LARGE PLATE MONITORING USING GUIDED ULTRASONIC WAVES

By

EMAD GHANDOURAH

A THESIS SUBMITTED TO UCL
FOR THE DEGREE OF DOCTOR OF PHILOSOPHY
DEPARTMENT OF MECHANICAL ENGINEERING
UNIVERSITY COLLEGE LONDON

2015

Declaration

I, Emad Ghandourah confirm that the work presented in this thesis is my own. Where information has been derived from other sources, I confirm that this has been indicated in the thesis.

Abstract

Areas of stress concentration around welded structures are likely to lead to fatigue cracks and corrosion pitting during the life time of technical machinery. Performing periodical non-destructive testing of the critical area is crucial for the maintenance of structural integrity and the prevention of unforeseen shutdowns of the system. Low frequency guided ultrasonic waves can propagate along thin structures and allow for the efficient testing of large components. Structural damage can be localized using a distributed array of guided ultrasonic wave sensors. Guided waves might be employed to overcome the accessibility problem for stiffened plate structures where access to some parts of the inspected structure is not possible. The transmission and reflection of the A_0 Lamb wave mode for a variation of the stiffener geometry and excitation frequency was investigated numerically and verified experimentally.

The dispersive behaviour of the guided waves has been studied to ascertain a frequency thickness product that provides limited pulse distortion. The limitations of the plate geometry as well as the excitation and monitoring locations were discussed. The radial spreading of the incident, transmitted and reflected waves from a stiffener has been investigated. The efficient quantification of the transmitted and reflected waves from the stiffener for a wide range of angles has been obtained from a single Finite Element model containing two parallel lines of nodes in front of and past the stiffener. The research outcomes have shown the dependency of the scattered wave on the incident angle and stiffener dimensions. Reasonably good A_0 wave mode transmission was obtained from the oblique wave propagation (up to an angle of 45^o) across realistic stiffener geometries. The choice of an optimum excitation frequency, which can ensure maximum transmission across the stiffener for specific plate geometry, was recommended.

The ability for defect detection in inaccessible areas has been investigated numerically and validated experimentally. The possibility of detecting and characterizing the reflection of a guided wave pulse (A_0 mode) from a through-thickness notch located behind the stiffener has been discussed. Two different approaches, based on the access to the sides of the stiffener on the plate, were employed. The limitations of the detectable defect size and location behind the stiffener have been investigated. The energy of the transmitted wave across the stiffener was adequate to detect simulated damage behind the stiffener. The evaluation has shown that defect detection in inaccessible areas behind stiffeners is achievable if the signal-to-noise ratio is high enough. In experimental measurements the noise level was of similar magnitude to the observed reflections at the defect. Thus, there is necessity to enhance the signal-to-noise ratio in experimental measurements.

Contents

LIST OF FIGURES

LIST OF TABLES

Chapter 1

Introduction

1.1 Motivation

In industry, there are many types of structures that are used for safety critical and hazardous applications, e.g. aircraft fuselage, pressure vessels, boilers, petrochemical storage tanks and off-shore oil platforms. Large plate components are often used to construct these structures, which can be subject to fatigue and corrosion damage during their life-cycle. Monitoring the structural integrity of these large structures is a very crucial task, but difficult to achieve. Eddy current as well as magnetic testing, liquid penetration, ultrasonic testing (UT) and other conventional non-destructive methods (NDT) have been used widely for the purpose of detecting unwanted discontinuities such as cracks and other flaws in the metallic structures [1]. Each one of these methods has been found to work efficiently for specific structures. Furthermore, non-destructive inspection plays a crucial role in the quality control of materials. It is used at all stages of the manufacturing process to monitor product quality, to determine the existing state of materials in order to accept or reject them and to specify whether a material or a part will satisfactorily perform its intended function or not. NDT is also widely used for routine or periodic determination of a plant integrity during service, not only to increase operational safety but also to avoid any forced shutdown of the plant. This work aims to contribute to the use of guided ultrasonic waves (GUW) for the structural health monitoring (SHM) of large metallic plate structure.

1.2 Ultrasonic Waves for SHM

The aim of this research is to strengthen the required basic knowledge for enhancing the applications of guided ultrasonic waves in SHM. Ultrasonic waves have been used widely for NDT inspections. Conventional UT is often used for inspecting thick metallic structures using bulk waves that propagate through the thickness. In contrast,

low frequency guided waves are primarily used for the SHM of large structures as they can propagate long distances along thin structures. Moreover, it is possible using guided waves to monitor large structures in relative short time compared to the time required for inspecting the same structure using bulk ultrasonic waves. So far, in industrial structures, the application of guided ultrasonic waves has been limited to a narrow field in pipeline inspection, in particular to buried and insulated pipes. Therefore, there is potential demand to expand the applications of guided waves for monitoring large plate structures. The thesis investigates the potential for defect detection in inaccessible area of plate structures, with a focus on the transmission of the A_0 Lamb wave mode across stiffeners to understand the possible defect detection sensitivity.

1.3 Overview

The use of guided waves for monitoring large plate structures is one of the methods that have been examined in the development of new NDT techniques [2]. This research intends to improve the applications of low frequency GUW for monitoring the integrity of large structures.

Previous investigations of guided ultrasonic wave scattering at structural damage such as fatigue cracks and corrosion pits have been summarized in Chapter 2. To obtain good understanding for the monitoring of large structures, an extensive literature review focused on the A_0 Lamb wave mode propagation and scattering using theoretical, numerical and experimental approaches has been made.

Chapter 3 describes the experimental setup that has been utilised in this project to study the A_0 Lamb wave propagation and scattering in large plates. Different excitation and monitoring configurations have been used to localise artificial defects in plates.

Chapter 4 introduces the finite element (FE) method that has been employed to model guided wave propagation and scattering in large plates. Matlab code has been used to automate the creation of FE models with stiffeners and defects of different sizes and locations. The scattering of flexural wave modes at cracks, notches and stiffeners has been considered for different excitation and monitoring configurations.

Chapter 5 shows the comparison of phase and group velocity measurements to theoretical and FE predictions.

Chapter 6 describes the analysis of the time trace signals for distributed sensor arrays to obtain the localization of defects in plates. The obtained results from the localization method, using both numerical and experimental approaches, have been compared with the actual defect location.

Chapter 7 shows the signal processing that has been used to separate and analyse both the reflected and transmitted signals at a stiffener. A new approach has been suggested to quantify the transmitted and reflected wave at a stiffener for a wide range of incident angles from a single FE simulation. The coefficients of the transmitted and reflected A_0 Lamb wave mode at the stiffener were predicted numerically and validated experimentally.

Chapter 8 investigates the influence of the stiffener geometry and excitation parameters on the transmitted and reflected waves. The interference at the stiffener location was studied, and the required time separation between the incident and reflected pulses was calculated. The dependency of the transmitted and reflected wave from the stiffener on the propagation direction was predicted for a wide range of incident angles.

Chapter 9 presents the FE modelling that has been used to detect and characterize a defect at different locations behind a stiffener. Experimental measurements have been performed to validate the numerical predictions. The procedures and steps that could be used to localize a real defect behind a stiffener in a large plate have been suggested at the end of this chapter.

A summary of the thesis and suggested future work, highlighting the aims of this work and presenting the main objective of each chapter in the thesis, have been discussed in Chapter 10.

Chapter 2

Literature Review

Understanding the way that guided ultrasonic waves behave in a large structure is a key step for establishing a new structural health monitoring technique for large plates. This chapter aims to introduce the general background of the propagation of guided ultrasonic waves in plate structures. Firstly, the most relevant studies and applications for guided ultrasonic waves in SHM have been briefly outlined in the current review. Then, the scattering and reflection of GUW at structural damage in plates has been reviewed. Finally, previous studies for single and multiple Lamb wave modes scattering at defects and surface features are reviewed to understand the wave behaviour across a stiffener in different directions.

2.1 Propagation of GUW

Generally, guided waves are of a particular interest for non-destructive inspection techniques as they have distributed stress through the thickness of the inspected part and can be used to detect defects at any depth. The wave can spread out in planar or cylindrical structures and propagate over large distances [2]. However, the main problem linked to the measurement of guided wave propagation in a plate is that it has dispersive characteristics and multiple modes. Different theories have been developed to explain the behaviour of GUW in plates. Lamb [3] described the dispersive propagation of the symmetric (S0, S1, S2 …) and anti-symmetric (A0, A1, A2…) Lamb wave modes. The GUW can be exited in plate-like structures, and during propagation these waves are guided by the plate boundaries along the structure. In addition to Lamb waves, another group of guided waves can propagate along plate-like structures. This group includes the shear horizontal wave modes (SH0, SH1, SH2 ….). For these modes the particle motion in the plate is perpendicular to the plane of propagation (Fig 2.1). For applications in pipelines the torsional modes (similar to the

shear horizontal wave modes in plates) were found to have several advantages over the flexural wave modes. Moreover, the SH0 wave mode has non-dispersive behaviour in plates. However, the controlled excitation of the SH0 wave mode was found to be slightly difficult without a good shear transducer, and it is more likely to lead to mode coupling between the SH0 and S0 wave modes. The displacement of the vibrating particle due to Lamb wave propagation was found to be in the plane of propagation. The first symmetrical mode S0 is non-dispersive at low frequency-thickness (fd) products and can be considered similar to a longitudinal bulk ultrasonic wave having mainly in-plate motion. On the other hand, the first anti-symmetrical mode A0 (Fig 2.1) is often called a flexural or bending wave mode due to the bending motion of the plate (out-of-plane displacement) [4].

The flexural wave mode (A0) has been chosen in the current research to study wave propagation in large plates. Due to the significant out-of-plane displacement the A0 mode can be excited easily in plate structures using single sided access with piezoelectric transducers. Similarly, the wave propagation and scattering can be measured easily using a non-contact, commercial laser vibrometer sensitive to the out-of-plane motion. Using the A0 wave mode in the experimental measurements has thus advantages over using other wave modes such as S0 and SH0. The A0 wave mode has a shorter wavelength compared to the S0 mode at the same frequency, and thus better sensitivity for defect detection.

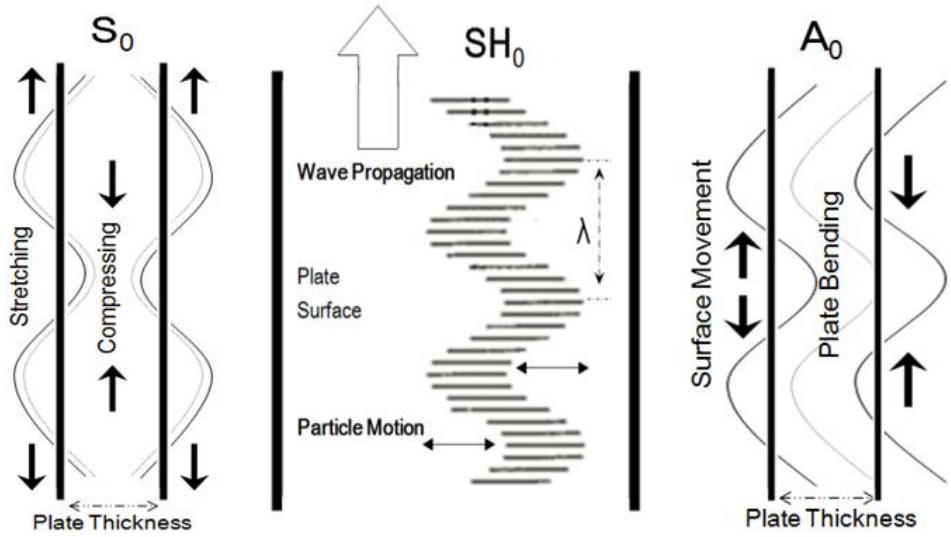

Fig 2.1 Comparison of different wave modes showing plate and particles motion in the case of S_0, SH_0 and A_0.

However, in the low frequency thickness regime the A_0 mode is more dispersive compared to the S_0 mode, requiring either more care in the choice of operational point (*fd*) or the usage of more advanced signal processing techniques. The mode shapes of the Lamb wave modes at 0.5 MHz mm frequency thickness product in an aluminium plate were obtained using the Disperse modeling program and are shown in Fig 2.2. Large out-of-plane displacement can be seen for the A_0 mode shape with limited in-plane displacement (Fig 2.2a). In contrast, the amplitude of the in-plane component for the S_0 mode (Fig 2.2b) is large relative to the amplitude of the out-of-plane component. Classical plate theory (CPT) can be seen as the simplest approach that describes the bending waves in plates. However, this theory uses bending stiffness only to estimate wave behaviour. A very good approximation of the A_0 mode was developed by Mindlin [5] to enhance the dispersion equation, including shear and rotary inertia in the calculations of the bending wave propagation. Thus, the error predicted by Mindlin's theory in the calculation of the real wave number was found to be less than the error of CPT theory [5]. The propagation behaviour of guided ultrasonic waves at different velocities and for a range of excitation frequencies has been described using several approaches [6].

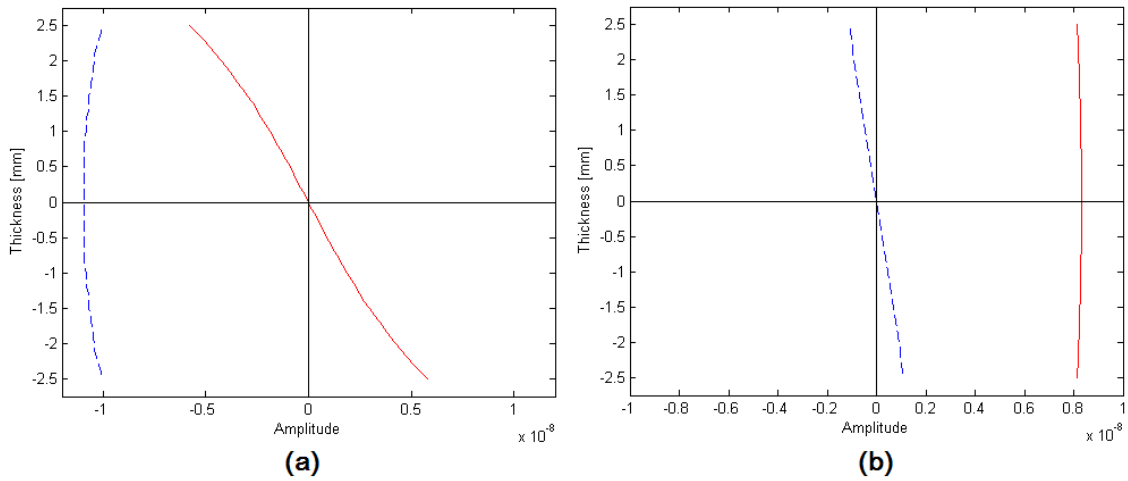

Fig 2.2 The mode shape of (a) A_0 and (b) S_0 wave modes at 0.5 MHz.mm in aluminium plate showing in-plane (blue dashed line) and out-of-plane (red line) displacements

Lamb wave modes are found to be dispersive, and at low *fd* the phase and group velocity varies with changing propagation frequency (Fig 2.3).

A general purpose modelling program (Disperse) was introduced in 1991 to generate the dispersion curve [7]. This interactive Windows software was developed to study the behaviour of guided waves in a wide range of structures, and to predict the characteristics of the wave propagation theoretically. Only the fundamental wave modes such as compression (S_0), flexural (A_0) and shear horizontal (SH_0) modes can propagate below the cut-off frequencies (f_c) of the higher wave modes. Lamb wave propagation at low frequency-thickness product has been employed widely for the monitoring of large plates [1] because the single wave modes at low *fd* can be analysed more easily. On the other hand, multiple wave modes can propagate at high frequency-thickness products, above the respective cut-off frequencies f_c, and the number of propagating modes increases with increasing excitation frequency. The cut-off frequencies f_c of the Lamb wave modes can be calculated based on the Rayleigh-Lamb theory [4]. The f_c of the A_1 mode was investigated as well, and obtained at about 1.5 MHz.mm for steel and aluminium plates.

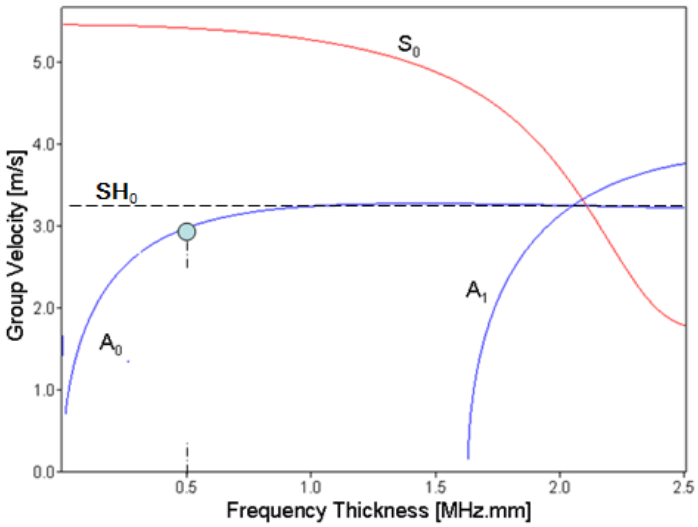

Fig 2.3 The group velocity of different guided wave modes in steel plates; A_0 wave mode at 0.5 MHz.mm marked

2.2 Scattering and Reflection of GUW

The reflection of GUW occurs when the propagated Lamb waves reach a sudden change in the plate material or structural damage, e.g., severe reduction in the plate thickness due to corrosion pitting. At that point, the guided wave mode is scattered and part of its energy is reflected back towards the excitation location [8]. Processing methods have been developed for analysing single and multiple wave mode propagation [9, 10]. Multimode scattering due to mode conversion has been investigated at different structures. Working at high *fd*, where multiple modes dominates, has been suggested for improved sensitivity for defect detection [11]. However, multimode waves have been employed in limited research projects compared to the work that has been carried out using single mode waves. The limitation in using multiple mode waves is mostly due to the expected interference between different modes which complicates the analyses of the observed signals. Though wave propagation at high *fd* is recommended for good detection sensitivity, propagation at low *fd* in single wave mode has been utilized in this research to avoid multimode signal processing.

Several studies have been conducted on metallic and non-metallic plates to investigate the characteristics of Lamb wave scattering at plate boundaries and structural discontinuities. In metallic plates, the reflection of GUW has been studied at different types of reflectors, mainly circular defects [12, 13], notches/cracks [14, 15] and surface features [16]. Material loss due to corrosion has been modelled as a part-thickness hole of various diameter and depth [17]. The scattering and mode conversion of the A_0 Lamb wave at circular damage has been predicted numerically and validated experimentally. The amplitude of the back scattered wave from the damage relative to the propagated wave pulse across the damage has been calculated. The scattered wave amplitude is found to be strongly dependant on the ratio of defect dimensions to wavelength due to constructive and destructive interference at the defect location. In addition, thickness reduction is found to be effectively varying the amplitude of the scattered wave. Different analytical approaches have been used to describe the scattered field of the A_0 wave mode around a circular cavity based on Kirchhoff and Mindlin plate theories [18]. Flexural wave propagation and scattering from a hole in an

aluminium plate has been measured using a laser interferometer to validate the approximate solutions. Good agreement has been achieved between experimental data and analytical solutions. Significant change was seen in the measured scattered field due to notch smaller than the employed wavelength introduced at the hole boundary. Development of a defect at a hole was found to be detectable using the variation of the measured amplitude.

In a different application, Lamb wave mode scattering has been modelled at low frequency-thickness product in an aluminium plate to study the mode conversion at circular imperfections [19]. A comparison between Poisson/Kirchhoff (classical plate theory) and Poisson/Mindlin (plate wave theory) models has been presented. The evaluation has shown that Poisson/Mindlin was performing better with in-plane wave modes at high frequency thickness. Backscattered A_0 Lamb wave amplitude from a circular scatterer with different plate properties has been predicted numerically [20]. The numerical prediction has been validated theoretically based on a developed analytical approximation for flexural wave scattering in the context of Mindlin wave theory. The calculated scattering at the circular region has been compared to similar outcomes obtained by using the Kirchhoff plate theory.

The A_0 wave scattering from notches and cracks has been predicted numerically and validated experimentally at low *fd* [1]. More recently the applications of GUW for structural health monitoring have been investigated at high *fd* [21]. Developing experimental approaches that focus on the Lamb wave reflection from cracks and notches at different orientations and various incident angles were the main objectives of this research [22]. The effects of the wavelength and wave diffraction on the transmission and reflection coefficients have been analysed. The reflection coefficient was found to be a function of both crack length and ultrasonic wavelength. At relatively short crack lengths, wave reflection was linearly proportional to the crack length, and then amplitude oscillation occurs in the reflected wave with increasing crack length. On the other hand, for relatively short cracks the wave diffraction was significantly affecting wave transmission. In addition, the transmission coefficient was found to

decrease at long crack length. The A_0 Lamb wave mode scattering at part- and through-thickness cracks has been investigated [23]. For all investigated cases of incident angle and defect size it was found that in certain directions very little scattered wave energy was observed. A good agreement has been obtained between the experimental measurements and the numerical prediction. Sensitivity of the scattered guided wave to the defect orientation and length has been discussed in a further step. A hybrid model has been developed to quantify the detection sensitivity at likely defect locations and orientation [24]. The scattering characteristics of the A_0 wave mode from part-thickness and through-thickness notches at different lengths have been predicted using the FE simulation and verified from measurements on machined slots in an aluminium plate. The sensitivity for defect detection was found to be strongly dependent on the chosen geometric configuration in relation to the possible defect location. The capability of using distributed array of guided wave sensors for the imaging of part thickness defects in plate structures has been investigated [25]. The detection sensitivity for fatigue cracks was found to vary with the location and orientation of the crack relative to the transducer location. Imaging algorithms have been suggested to avoid incorrect defect localization.

The scattering of GUW in two-dimensions (2D) has been investigated numerically to obtain predictions that can be verified to from analytical and experimental studies. Better understanding of the influence of varying plate thickness on the guided wave field along the plate requires further investigation using a three-dimensional (3D) model. Recently, 3D FE models are more frequently used to study the scattering of Lamb wave modes in large plate-like structures. The angular profile of the SH_0 wave mode scattering at through thickness cracks was studied in 2D based on the wave reflection and diffraction at the crack [26]. Reflected waves were found to be mainly concentrated in a narrow angular band around the specular direction, varying with the incident angle. The normal incident wave on the crack has shown the strongest reflection that could be sufficient for defect imaging. The numerical prediction of the wave propagation and scattering using 2D finite element models has been validated experimentally [27]. Lamb waves were excited at low frequency thickness product in metallic plates and the reflection coefficient of the A_0 wave mode from shallow and

very deep cracks was obtained. The reflection function, which was characterised by the geometric ratio of the wavelength to notch width and *fd* products, has shown a complex shape due to the interference between the reflections from the two sides of the notch. Experimental validation has been carried out for another 2D FE model [28], in which Lamb waves were used at low excitation frequency. The scattering of the S_0 wave mode from rectangular notches of various widths and depths was modelled. The analytical study of the reflected wave from the notch sides has been used to explain the behaviour of the reflection function. Significant changes, from a linear slope at low frequency towards a frequency independent constant value at high frequency, were observed in the reflection function.

Separation of in-plane and out-of-plane Lamb wave components for crack detection in metallic structures has been attained experimentally using a 3D laser vibrometer [29]. Very little difference was seen between the measurement sensitivity of the in-plane and out-of-plane vibration components for impact damage detection. Damage localization and detection sensitivity were obtained efficiently using the amplitude of the propagated wave. Measurements have been carried out in 2D to study the interaction of low frequency SH_0 waves with through-thickness fatigue cracks [30]. The influence of the crack length, excited wave and measurement position on the reflected wave from the crack has been investigated. The backscattered wave from the crack was found to carry most of the reflected energy. Crack reflection was observed clearly using uniform shear sources in the far field. Demma et al. [31] have used a FE model to study the reflection of low frequency SH_0 waves from part thickness notches in a 2D plate model. The influence of the excited frequency and notch length on the magnitude of the reflected wave has been compared. Measurements have been conducted to verify the predicted results from a thickness step and v-notch. The reflected SH_0 wave mode from the step at low frequency was almost constant with varying frequency-thickness products (*fd*). Consideration of the interaction of the non propagating modes with the sides of the notch was very important to show the dependency of the wave scattering field on the *fd* products, especially at very small notch axial extent.

The scattering of plane waves at a finite scatterer was predicted using circular sets of nodes surrounding the scatterer [32]. The complete scattering behaviour for the far-field has been extracted from the matrix of Fourier coefficients based on the model size and order of the computational load (degree of freedom). The difference using baseline subtraction was related to the presence of the scatterer alone. Then, modelling accuracy was investigated using comparison to the analytical solution for a circular cavity at different modelling parameters.

The previous study, which was monitoring the wave scattering in 2D at all directions, has been investigated in a 3D numerical model [33] in a bid to compare the required computational time. Only the near surface scatterer and the immediate vicinity of the surrounding medium were modelled. The computational load for non-reflecting boundary conditions was found to be several orders less than for the model with absorbing layers. The comparison showed that the maximum dimension of the 2D and 3D scatterer was affecting the required degree of freedom and computational time. In further research, a boundary element computational solution has been employed to simulate the A_0 Lamb wave mode scattering at different geometrical obstructions such as joints and stiffeners. The transmission and reflection behaviour of plate waves at stiffening ribs were predicted using a 2D computational model [34]. For this purpose experimental observation was performed to validate the numerical prediction for the wave transmission across thin and tall stiffeners in particular. In addition, the numerical prediction has revealed the reason behind observing robust transmission results and poor wave performance in the case of a square stiffener profile. The behaviour across square ribs resulted from increasing the frequency bandwidth range, from 200-300 kHz to 320-470 kHz. Scattering of Lamb wave modes from surface features and stiffeners was predicted in both 2D [35] and 3D [36] models. Scattering of Lamb waves at defects in plate has been studied for a variety of cases. Depending on the scatterer characteristics a dependency of scattered wave was found. For larger defects reasonably good detection sensitivity was predicted, but can depend on angular scattering patterns and sensor location.

2.3 Applications of GUW for SHM

GUW have been employed in several studies to detect structural damage in non-destructive testing and structural health monitoring applications. Monitoring of the thickness reduction in different types of structures was one of the main aims of these studies [37]. Applications of NDT and SHM, in principle, differ in the test duration and area coverage for each measurement. In SHM, where the transducers are typically permanently attached to the structure, the degradation of a complete structure throughout its service life is monitored continuously. In contrast, for NDT, the components of the structure are tested at a maintenance interval based on the required level of inspection. Most of the GUW studies aim to develop experimental approaches that detect, localize and characterize a defect in a large structure.

2.3.1 General SHM Algorithm for Damage Detection

Considerable interest has been observed recently for SHM applications that use Lamb wave propagation to localize the expected damage. In principle damage can be localized using a minimum of three transducers, acting as actuator and sensor. Improving the accuracy of the defect localization required using a larger number of transducers. In contrast, achieving good signal-to-noise ratio required employing less sensors and actuators as has been found using the synthetic time-reversal method [38]. The principle of the new method has been developed for large area monitoring using a distributed network of transducers. Based on the arrival time of the scattered wave pulse from a defect, ellipses that represent the potential damage location were calculated for each excitation/sensor arrangement. The intersection point of the ellipses around the excitation/monitoring locations represents the damage location in the monitored structure. With circular patch transducers, the shape of the time-reversal wave was not exactly the same as the original excitation. The applications that have been reviewed in the following paragraphs where categorized in different groups based on the employed transducer array. The presented damage localization techniques contain phased arrays, localized arrays and distributed arrays of monitoring transducers.

Damage detection using the phased array method has been discussed in the following group of applications. The use of piezoelectric wafer active sensor (PWAS) based on the phased array principle was resolved in an improved numerical prediction model [39]. Two PWAS sensors were adopted in pitch-catch measurements to monitor the multimode Lamb waves scattering in an aluminium plate at high *fd*. The prediction of the numerical model was matching the experimental results much better than the conventional models. Nevertheless, the used method for monitoring wave propagation was found to be limited to simple metallic structures and rather imprecise at high excitation frequency, where multiple dispersive modes interfere with each other. The capability of the PWAS to excite and detect tuned Lamb wave for SHM has been investigated in a further study [40]. Different Lamb wave modes were used to detect through-thickness cracks employing the pulse-echo method. The propagated wave across the crack was responding with a different behaviour based on the utilized wave mode. The maximum excitation and detection has been achieved when the PWAS length equals half the wavelength of a particular Lamb wave mode.

Further applications of the GUW have been used to detect and characterize different damages using a localized array of transducers. Localized arrays of PZTs have been used in different NDT techniques, e.g., L-SAFT [41], for imaging corrosion flaws in metallic plates using Lamb wave propagation. Additional background noise was observed in the recorded images due to mode conversion, which caused minor difficulties in interpreting the reflected wave from damage with accurate information about defect size and location. Exciting and detecting the S_0 wave mode in an aluminium plate using a circular array of electromagnetic acoustic transducers (EMATs) has been performed experimentally [42]. A phased algorithm has been used in conjunction with the array elements to produce B-scan images of the surrounding plate. Two methods of signal processing have been performed on the collected data from the circular pattern of elements that behave as omni-directional point transducers in a bid to study the effect of the array diameter on the angular resolution. The phased addition algorithm seems to be applicable to any geometry of array element and for different plate thicknesses. For better inspection performance, the required number of elements in the monitoring array was reasonably high. A sensor array with 64

transducers was employed to perform simple and direct measurements of the propagation field under the array [43]. The acoustic performance of the sensors that were triangulating the leak location in the spacecraft was compared to the experimental measurements and good agreement was achieved. The array method was found to be very efficient, since it requires small amounts of information extracted from a large amount of collected data about the leak noise. In addition, the required processing algorithm for the array method can be applied simply.

In other GUW applications, distributed networks of transducers were employed to measure and localize the damage using Lamb wave propagation. Baseline measurements have been followed by defect measurements using a mass bonded to an aluminium plate [44]. Then baseline subtraction method was used to detect and localize the mimicked damage. Cracks longer than 6 mm were detected utilizing non-contact measurements of local amplitude and time-of-flight variations. Similarly, distributed arrays of piezoelectric transducers have been used in different combinations in order to localise linear cracks in aluminium plates based on the time of flight analysis for a single wave mode [45]. The crack position in the plate was successfully identified with satisfactory precision using a nonlinear least-squares optimization algorithm. In another study, a sparse array of transducers were instrumented on an airframe panel to investigate the possibility of reducing the number of baseline measurements that were required for monitoring a complex shape [46]. The reduction in the number of baselines in the database was limited by the maximum temperature gap between baselines, wave mode purity and the maximum propagation distance to cover the whole structure. For good sensitivity at reasonably high signal complexity and insufficient mode purity, the required temperature gab between baseline measurements was less than 0.5 ^{o}C. Finally, the noise level due to temperature fluctuation and wave reflection has been improved reasonably by reducing the number of baselines in the database. Distributed arrays of PZT transducers were used in two SHM experiments to reconstruct a through-thickness circular hole on a large aluminium plate [47]. The performance of the *in situ* commercial array of transducers has been predicted numerically and validated experimentally using baseline subtraction method. The imaging technique of single transmission and multi-receivers (STMR) was performing effectively when the

inspected structure allowed for a back reflection towards two PZT transdusers (at minimum). In a different approach, arrays of distributed sensors have been used to quantify the detection sensitivity for crack-like defects in a plate structure [48]. The predicted damage location using different evaluation concepts has been validated experimentally based on measurements behind a stiffener welded to the plate. The simulated access to one of the plate sides has shown that defect detection is still possible but the accuracy of the localization decreases significantly.

2.3.2 Problems of Baseline Subtraction

Permanently attached *in situ* sparse arrays have been used widely for monitoring the behaviour of *a priori* known wave propagation and scattering. Imaging damage in a plate-like structure using sparse transducer array was achieved experimentally and verified numerically using different signal processing techniques. Time shift averaging algorithms have been applied to differential signals filtered at multiple frequencies to improve the quality of the defect image [49]. A set of images have been created and combined to obtain accurate damage localization with reduced noise level. Then systematic incorporation of multi-frequency information seems to have significantly improved damage detection and localization. The sparsity degree that could minimize the image reconstruction error was investigated while utilizing artificial damage in an aluminium plate [50]. Baseline subtraction was performed using delay-and-sum differential signals technique. Mismatch was observed between the measured and predicted image due to considerable noise level in the analysed signals. Good performance was achieved after applying a two-step hybrid technique, basis pursuit de-noising (BPDN), and then orthogonal matching pursuit (OMP) in multiple damage sites.

Some of the SHM applications required previous information about the expected wave propagation behaviour and probable damage location in the inspected structure. A technique that enables dispersive time-domain signals to be mapped to propagation distance while removing the effect of dispersion has been described based on *a priori* known characteristic of the GUW and material properties [51]. Most of the localization

algorithms have been developed based on known wave propagation characteristics. These algorithms have been tested on very limited data sets and iterated until their desired performance was achieved. The practical upper limit on plate thickness was then considered by several factors such as transducer efficiency, which was governed by mode shape, and the presence of higher order guided wave mode. The applicability of performing *in situ* measurements using a small number of distributed sensors has been investigated [52]. The algorithm has been validated by quantifying the actual transmitted and received signals. Then the dispersion curve has been estimated using numerical simulation with minimal *a priori* information to develop the mathematical approach that can suggest the parameters of the GUW. Finally, the propagation loss, transducer distances and mode weighting coefficients have been described as well in the algorithm.

The effect of changing temperature on the response of the GUW pitch-catch system for SHM has been discussed [53]. Deriving a closed form solution for the spatial Fourier transform of the transformed shear stress from a simulated actuator into a plate-like model was the main aim. It was found that the temperature change has a significant effect on the amplitude of the propagated wave and negligible effect on the wavelength tuning points. The influence of the environmental change on the SHM approach was quantified numerically and validated experimentally [54]. Temperature variation was found to change wave velocity and affect the dispersion curve of guided waves. Though temperature change was significantly affecting baseline subtraction, optimal baseline subtraction (OBS) was found to reduce the coherent noise in the measurements and gives the least error. OBS requires a set of baseline measurements recorded from the undamaged specimen for different temperatures spanning the expected service temperature range. Optimal baseline subtraction can be attained by comparing the current time trace signals to all available baselines and subtracting best matched baseline waveform from the damage signal, in order to reduce residuals due to temperature change.

Baseline subtraction has been used to detect small damage in several research projects, with optimal baseline subtraction used mainly to eliminate the effect of the temperature change [55]. The parameters that cause instability and robustness of OBS under varying rates of temperature change have been studied. The used method has improved the signal to noise ratio by up to 20 dB, and shown the ability to detect damage above the noise level, which is typically around -40 dB. A controlled environment, where the temperature is gradually increased then cooled back to ambient temperature, was used to perform the SHM on a real, complex steel structure [56]. Robust temperature compensation strategy has been performed based on a combination of the optimal stretch method and baseline subtraction to avoid having overlap reflections. Emphasizing the first arrival pulse by eliminating secondary pulses has been used in order to obtain an optimal estimator for defect localization in any given structure and sparse array. The final form of the optimal estimator was found to have superior performance over other existing estimators in the context of stiffened aluminium plates. Modelling systems that use reference signal subtraction to increase damage amplitude relative to structural feature amplitude have been investigated using a sparse array of sensors [57]**.** Comparison between two subtraction methods and two sensor configurations has been performed to show the dependency of the damage detection on the temperature change and propagation distance. A relationship between sensitivity and sensor pitch was found and similar behaviour obtained from two different signal subtraction approaches. The investigated strategies for guided-wave SHM were found to be economically and practically feasible by using one sensor per square meter.

The applied loads on an engineering structure can considerably affect the propagating wave between the distributed sensors monitoring structural integrity. Distributed arrays of piezoelectric transducers have been employed to estimate applied loads from observed change in the phase velocity over a range of propagation directions [21]. Numerical solution was used for decoupling the effect of homogeneous biaxial stress into its two principle components. The stress level was predicted numerically and validated experimentally using S_0 wave mode propagation over a narrow frequency band in aluminium plates. The obtained time shifts using this approach were related to the load change only, i.e., the contribution of the temperature change in the load

variation was neglected. In a different SHM application, Lamb wave scattering has been used to examine detection performance in long-term structural health monitoring [58]. Experimental measurements were performed on a pair of surface-mounted PZTs to investigate bonding problems and identify defective transducers in the monitoring system. Linear reciprocity of guided waves between transducers has been proposed to assess abnormal behaviour in the damaged PZT while it functions in the SHM system. Measurements were performed on an aluminium plate without baseline comparison. The used methodology has been examined under several complicated geometrical conditions which prove to be suitable for distributed PZT array.

2.3.3 Monitoring Complicated Structures

Interpreting data signals to localize damage in a complex structure requires *a priori* knowledge of the geometry of the structure. The following SHM applications have dealt with complicated structures. Localizing air leaks in complicated spacecraft skin structures due to high-speed collision with small objects was discussed in a previous research [59]. Cross-correlation has been used to transform the leak noise into a measurable and deterministic quantity. Based on the amount of the collected data and the simplicity of the processing method, this approach appears to be extremely robust. Locating leaks generated by micrometeorite debris impact on a manned spacecraft is another similar example of SHM applications in complex structures [60]. Cross-correlation of ultrasonic noise from a leak source was employed once more to demonstrate guided wave propagation and scattering in the spacecraft skin. Four methods for sensing and processing leak noise, phased array, distributed sensor, dual sensor and propagation pattern were developed and tested. Each of these methods was found to be repeatable and suitable for different circumstances. The risk of micrometeorite and space debris to the mission of the spacecraft and cabin crew can be dramatically reduced by applying these methods. In a different monitored structure, Rayleigh waves have been excited at high frequency-thickness product to measure the transmitted wave across multiple stiffeners in an aluminium plate [61]. The measured reflection from machined notches was found to be comparable to theoretical prediction. The detection of a surface defect with a depth more than $1/10$ of the plate thickness seemed to be possible past multiple stiffeners using a Rayleigh-like wave mode. Wave

propagation within both single layer and multiple layers waveguides has indicated overlapping in the dispersion curves of the phase and group velocities at some incident modes [62]. The incident modes that have identical wave structure (mode-pair) were selected to ensure maximum energy transmission between waveguides. Then the wave mode conversion at the transition zone between waveguides (single and multiple layers) was predicted using the SAFE method and the normal mode expansion. Agreement was achieved in the mode-pair selection based on the comparison between model prediction and the dispersion analysis. Signal-to-noise ratio and defect sensitivity were improved by using the selected mode-pair.

2.4 Flaw Detection behind a Stiffener

Applying any inspection method or detection technique to SHM requires further description of the anticipated structural damage. Flaws at a stiffener (T-joint) can take many forms and appear in different ways depending on the location and function of the stiffener in the industrial structure. For instance, in the shipbuilding industry and in off-shore platforms the salt water (sea water) is expected to cause corrosion on the outer surface, which is usually opposite to the stiffener side [63]. On the other hand, in structures such as boilers and large pressure vessels, the damage mostly occurs on the internal surfaces that contain the T-joints [64].

Inspecting structures that contain inaccessible bonded joints requires *a priori* knowledge about the guided wave scattering at geometrical discontinuities and material change in the structure. Moreover, understanding the mode conversion that occurs due to wave propagation across bonded joint was another crucial step for improving adhesive joint inspection. Recently, the trapped energy of the non-dispersive shear guide wave mode at weld in a steel plate [65] and bond line in an aluminium plate [66] has been predicted using the semi-analytical FE method. Validation has been performed using experimental measurements and a good agreement has been achieved in comparison to the numerical approach. The investigation has shown that the propagated mode can be concentrated in the weld direction when it has a similar mode shape as in the side plates but with lower phase velocity [65]. Though high-order weld-guided

modes have been found during the model calculation, only the shear and compression weld-guided modes were discussed in the investigated case to simplify the used model. The trapped shear guided wave along a T-shaped stiffener bonded to the aluminium plate has been measured using laser interferometer to verify the numerical prediction [66]. The influence of the epoxy shear modulus and bond line thickness on the phase velocity and trapped energy have been investigated, and significant variation was observed in the dispersion curves due to large change in the shear modulus during the curing of the adhesive.

Propagation of the GUW in plate-like structures has been employed in different research work to study the wave scattering from a defect located past a stiffener. Despite the considerable efforts that have been recently directed at simulating wave propagation across a stiffener in plate-like structures [36]**,** very limited research work has tackled the scattering of oblique incident guided waves at a straight surface feature. The propagation of Lamb waves across a stiffener modelled along the width of infinite planar host waveguide has been investigated [35]. The semi-analytical finite element (SAFE) method has been used to create a 2D model of the bulk wave scattering at a uniform cross-section modelled along the plate width. Propagation of the incident wave mode (S_0) has been modelled at 1 MHz in an aluminium plate with and without a bonded stiffener to obtain baseline subtraction. The transmitted and reflected coefficients of A_0 and SH_0 wave modes have been calculated at a range of propagation directions, 0^o - 70^o, by creating one model for each angle. The coefficient of the reflected S_0 and SH_0 wave modes at 30^o propagation direction has been predicted at a range of excitation frequencies, 0.2 MHz to 2 MHz [35]. Finally, the measured wave transmission across a bonded stiffener has been compared to the numerical results and good agreement was achieved.

The rigidity of aerospace structures has been improved by employing vertical stiffeners of minimal additional weight. The scattering behaviour of the plate wave at geometrical obstructions such as joints and stiffeners in a spacecraft skin has been predicted and validated experimentally in several SHM applications. The influence of the geometrical

obstructions between sensor and acoustic noise source in the spacecraft skin was investigated [67]. Measurements of the noise transmission across geometric obstructions have been compared with the measured signals in an unobstructed plate, and then good agreement was obtained in comparison to the theoretical prediction. Though they have different physical models, studying normal transmission across a stiffener has provided the required understanding for the leak problem in the spacecraft skin. The transmission coefficient at normal propagation across a stiffener was demonstrated in a further step to provide guidance for robust frequency selection [68]. The characteristic of the geometrical obstructions and their influence on the performance of the PZT array detector was the major limitation in the predicted model. Based on the necessary guidance for frequency selection, the frequency that has widest possible bandwidth should be chosen for localizing the air leakage in the spacecraft structure. The effect of integral stiffeners on locating the leak source was examined with a specific proposed application for spacecraft structures [69]. The propagated energy from a leak source to a contact-coupled acoustic array was predicted at a range of frequencies, 50 - 400 kHz. The properties of the transmitted signals have shown significant increase at high frequency, and a good agreement was found in comparison to the experimental outcomes. The optimal propagation direction that provides the best transmission coefficient over a range of operating frequencies was proposed. Eventually, it was found that the stiffener geometry determines whether or not the excited wave can spread from the noise source to the array detector.

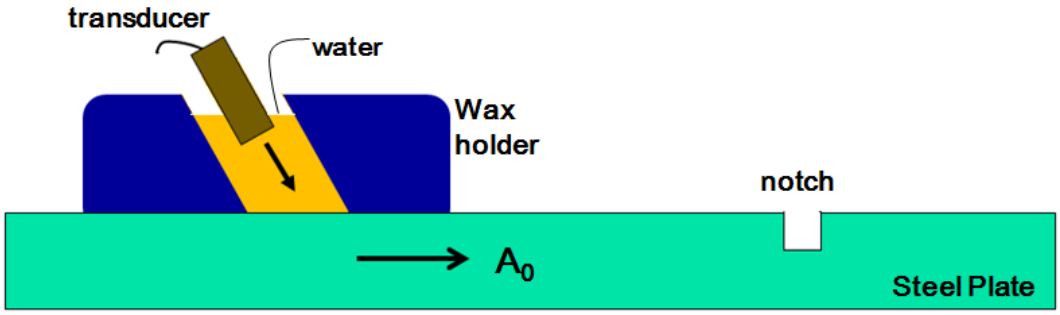

Fig 2.4 Schematic diagram of the normal A_0 Lamb wave incidence on a simulated notch along the width of a plate-like structure.

The normal incidence and reflection of plane guided waves at artificial flaws in a plate structure was discussed by Lowe et al [27]. The FE method has been used in two-dimensions to simulate the A_0 wave mode scattering at notch modelled along the plate width (Fig 2.4). A more comprehensive approach towards studying the scattering of guided waves at a surface feature, for instance, a stiffener or a straight weld performed along the width of a large plate structure, can be conducted using a 3D finite element model. The reflection and transmission of the A_0 Lamb wave mode at intact stiffeners welded to a steel plate were monitored experimentally using a laser vibrometer [36]. The obtained measurements were verified using a FE model. The normalized amplitude of the exited wave, ahead of and behind the stiffener, was used to calculate the coefficient of the transmitted and reflected guided waves. Finally, a monitoring approach was suggested to detect any structural damage at the stiffener.

The presented review in this chapter provides the background for guided wave propagation in plate-like structures. The dispersive behaviour, which GUW show in plates, has been illustrated using dispersion curves for different guided wave modes. In addition, the review has shown some useful details about the expected wave scattering and mode conversion at different types of thickness change and structural damage. Based on the discussed applications of GUW, an obvious research area was found to be not tackled, even though it is very important for extending guided wave applications in the context of SHM. The current research is studying in detail the transmission and reflection of the flexural wave mode (A_0) from a stiffener. The outcome of this study is expected to have significant application for ship hull monitoring, and to contribute to SHM applications in complex structures such as aircraft fuselage in the future. This research has been extended to study the possibility of detecting and characterizing the A_0 mode reflection from a notch behind stiffener.

In conclusion, the literature that has been presented in this chapter has covered most of the theoretical and experimental methods that have been developed to investigate GUW applications for structural health monitoring in large plates. In addition, the potential applications of the A_0 Lamb wave mode in non-destructive testing have been explored in this chapter to establish a proper base for further research. Several applications of localized and distributed measurements using PZTs and laser vibrometers have been discussed in this chapter. Reflection of the A_0 Lamb wave from through-thickness

cracks and notches in a plate structure has been studied. Wave transmission across a straight weld performed across the width of a large plate has been investigated. Different types of defects behind stiffeners and T-joints have been detected and localized. Moreover, localization accuracy has been quantified in several studies using sensor arrays. More complicated structures such as spacecraft frames have been monitored in various SHM research projects. Laboratory experiments from the most relevant work in the literature review will be repeated in Chapter 3 as an important foundation for the current research project.

Chapter 3

Experiments

The propagation and scattering of guided ultrasonic waves has been widely studied in the last decade. Most of the theoretical approaches that govern Lamb wave propagation and scattering in large structures have been verified experimentally. The experiments in this chapter aim to build a solid base for new research based on the outcomes of previous research as discussed in the literature review. Several experiments for the A_0 wave mode propagation have been repeated to understand the way that flexural wave modes behave in large plate structures. Different experimental configurations have been used to study guided ultrasonic wave propagation and scattering at defects and stiffeners in large plates. The measurement procedure and the calculations of the wave propagation from the obtained results have been explained in this chapter with a brief evaluation.

3.1 General Experimental Setup

The flexural wave mode (A_0 Lamb wave mode) was selected for the experimental approach because it can be excited and measured easily using single sided access with PZT transducers as discussed in chapter 2. Moreover, the A_0 wave mode has significant out-of-plane displacement, allowing for the point wise, non-contact measurement with good accuracy a using commercial laser interferometer. The additional reason for choosing the flexural wave in this research is the shorter wavelength (λ) as compared to the S_0 mode at the same frequency range, giving sufficient sensitivity of the wave mode to small defects that was considered reasonable at low frequency range. The excitation location and frequency were chosen to allow for sufficient separation between pulses (incident and reflected) in the time domain, and to show good spatial resolution of the scattered waves.

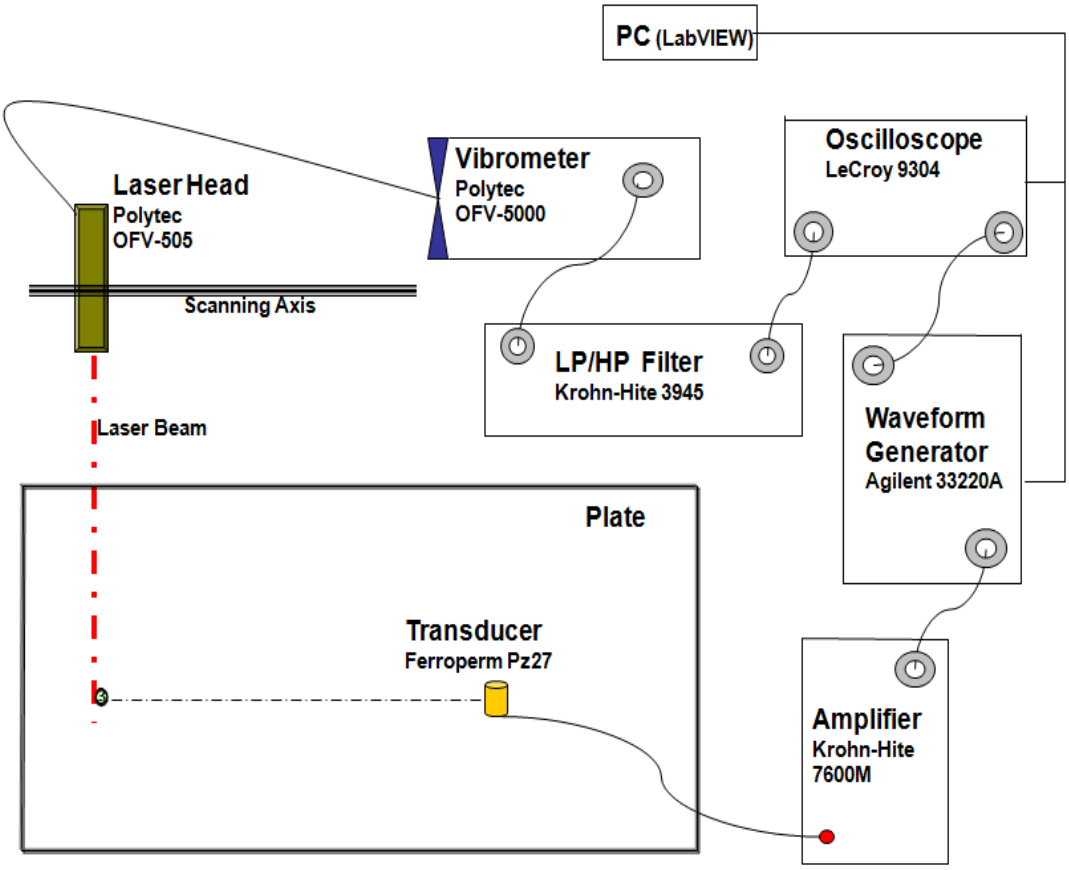

Fig 3.1 Schematic of the general experimental setup.

The propagation of the A0 Lamb wave mode was measured at low excitation frequency, and was found to be dispersive and to require advanced signal processing techniques. The experimental setup that has been utilized in this research has been used before for several projects and SHM research in the Mechanical Engineering Department of University College London [70]. The general experimental setup consists of a piezoelectric transducer glued to a large metallic plate, waveform generator, amplifier, laser interferometer, bandpass (LP/HP) filter and oscilloscope (Fig 3.1). Since the excited and measured wave mode (A0) in the plate has significant out-of-plane motion, observing the S0 wave mode with significant in-plane motion was not expected with the used measurement method (laser interferometer).

3.1.1 Monitored Plates

The experimental part of this research investigates the use of the flexural waves for the SHM of metallic plate structure. Two different plates have been used in the

experimental measurements (Table 3.1). For the initial measurements of the wave propagation characteristics an aluminium plate (AL 2014-T6, 1 m length, 0.7 m width and 3 mm thickness) has been used. The wave propagation characteristics and velocities in aluminium and steel plates are reasonably comparable, thus procedures and experience developed using aluminum plates can be easily transferred to steel plates. Aluminium plates are lighter and thus easier to handle in a laboratory environment and typically have good surface finishing compared to steel plates. The accurate measurement of wave propagation along steel plates required surface preparation before transducer bonding and application of strips of retro reflective tape to reflect back enough laser light for guided wave measurement with sufficient signal to noise ratio. A stiffened steel plate, with the ratio of stiffener dimensions similar to that used in ship hulls, has been employed to measure the coefficients of the transmitted and reflected wave from the stiffener. The stiffener consisted of an L-shaped cross-section (size: 50 mm × 50 mm and 5 mm thickness) welded across the width of the steel plate (size: 2 m × 1 m and 5 mm thickness). For both plate specimens, simulated defects were introduced during the measurements. A mass was glued to the aluminium plate as a simulated defect for the measurements described in chapter 3.3. For the stiffened steel plate a notch was cut into the plate as described in chapter 3.5.

Table 3.1 Types of tested plates in the experimental work

Plate #	Material	Dimensions	Stiffening
1	Aluminium	1 m x 0.7 m, 3 mm thickness	No stiffener
2	Steel	2 m x 1 m, 5 mm thickness	With stiffener

3.1.2 General Experimental Procedure

The general experimental procedure in this research consists of several signal processing stages. LabVIEW software was employed to define the excitation signal as 5 sinusoidal cycles of in a Hanning window. The electrical signal was generated using an arbitrary function generator (Agilent 33220A). A signal amplifier (Krohn-Hite 7600M) was used to amplify the excitation signal to about 200 Vpp, and the amplified signal was applied to the transducer to excite mechanical waves in the plates using the piezoelectric effect. The vibrometer controller (Polytec OFV-5000) was connected to the laser head (Polytec OFV-505) which was mounted on a two dimensional scanning system. The propagated waves were measured at different locations on the plate. The measurement position was controlled using LabVIEW. The laser interferometer was used to measure the velocity of the out-of-plane displacements to record the first antisymmetric wave mode (A_0). The measured signals were filtered using a low-pass and high-pass filter (Krohn-Hite 3945), set respectively above and below the excitation center frequency in the plate. The employed frequency window for the filter (4^{th} order Butterworth) had a range of ±25% of the center frequency. The signals were recorded using a digital storage oscilloscope (LeCroy 9304) with typically 10,000 points in the time domain and averaged 20 times to improve signal-to-noise ratio. Finally, the signals were transferred to a computer for further processing. All measurements have been performed at room temperature.

3.1.3 Transducers

The transducers used in the experiments were built for this project in-house [12]. Based on previous experience the PZT transducers have been found to function well in the desired bandwidth for the excitation frequency (60 - 140 kHz). For some experiments the PZT transducers have been additionally employed in the frequency range up to 200 kHz. The PZT disc (Ferroperm Pz27, 5mm diameter, 2mm thickness) was bonded to the backing mass (Fig 3.2) using two component epoxy adhesive. The dimensions of the backing mass (brass cylinder, 5 mm diameter, 6 mm height) were designed to provide a suitable transducer performance for the excitation frequency range. The manufactured PZT transducer was glued to the plate using the same epoxy adhesive. Thin wires were used to connect to the top of the active PZT disc via the backing mass.

The transducer and setup were grounded by another wire connection between the amplifier and the surface of the plate.

The employed A_0 wave mode in the experiments was typically excited at 100 kHz, for which the used transducer has shown good performance. The diameter of the PZT transducer (Fig 3.2) is about a quarter of the wavelength at 100 kHz excitation frequency for the A_0 mode (bending). Therefore, in good approximation, the transducer can be considered as a point source, point receiver for the excited wave mode in the plate and distributed sensor SHM applications. The PZT disc used in the transducer for this research was excited significantly below its resonance frequencies. The PZT disc is polarized through the thickness, contracts and expands in the thickness direction with the applied voltage, and thus exerts mostly an out-of-plane force on the plate. The transducer has shown good performance above 50 kHz, with the performance dropping off above 200 kHz. For higher excitation frequencies the influence of cross contraction, boundary layer, diameter and frequency on the excitation of the A_0 and S_0 wave modes was investigated in more detail by Giurgiutiu [40]. The frequency-thickness range is sufficiently below the cut-off frequencies of the higher wave modes.

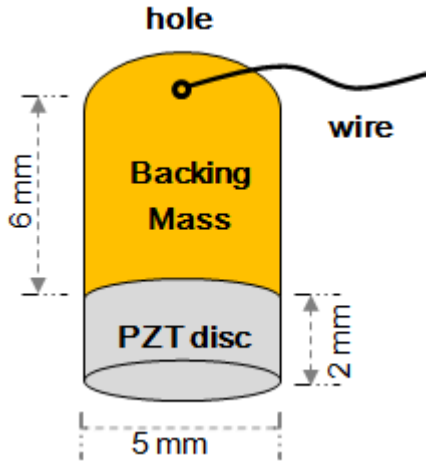

Fig 3.2 Schematic of the PZT disc (Ferroperm Pz27, 5mm diameter, 2mm thickness) glued to backing mass (brass cylinder of 5 mm diameter and 6 mm height).

Based on the chosen excitation frequency and bandwidth, limited pulse distortion is predicted with reasonably constant group velocity limiting the pulse distortion (Fig 2.3).

3.2 Phase and Group Velocity Measurements

As the guided wave dispersion relations for a steel plate are similar to those found for an aluminium plate, measurements were initially performed in an aluminium plate because it is lighter and easier to handle in the lab. An available aluminium plate (size: 1 m × 0.7 m, 3 mm thickness) was used to measure the A0 mode wave propagation, and to calculate the phase and group velocity. Displacements of the A0 Lamb wave mode were measured at three different locations, 200 mm, 201 mm and 300 mm from the excitation transducer, using the laser interferometer (Fig 3.3). The transducer was located 200 mm and 300 mm distance respectively from the side edge and the bottom edge of the plate. The A_0 Lamb wave mode was excited at excitation frequencies ranging between 50 and 150 kHz with a 10 kHz step. The filter cut-off frequencies were adjusted above and below the excitation frequencies at ±25% of each center frequency in the investigated range. The recorded signals in the time domain were analysed and the results are presented in Chapter 5.

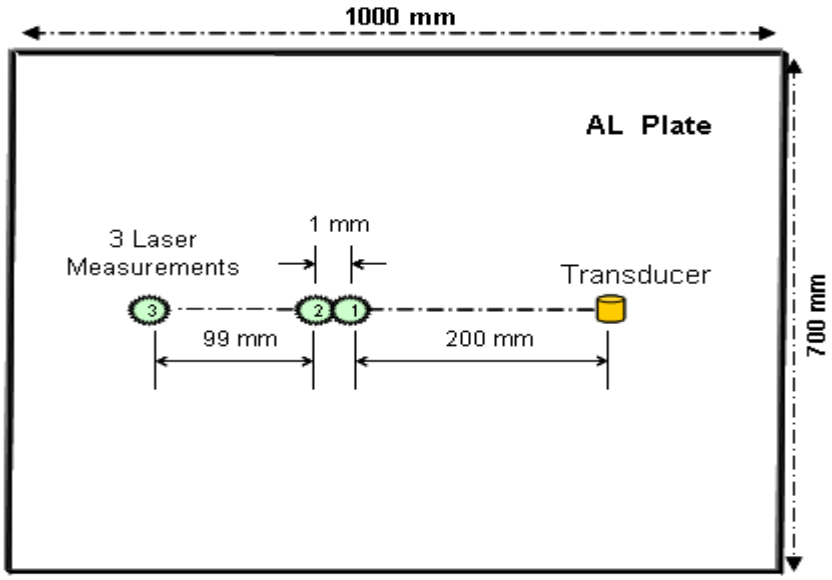

Fig 3.3 Schematic of an aluminium plate (1000 mm, 700 mm and 3 mm thickness) with measurements at (1) 200 mm , (2) 201 mm and (3) 300 mm from excitation transducer.

The laser measurements at 200 mm and 201 mm from the excitation location have been used to calculate the phase velocity by calculating the change in the phase angle. The measurements at 200 mm and 300 mm from the excitation location have been used to calculate the group velocity from signals with a large difference in the arrival time. The envelopes of the measured signals were calculated using Hilbert transform, and the maximum of the envelopes was detected to calculate the corresponding arrival times. The group velocity was obtained using the time difference (arrival times of the two measurements) and the distance between the two measurements (100 mm).

3.3 Defect Localization Array

The propagation of the A_0 Lamb wave mode in a large plate has been used in this experiment to localize an artificial defect (glued mass) using one excitation source point and laser measurements at different locations. The defect in the experiment was simulated by a cylindrical mass (5 mm diameter and 6 mm height) to avoid damage to the plate. The location of the PZT excitation transducer was chosen at 300 mm distance from the plate corner in the x and y directions (Fig 3.4). The laser measurements were performed at different locations (x = 300 mm, y = 500 mm), (600 mm, 500 mm), (600 mm, 200 mm) and (300 mm, 200 mm) on the plate. Baseline measurements were carried out before adding the artificial damage to the aluminium plate, placed at 100 mm in the x direction from the excitation point (Fig 3.4). The second group of the laser measurements was performed again at the same monitoring locations after adding the cylindrical mass (size: 5 mm diameter and 6 mm length). Sufficient time separation was maintained between the reflected waves from the artificial defect and the plate edge. The obtained measurements have been analyzed and evaluated. The signal processing method that has been used to detect and localize the defect is explained in Chapter 6.

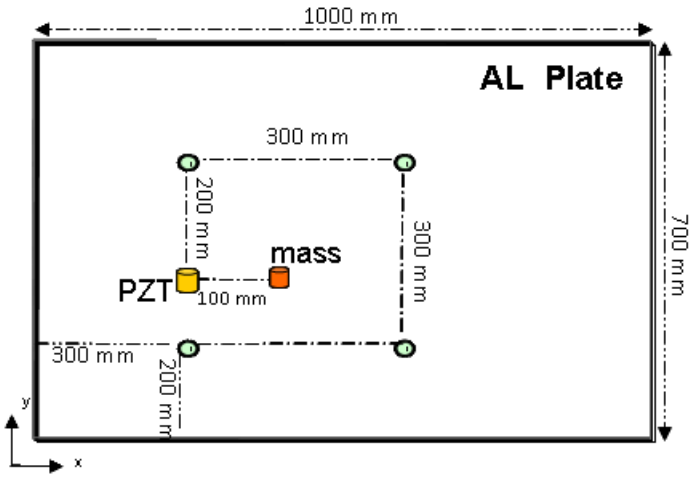

Fig 3.4 Schematic of the array monitoring setup showing one excitation point (yellow) and four monitoring points (green) on aluminium plate to localise an artificial defect (orange).

3.4 Transmission and Reflection Measurements at a Stiffener

The A_0 Lamb wave mode transmission and scattering at a stiffener have been measured in this experiment to calculate the coefficients of the transmitted and reflected waves from a stiffener. Measurements were performed ahead of and behind a stiffener with L-shaped cross-section (size: 50 mm x 50 mm, 5 mm thickness) welded to a steel plate (size 2 m × 1 m; 5 mm thickness). Metal inert gas (MIG) was used for welding the stiffener. Similar L-shaped stiffeners are found on ship hulls, about 200 - 400% the size of the modelled stiffener, with a typical size of about 100 mm to 200 mm length in each side of the L-shape and 10 mm to 20 mm plate wall thickness. The laser measurements were performed at 100 kHz, 150 kHz and 200 kHz excitation frequency to study the dependency of the wave propagation on the excitation frequency. In the first stage, lines of measurements at normal and oblique directions across the stiffener were performed to calculate the transmission and reflection coefficients at specific incident angles, 0^o and 45^o (Fig 3.5). The spacing between the measurement points on the lines was 1 mm in the normal monitoring across the stiffener (0^o), and 1.4 mm at 45^o incident angle to match the settings used for the FE simulations described in the next chapter.

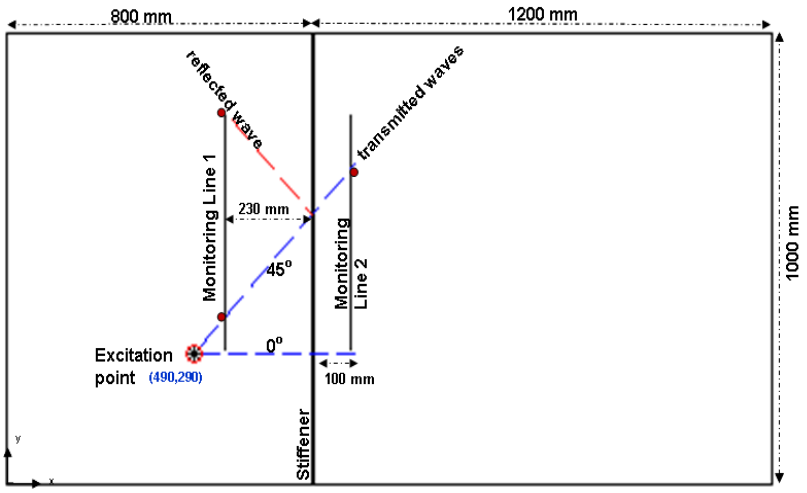

Fig 3.5 Plate schematic showing lines of measurements for calculating the wave scattering at stiffener in specific directions (0^o & 45^o) and at a range of incident angles (0^o - 45^o).

The transmitted and the reflected coefficients at a range of incident angles across the L-shaped stiffener were investigated in the second stage of the experiment. The measurements were performed on lines parallel to the stiffener to optimize the required datasets for calculating the coefficients of the transmitted and reflected A_0 Lamb wave mode in a range of directions 0^o - 45^o. Two parallel lines of measurements were measured in front of and past the stiffener at 230 mm and 100 mm from the stiffener sides respectively. Each monitoring line consists of 400 measurements of 1 mm step size in the y-direction. The obtained measurements, across the stiffener, in front of and past the stiffener, have been used to calculate the transmission and reflection coefficients in Chapter 7. Scattering from a stiffener of rectangular cross-section has been predicted. However, the experimental validation could not be performed because the stiffener weld was not adequate (Fig 3.6), and the weld geometry was large relative to the 20 mm stiffener height. Furthermore, the weld quality and geometry varied significantly along the weld length.

Fig 3.6 Large steel plate with welded stiffener of rectangular cross-section (5 mm thickness).

The weld (Fig 3.6) had a roughly triangular shape, extending more than 5 mm in the vertical and horizontal directions, significantly large compared to the stiffener thickness of 5 mm and the wavelength at 100 kHz. The weld was found to be quite uneven along the stiffener as can be observed in Fig 3.6, showing several gaps in the weld material.

3.5 Defect Localization behind Stiffener

The normal reflections of the A_0 wave mode from an artificial slot machined behind a stiffener welded across the width of steel plate were detected and characterized experimentally. Notch location, excitation and monitoring points have been optimized numerically to maintain sufficient time separation between reflected pulses from the stiffener and the slot in the signal. The reflection from a notch 200 mm past the stiffener, in the normal direction, was recorded for damage detection. Experimental measurements using one-side-access and two-side access in the stiffened plate have been carried out. The scattering of the A_0 wave mode was measured in front of and behind the stiffener, respectively at 100 mm and 250 mm from the stiffener, to validate the numerical predictions (Fig 3.7).

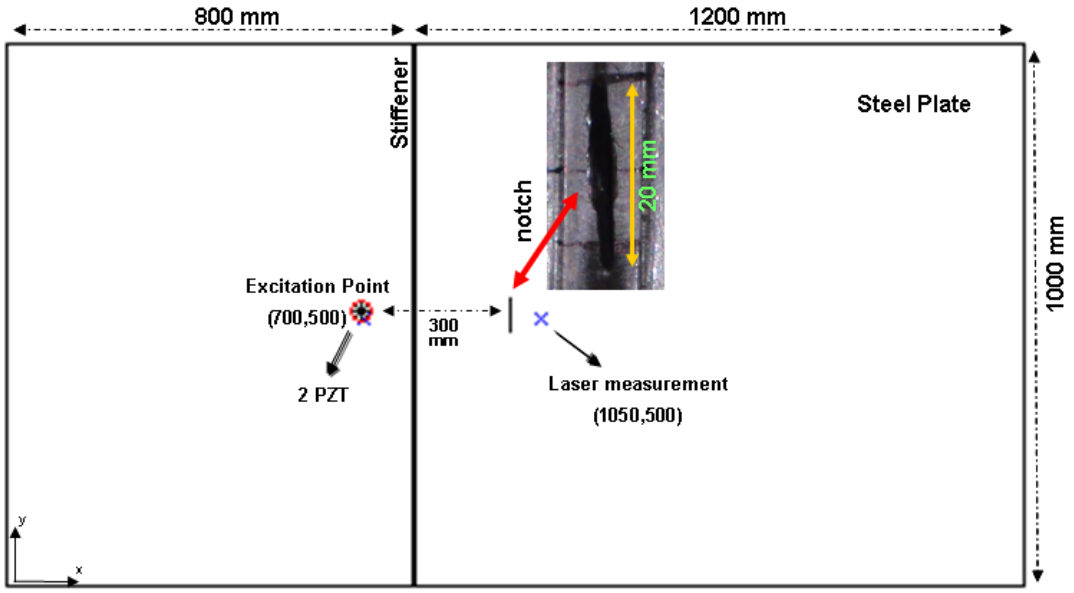

Fig 3.7 Schematic of A_0 mode excitation and reflection from notch (20 mm) behind stiffener shows wave measurements using PZT (at excitation zone) and laser beam (50 mm behind notch).

Two piezoelectric transducers were glued next to each other in front of the stiffener (100 mm from the stiffener), one of them to excite A_0 wave mode and the other to measure the stiffener and slot reflection. Additional laser measurements were performed on the opposite side of the stiffener behind the slot to check the possibility of detecting the scattered wave field at that location. Experimental measurements at 100 kHz excitation frequency were performed before and after cutting the slot in the plate to find out the residual signal after baseline subtraction. The signal processing steps that were carried out to evaluate the measured signals have been discussed in Chapter 9.

In conclusion, Lamb wave propagation and scattering in large plates were investigated experimentally. A low frequency range was used to measure the phase and group velocity. The A_0 Lamb wave mode has been used to detect and localize damage in an aluminium plate. The structural damage in the plate was simulated by an added mass. One excitation transducer and four laser measurements were used to monitor wave propagation with and without damage. The transmitted and reflected Lamb waves at a welded stiffener in a large steel plate have been investigated experimentally. Lines of laser measurements at normal and oblique directions across the stiffener have been used to calculate the transmission and reflection coefficients at specific propagation

direction. Two parallel lines of measurements in front of and behind the stiffener were carried out to reduce the required measurements in each propagation direction across the stiffener. The experimental measurements have been employed to characterize the wave scattering from a defect located past a stiffener in the plate structure. The normal A_0 wave mode scattering from an artificial slot machined past the stiffener was measured based on the access to the stiffener sides in the plate. Similar plate and stiffener geometries were modelled in the next chapter using the FE method, and the numerically predicted guided wave propagation was compared to the experimental measurements.

Chapter 4

Finite Element Simulation

Numerical simulations have been employed to validate the experimental results, and to reduce the required laboratory work in the next stage of this research. The Finite element (FE) method can provide numerical solutions for the wave propagation and scattering in 2D and 3D structures, for different plate dimensions and excitation parameters. Therefore, it has been chosen to model the Lamb wave reflection from defects and surface features. FE simulation has been employed in this chapter to predict the guided wave propagation for plates. The possibility of detecting the A_0 Lamb wave mode reflection at defects was investigated. Wave transmission across a stiffener on a steel plate has been simulated and is discussed at the end of the chapter.

4.1 Stability of the FE Model

The generally well known stability criteria that have been used for the FE model in this research. Adequate choices for the characteristics of the elements such as the element type, material behaviour, size and the number of nodes in each element are necessary to obtain the required stability of the simulation results. One of the initial procedures in creating the FE model is calculating an element size that will provide model stability. The stability in the simulated model can be achieved when the wavelength of the excited mode equals at least 8 elements as a minimum (Eq 4.1) [27]. The shortest wavelength within the excitation bandwidth was used to determine the element size that ensures a stable model. The maximum distance between linear elements in the wave propagation direction (elastic 8-node brick) was calculated using the following stability condition [28],

$$\frac{\lambda_{\min}}{\max(\Delta x, \Delta y, \Delta z)} \geq 8 \ \textit{elements} \quad \textbf{Eq 4.1}$$

The excitation of the A_0 Lamb wave mode was at 100 kHz frequency (f), giving wave propagation at 1870 m/s phase velocity (C_p) in an aluminium plate. The required number of elements per wavelength to provide stability for the plate model in the propagation direction (x-direction) is approximately 8 -10 elements. This number and the length of the propagated pulse (Eq 4.2) were used to calculate the maximum size of the element (Eq 4.3).

$$\lambda_{\min} = \frac{C_p}{f} = 18.7 \ mm \quad \textbf{Eq 4.2}$$

$$\therefore \Delta x, \Delta y \ \textit{and} \ \Delta z \ \textit{should be} \leq 2.33 \ mm \quad \textbf{Eq 4.3}$$

Investigating the required number of elements for model stability through the thickness requires *a priori* knowledge about the mode shape through the thickness. In the case of the A_0 excitation at 100 kHz in a 5 mm thick aluminium plate, the mode shape of the Lamb wave (Fig 4.1) shows that the out-of-plane displacement can be approximated using two elements across the thickness. However, the in-plane displacement requires a higher number of elements through the thickness to accurately describe the mode shape. Four linear elements through the thickness can provide good approximation for the in-plane and out-of-plane components. Modelling wave propagation at high frequency thickness products requires up to 20 elements per wavelength [40] for good approximation and model stability. In general, for high excitation frequencies smaller elements are required to reduce the numerical dispersion and model the wave propagation accurately.

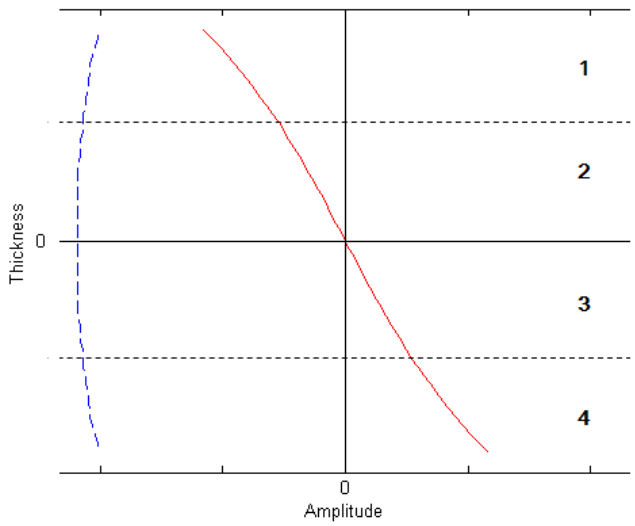

Fig 4.1 A_0 mode shape (0.5 MHz mm) showing in-plane (blue dashed line) and out-of-plane (red line) displacements, with 4 elements through the thickness indicated.

The chosen element dimensions (Δx, Δy and Δz) in the aluminium plate models (3 - 5 mm thickness) were 1 mm in the x and y direction. Four elements have been used through the thickness as this is compatible with the stability criteria and gives sufficient details about the modelled mode shape based on the used wavelength. The time for the wave to travel between two nodes inside an element can be calculated. The interval of the monitoring time, the simulation time step (Δt) needs to be chosen smaller than this time to ensure stability of the numerical simulation. The dependency of the wave velocity on the excitation frequency and propagation direction is a nonphysical effect called numerical dispersion. This undesired effect that inherently presents in the time steps is considered a source of instability in the modelling method. In fact, the interval of the monitoring time is found to be the primary cause of instability in the FE model. Applying smaller time steps in the FE model can be an effective way to reduce the effect of the numerical dispersion on the FE simulation. Studying the accuracy and the stability of the numerical results are the key objectives of these models. The velocity (V_p) of the plate wave (Eq 4.4) has been calculated from Mindlin theory [5], where E, ρ and ν are Young's modulus, material density and Possion's ratio respectively. Taking this as the maximum expected wave velocity, the maximum permissible time step (Δt) to fullfil the stability requirements was calculated employing the element dimensions (Eq 4.5).

$$V_p = \sqrt{\frac{E}{\rho(1-\nu^2)}} \quad \text{Eq 4.4}$$

$$\Delta t = 1 \Big/ C_p \sqrt{1 \Big/ \Delta x^2 + \Delta y^2 + \Delta z^2} \quad \text{Eq 4.5}$$

The brick element type C3D8R was employed in the simulations of this research. From the above relationships, it can be concluded that for the 8-node brick elements, $\Delta x = \Delta y = \Delta z = 1$ mm, the compatible time steps with stability criteria in the simulated models were $1x10^{-7}s$.

4.2 ABAQUS Input File

In this research project, the FE method was utilized to simulate the propagation and scattering of the GUW in plates using a commercial software package (Abaqus/Explicit). This software employs explicit time integration to find time-domain solutions for the propagated wave. A pulse of 5-cycle tone burst was used to simulate the A_0 Lamb wave mode at various excitation frequencies ranging between 50-150 kHz. The Matlab files used for automatically creating Abacus input files were developed based on an MSc project in the Mechanical Engineering Department, UCL [70]. The original input file, which has been used at the beginning of the PhD project as an introduction to understand the required tools for modelling plate structures, simulates a simple plate shape. The Abaqus input files consist of several definitions for the parts of the modelled setup that contain the number of nodes and elements in each part. Creating a model using the graphical interface of Abaqus can require rather long calculations for the exact number and locations of nodes and elements in the model. A Matlab command file can therefore be used to overcome this problem and easily create an input file. Easier parameter variation can be obtained with exactly the same grid by involving Matlab code in defining plate size, defect dimensions, element size and the number of elements per row (in x, y and z-directions). Input data and dimensions can be defined in the first section of Matlab program. The other required sections in the input file were described also in the Matlab file. For example, parts assembly, time interval, material properties, boundary conditions and the requested structure for the output file

can be specified. The excitation parameters and the monitoring locations on the plate model can be varied very easily in Matlab.

The Cartesian coordinates of the 8 corners in the plate were calculated by Matlab, and appeared at the beginning of the input file. These coordinates were used later to generate and number all plate nodes. The main advantage of using Matlab was that it can automatically calculate the node number in each direction using a regular grid of nodes. Master nodes were used to create the master element. Then the rest of elements in the plate were generated and numbered in Matlab using the master element and the iteration of the elements in the x, y and z directions. The output database requests that produce the model elements and the propagated energy along the plate were created by Matlab at the end of input file. The Matlab program gives further flexibility in changing the excitation parameters such as the location of the excitation point and the excited frequency. In fact, employing Matlab code can reduce the effort that needs to be carried out for each FE simulation. The novelty in the modelling part of the research lies in employing Matlab code to automatically generate the FE models of a plate containing a stiffener and defect. The new code gives control over the stiffener shape and geometry, and can be employed to automatically change the length, depth, and location of the simulated notch behind the stiffener.

4.3 Phase and Group Velocity Modelling

The propagation of the flexural Lamb wave mode A_0 has been simulated in an isotropic, homogenous aluminium plate (size: 1000 mm x 700 mm, thickness 3 mm) using the material properties of the laboratory specimen. Matlab code was used to create FE models for various excitation frequencies ranging between 50-150 kHz, the same excitation range that was used in the experimental approach to calculate phase and group velocities (Chapter 5). Out-of plane force was simulated at the excitation location. The excitation point was modelled at 300 mm distance from the origin point at the plate corner in *x* and *y* direction to calculate the phase and group velocity in the plate (Fig 4.2). The A_0 Lamb wave mode propagation was monitored at three locations (200 mm, 201 mm and 300 mm from the excitation point) in the x-direction to replicate the experimental measurements.

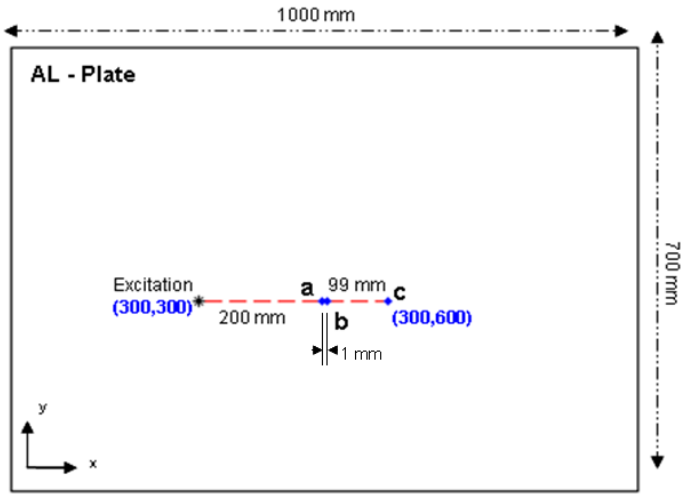

Fig 4.2 An aluminium plate model (1000 mm, 700 mm and 3 mm thickness) with monitoring nodes at (a) 200 mm , (b) 201 mm and (c) 300 mm from excitation point.

Time steps of $1x10^{-7}s$ were used to fulfil the stability criteria in this model, but the size of the elements has been changed because the number of the through-thickness elements should be an even number. The even number was employed to selectively excite A_0 mode by using the out-of-plane component in the middle of the plate thickness. Model parameters that can provide stability for the propagated wave along the plate have been discussed. Two elements through the thickness can approximate the out-of-plane displacement of the mode shape, whereas more elements are required to obtain a good approximation for the in-plane displacement. At low frequency thickness (0.3 MHz.mm), four elements through the plate thickness ($\Delta x = \Delta y = 1$, and $\Delta z = 0.75$ mm) were found to provide enough details about the mode shape and sufficient for model stability. All tested plates in the experimental approach (Table 3.1) have been modelled in this chapter except the defected plate (number 1) that has been replaced with different plate dimensions to obtain simple and comparable notch and crack model.

4.4 Crack and Notch Modelling

This section focuses on the simulation of the scattering of the flexural wave mode at defects such as a notch and a crack. A structural health monitoring system has been simulated to mimic wave propagation and scattering in an isotropic, homogenous aluminium plate (size: 600 mm x 600 mm, thickness 4 mm) using the FE method.

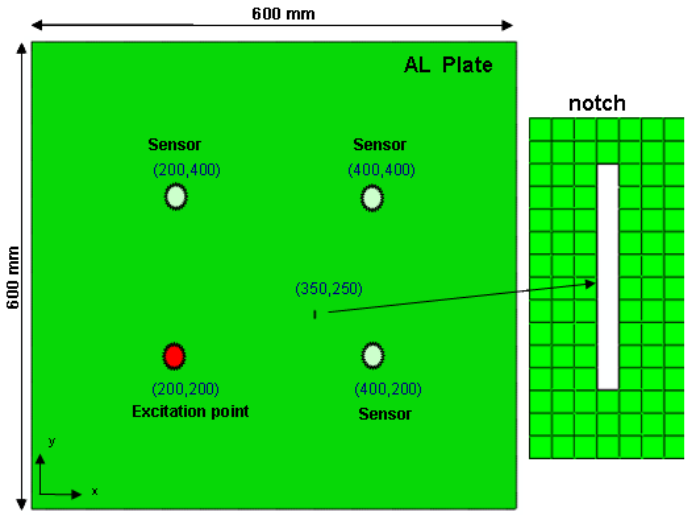

Fig 4.3 FE simulation of aluminium plate (600 mm x 600 mm x 4 mm) with sensor locations and notch (10 mm x 1 mm) shown.

Elements of size $\Delta x = \Delta y = \Delta z = 1$ mm was employed to obtain wave propagation compatible with the stability criteria. The original plate size, which was used in the experimental approach of the defect detection, has been changed in the numerical approach to reduce computational time. The scattering of the A_0 Lamb wave mode at a through-thickness and part-thickness notch (dimensions: 10 mm in y-axis and 1 mm in x-axis) was predicted. A distributed array of four monitoring nodes was modelled symmetrically 200 mm from the plate edges to obtain wave propagation before and after creating the notch (Fig 4.3).

The FE method has been used to simulate baseline data signals, in the first stage, before adding the defect to the plate. In the second stage, the wave propagation was monitored after creating through-thickness (4 mm depth) and part-thickness (1 mm, 2 mm and 3 mm depth) notches in the plate models. The distances from the plate edges to the monitoring nodes were assumed to give sufficient time separation between the reflected signals from the plate edges and the notch signals. The 3D model was run with different excitation locations of the A_0 Lamb wave mode, and the scattering was obtained using a distributed array of monitoring nodes [71]. The notch model was modified to monitor a crack instead of notch in the same plate geometry and using the same distributed array (Fig 4.4).

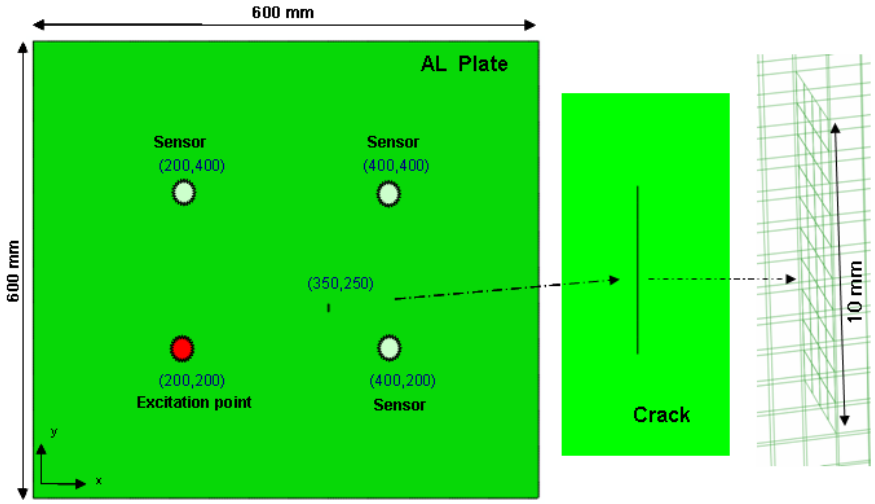

Fig 4.4 FE simulation of aluminium plate (600mm x 600 mm x 4 mm) with crack shown.

The Cartesian coordinates of the defect central point on the x-y plane were chosen at 350 mm and 250 mm from the origin point on the plate edge (Fig 4.3 & 4.4). The modelled notch and crack were 10 mm length. Input parameters such as plate and defect dimensions, meshing size and the number of elements were defined in the first part of Matlab file. In the second part, the baseline plate model was defined as one block while the plate containing a through-thickness notch was divided into 4 assembled blocks around the notch space (Fig 4.5). Each one of these blocks was meshed with cubic elements of 1 mm length, 1 mm width and 1 mm thickness. In addition to the four assembled blocks that surround the notch, one more block was defined inside the notch space to create the part-thickness notch model.

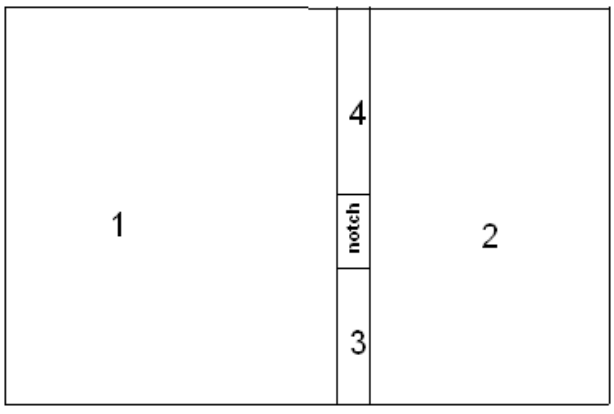

Fig 4.5 Four assembled blocks surrounding the through-thickness notch in the aluminium plate.

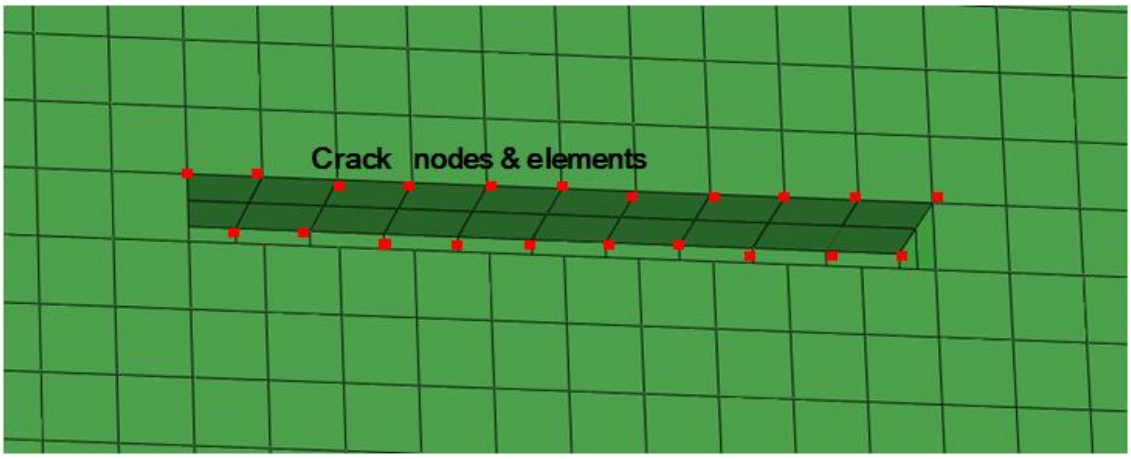

Fig 4.6 Part-thickness crack nodes (red dots) generated along the notch using different numbering system.

Through-thickness and part-thickness cracks were created inside the notch by filling the space between the four blocks (Fig 4.5) with an additional block of elements. The new elements are connected on 3 sides to the existing plate nodes and on the 4th (crack) side to different nodes. Additional nodes along the crack surface were generated automatically (Fig 4.6) using a different numbering system compared to the numbering system that has been used for generating the nodes and elements of the plate. This creates two coinciding surfaces along the crack, which ABAQUS treats as not connected. Thus the finite element model simulates a crack between the plate elements and the new block of elements, that has been generated inside the notch space. For the model that includes a through-thickness crack, the crack elements have been divided into three groups, one in the middle and two at the ends of the crack, to connect the crack to the plate blocks (Fig 4.7). Three additional groups of elements were added to the top of the crack elements to create a model of part-thickness crack open to one plate surface.

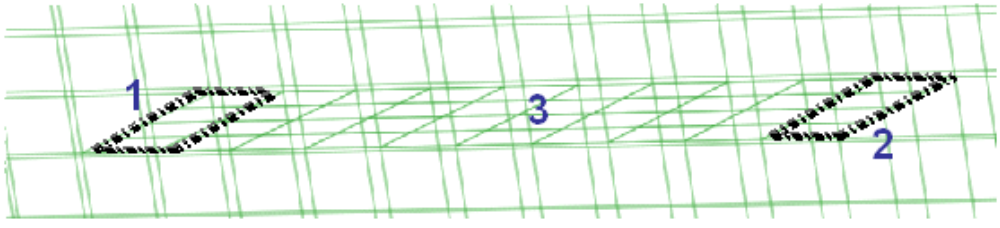

Fig 4.7 Through-thickness crack elements divided into three groups.

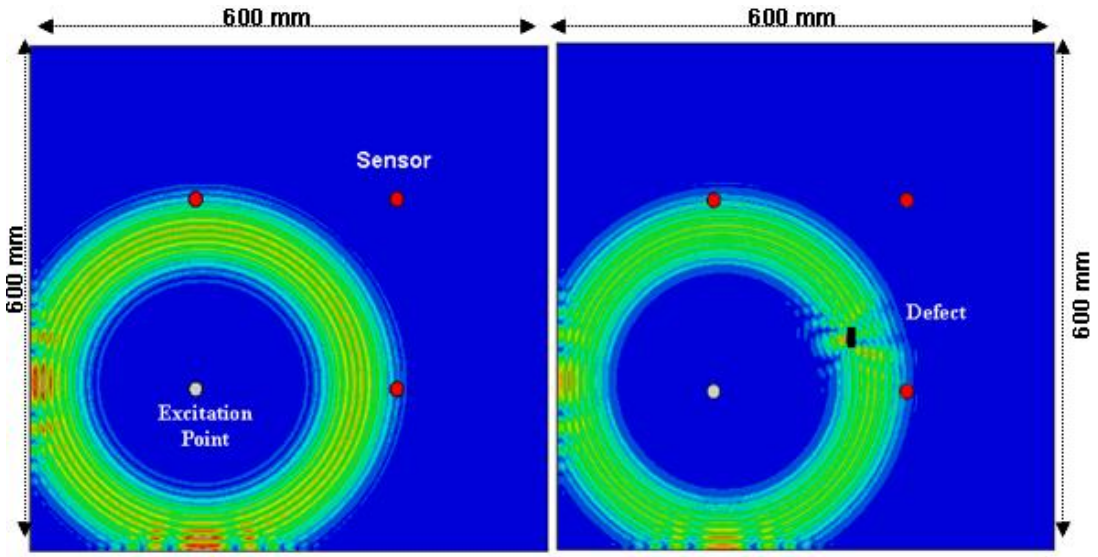

Fig 4.8 Lamb wave propagation in 4 mm thickness of aluminium plate excited at 100 kHz before adding the notch (left) and after adding the notch (right).

The Matlab program can provide automatic implementation for changing the length and the depth of the simulated defect in the model. The problems that a user of Abaqus might face in creating a notch or crack using the graphical interface can be easily solved using Matlab code and an input file. Changing the defect location automatically by calculating the node number of the new location and numbering the defect elements can be performed using a regular grid in Matlab. The effect of the A_0 Lamb wave mode scattering at the notch and the crack have been obtained for several excitation and sensor arrangements. A comparison was performed between scattering fields that show the Von Mises stress in the baseline and defect models (Fig 4.8) to demonstrate the effect of the damage (notch/crack) on the guided wave field pattern.

The propagation and scattering of the A_0 Lamb wave mode have been modelled with and without a through-thickness and part thickness notch/crack for damage localization. The obtained signals from the models have been used to detect the simulated defect in the aluminium plate using baseline subtraction method, and the results have been compared to the experimental outcomes in Chapter 6.

4.5 Stiffener Modelling

Lamb wave scattering at a simulated stiffener across the width of a plate-like model was investigated. The incident and scattered wave at the stiffener were modelled using FE simulation. Both reflected and transmitted guided wave fields at the stiffener location were predicted numerically. In the first attempt of adding a stiffener to the plate model, nodes were generated in a box of nodes that include both plate and stiffener elements. Unused nodes, which were generated in the nodes box beside stiffener nodes, have been removed in the next step to avoid memory problems for high stiffeners. The new model has been used to generate only the useful nodes for plate and stiffener elements. The modified plate model can automatically generate nodes for the plate and the stiffener elements at different sizes. Changing the height and thickness of the simulated stiffener was performed easily in Matlab code to generate the Abaqus input file. Automatic implementation for changing the stiffener location was obtained by calculating the node number of the new location.

Finite element method was used to simulate A_0 wave mode propagation and transmission across a stiffener in a steel plate (size: 1m x 1m, thickness 5 mm). Guided wave propagation and scattering were simulated across a stiffener of 5 mm thickness and 10 mm height. The stiffener, which has a rectangular cross section on the plate, was modelled as perfect contact with the plate and with material properties similar to the plate material. However, the geometry and material of the weld that bond the stiffener to the plate has not been modelled for simplification. The stability in the model was achieved at $\Delta t = 1x10^{-7} s$, $\Delta x = \Delta y = 1$ mm, and to obtain even number of elements in the plate thickness, Δz was chosen as 1.25 mm. The excitation point was modelled at 400 mm and 300 mm from the plate origin on x-axis and y-axis respectively, and 200 mm from the stiffener location in the x-direction (Fig 4.9).

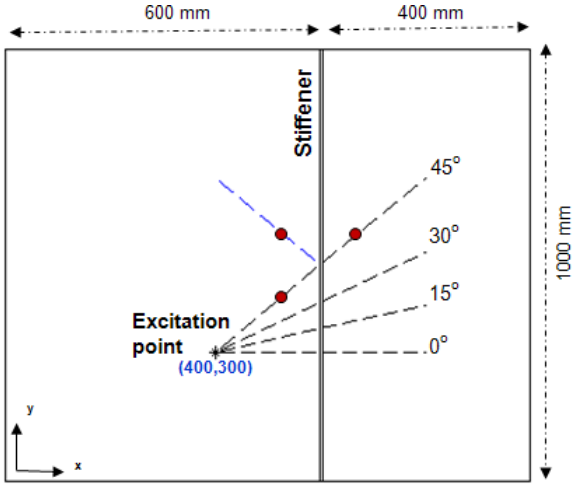

Fig 4.9 Schematic of a stiffener across the width of mild steel plate shows the excitation point and the lines of monitoring points at different wave incident angle.

This model employed the material properties of a laboratory specimen to simulate the excitation of a 5-cycle pulse in Hanning window at 100 kHz. The propagation and transmission of the A_0 Lamb wave mode across the stiffener were observed at several lines of the monitoring nodes, 0^o, 15^o, 30^o, 45^o, starting from the source point. Two parallel lines of monitoring nodes were simulated in front of and past the stiffener at 100 mm from the sides of the stiffener (Fig 4.10), Then the two lines has been simulated at different distances shown in chapter 7, 8 and 9. Each monitoring line consists of 400 monitoring node of 1 mm step on y-direction. The monitoring lines were modelled in parallel to the stiffener to calculate the transmission coefficient across the stiffener at a wide range of incident angles.

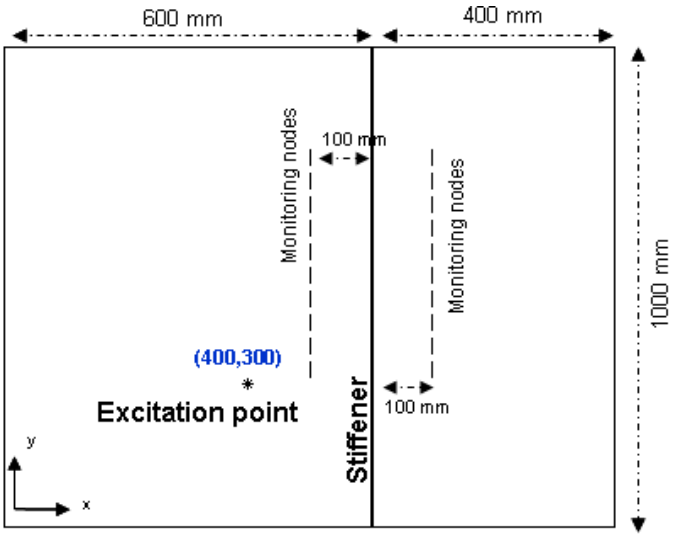

Fig 4.10 Schematic of a stiffener across the width of steel plate showing the excitation point and parallel lines of monitoring points.

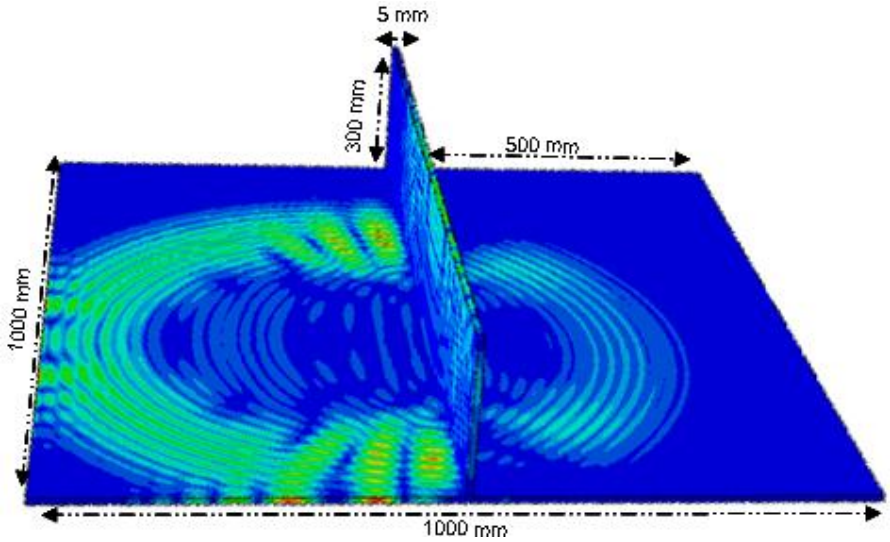

Fig 4.11 Time snapshot of Lamb wave propagation in all directions across a stiffener (size: 1000 mm x 300 mm, thickness 5 mm) simulated across the width of steel plate (5 mm thick).

The simulated data signals, across the stiffener, in front of and past the stiffener, were processed and utilized to calculate transmission and reflection coefficients (Chapter 7). The propagation of the A_0 Lamb wave mode across a high stiffener (300 mm) was predicted using the FE simulation to obtain the scattered field of the GUW (Fig 4.11). The perpendicular transmission and reflection of the S_0, SH_0 and A_0 wave mode at a rectangular shaped stiffener (80 mm height and 5 mm thickness) have been predicted numerically to study mode conversion at the stiffener. The FE method has been used to simulate the excitation of the flexural Lamb wave at 100 kHz in the middle of plate thickness of a steel plate (1.5 m, 1 m and 5 mm thickness), and at 300 mm distance from the stiffener location. A perpendicular line of 600 monitoring nodes at 1 mm step has been modelled to observe the wave scattering at the stiffener, and to calculate the carried energy by each mode. The sum of the transmitted and reflected energies was compared with the energy of the incident wave at the stiffener, and the results have been utilized in the energy balance validation (Chapter 7).

More complicated stiffener shapes such as an L-shaped cross-section was modified using Matlab to simulate the stiffened steel plate (size: 2 m, 1 m and 5 mm thick) available at the Mechanical Engineering Department, UCL. Lines of the monitoring nodes at normal and oblique directions across the L-shaped stiffener (50 mm x 50 mm;

5 mm thick) were modelled to calculate the transmission and reflection coefficients at specific incident angles, 0^o and 45^o. In the second stage, the modelled lines across the stiffener have been replaced by two parallel lines of nodes in front and past the stiffener. The scattering behaviour was predicted at 100 kHz, 150 kHz and 200 kHz excitation frequency to study the dependency of the wave propagation on the used frequency. The predicted wave transmission and reflection at the L-shaped stiffener have been compared to the experimental outcomes in Chapter 7.

4.6 Notch detection behind Stiffener

The numerical approach was used to investigate the possibility of detecting and characterizing a notch behind a stiffener. The normal reflection of the A_0 Lamb wave mode from a notch behind a stiffener was predicted using the FE method. The same notch geometry was modelled at various distances from the simulated stiffener to study the limitations of the detectable defect behind the stiffener. Each plate model investigates wave reflection from one notch at a time. A through-thickness notch (20 mm length) behind the L-shaped stiffener (5 mm thickness) was modelled in a steel plate of size 2 m by 1 m and 5 mm thickness (Fig 4.12). The stability criteria have been achieved using $\Delta x = \Delta y$ =1 mm, Δz =1.25 mm and $\Delta t = 1x10^{-7} s$. The excitation point was modelled at 200 mm in front of the stiffener and in the middle of the plate in the y-direction to ensure sufficient time separation between the incident and reflected pulses in the time trace signals. The normal scattering from a notch behind the stiffener was detected and characterized using two different monitoring approaches, access to one stiffener side only, and access to both sides of the stiffener. Two nodes were simulated at the excitation location and behind the notch to monitor wave propagation before and after creating the notch in the plate model. The transmitted and reflected waves from the notch were analyzed in the time domain before using the baseline subtraction method. The predicted scattering from a notch behind a stiffener has been compared to the experimental results in Chapter 9.

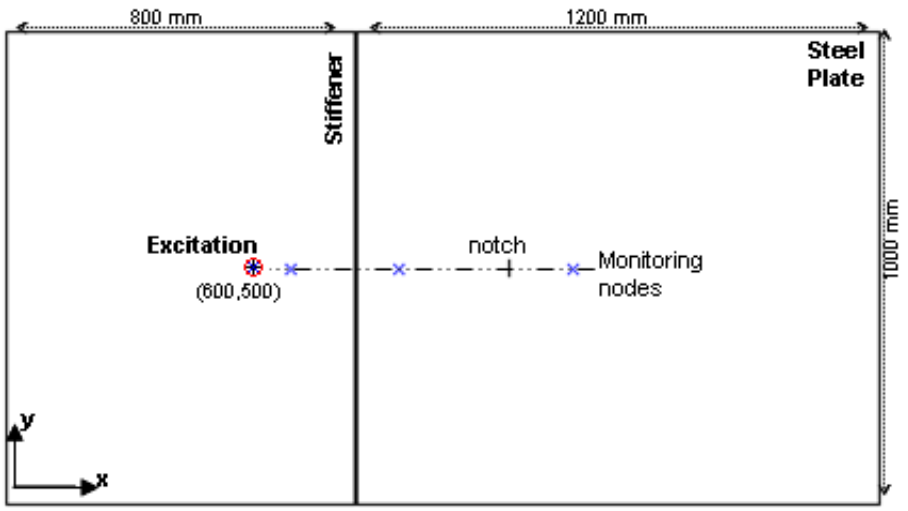

Fig 4.12 Schematic of plate model with stiffener across the width and notch modelled behind it to investigate normal scattering at notch behind stiffener.

4.7 Summary

The propagation of the A_0 wave mode in a metallic plate has been simulated using FE models. The accuracy of the numerical results has been investigated based on the stability criteria of the model. The element size, relative to the wavelength of the propagated mode, and the interval of the monitoring time have been calculated to ensure numerical stability of the FE simulations. Different plate size, defect dimensions and stiffener shape has been simulated using Matlab code. Matlab code has been employed to calculate the number of each node and element in the model, and to provide automatic change for the location of the simulated defect and stiffener. Material properties, excitation parameters, monitoring locations have been changed simply using the Matlab program. The phase and group velocities have been calculated numerically at a low frequency range. Flexural wave mode propagation and scattering from through-thickness and part-thickness damage such as notch and crack have been simulated in a 3D model of the aluminium plate. Wave propagation before and after adding the notch or crack has been predicted to detect and localise the damage using the baseline subtraction method.

The reflected and transmitted waves across a stiffener in a steel plate model have been investigated. Lines of monitoring nodes at normal and oblique directions across the stiffener have been simulated to calculate the transmission and reflection coefficients at specific propagation directions. Quantifying the transmitted and reflected wave from the stiffener at a wide range of angles employing line of monitoring points for each

propagation direction has been substituted by modelling two parallel lines of nodes in front of and past the stiffener using one FE simulation. The scattering of the A_0 wave mode from the notch located behind the stiffener in the plate structure has been modelled. Wave scattering before and after adding the notch past the stiffener has been simulated to characterize the notch reflection using baseline subtraction. Normal wave mode propagation and scattering from a simulated notch located past the stiffener were predicted using access to one or both sides of the stiffener.

Chapter 5

Phase and Group Velocity

This chapter investigates the phase and group velocity of the A_0 wave mode propagation in large plate structures at low frequency-thickness products. Furthermore, the chapter aims to show the dispersive behaviour of the A_0 Lamb wave mode below 0.5 MHz.mm. An aluminium plate has been used in this chapter, instead of the actual stiffened plate (steel) that is going to be used later in the main part of the research, to reduce surface preparation work. The phase and group velocities of the propagated wave have been calculated based on experimental measurements. The predicted A_0 wave mode propagation using the finite element method has been used to calculate the phase and group velocities. A further theoretical approach has been employed to validate both experimental and numerical results based on well-established correlation. The match between the outcomes of the used techniques can justify using the theoretical prediction for calculating the velocity of the propagated wave in a different plate material such as steel plate.

5.1 Theoretical Approach

Studying the characteristics of the A_0 Lamb wave mode is a crucial step for calculating the wave velocity. The simplest approach that describes flexural wave propagation in a plate and takes into account bending stiffness (Classical plate theory) was modified by Mindlin [5] to include shear and rotary inertia as mentioned in Chapter 2. The behaviour of the A_0 Lamb wave mode was investigated theoretically using the propagation velocity of the excited wave. Group velocity *(C_g)* can be calculated from the dispersion relation [3] as:

$$C_g = C_p + k\frac{dC_p}{dk} \quad \text{Eq 5.1}$$

$$C_p = \frac{2\pi f}{k} \quad \text{Eq 5.2}$$

The mathematical relation shown in Eq 5.2 has been used to calculate the phase velocity (C_p), where f stands for wave mode frequency, and k is the wave number. Substituting Eq 5.2 into Eq 5.1 gives the calculated value of the group velocity. Mindlin theory [5] was employed to calculate the wave number (k) for a variety of frequency content, where κ the correction factor, $\kappa^2 = \pi^2/12$, and V_p plate wave velocity (Eq 5.3).

$$V_p = \sqrt{\frac{E}{\rho(1-\nu^2)}} \quad \text{Eq 5.3}$$

$$k = \pm\frac{1}{V_p\kappa}\sqrt{\frac{\omega}{2h(1-\nu)}}\sqrt{h\omega(2+\kappa^2(1-\nu)) + \sqrt{12V_p^2k^4(1-\nu)^2 + h^2\omega^2(2-\kappa^2(1-\nu))^2}} \quad \text{Eq 5.4}$$

Matlab code was employed to generate the vector of the angular frequencies (ω) and to calculate the wave number (Eq 5.4). The plate parameters that were used for this approach, such as Young's modulus (E), Poisson's ratio (ν) in addition to material density (ρ), were considered based on the standard values of the aluminium alloy 2014-T6 (Table 5.1).

Table 5.1 Material Parameters of the Aluminium Plate 2014-T6.

Parameters	Mindlin & FE	Units
Young's modulus (E)	$7.3\text{x}10^{10}$	N/m^3
Poisson's ratio (ν)	0.33	--
material density (ρ)	2800	kg/m^3
plate thickness ($2h$)	3	mm

5.2 Disperse Code

Disperse code is a modelling software that employs a numerical solution for analytical equations to create dispersion curves for different geometries and material properties. The results of this interactive Windows code were used to verify the Mindlin theory. The software has been developed at Imperial College to predict the features of the propagated wave in different structures [7]. The behaviour of the A_0 Lamb wave mode propagation in pipes and multilayer structures can be investigated easily using Disperse software.

5.3 Experimental Approach

The piezoelectric transducer, described earlier in Chapter 3, was employed in this approach to excite the A_0 Lamb wave mode in an aluminium plate (size: 1 m, 0.7 m, 3 mm thickness). Wave measurements were performed to calculate the phase and group velocities using the experimental setup that has been presented in Fig 3.1. Short time sinusoidal signals were used to excite the A_0 Lamb wave mode in the aluminium plate at 10 kHz frequency steps varied between 50 - 150 kHz.

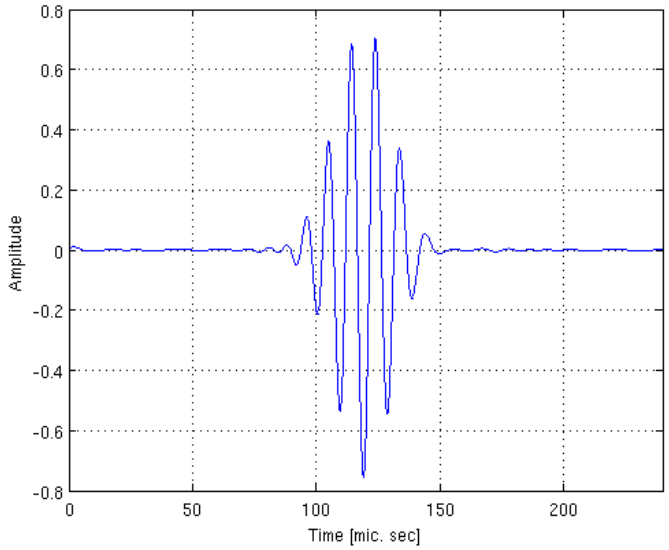

Fig 5.1 Typical A_0 Lamb wave measurement of 5-cycles sinusoidal signal in Hanning window excited at 100 kHz central frequency in 3 mm plate thickness.

The excitation point was chosen at 300 mm distance from the plate edges in the *x* and *y* direction. Full time trace signals for 5-cycles in Hanning window were observed at three locations, 200 mm, 201 mm and 300 mm from the excitation point in the *x* direction (Fig 5.1). The excited wave mode (A_0) in the plate has significant out-of-plane motion, which has been observed using laser interferometer. The full time trace signals were loaded into a Matlab file to be processed. The noise in the time trace signal was filtered employing high-pass and low-pass filters. Data signals were time-gated to separate the plate edge reflection and capture only the direct incident pulses. Phase and group velocities were calculated using the analytical procedures that have been described by Staudenmann [72]. Fourier transforms of the analysed signals were used to calculate the phase angles. The change in phase angle ($\Delta\psi$) was used (Eq 5.5) to calculate the phase velocity (C_p), where (Δx) is the distance between the monitored locations on the plate (Fig 4.2).

$$C_p = 2\pi f \frac{\Delta x}{\Delta \psi} \qquad \textbf{Eq 5.5}$$

Δx was chosen typically small (1 mm) to avoid the effect of 2π jumps in the calculation of the phase velocity.

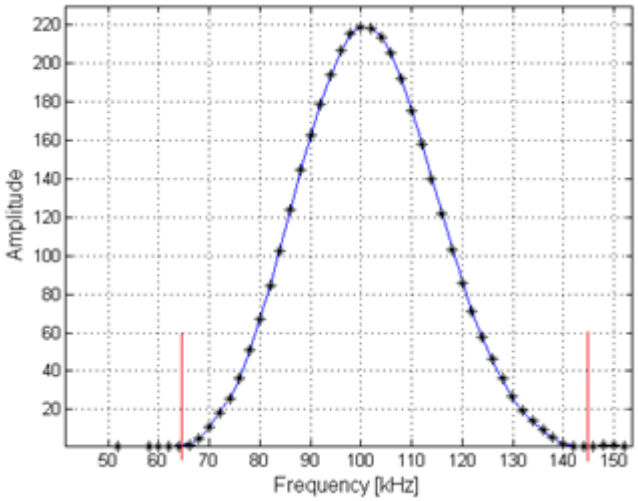

Fig 5.2 Fourier transform of time trace signals excited at 100 kHz central frequency and measured at 200 mm (solid line) and 201 mm (star line) from the excitation point in 3 mm thick plate.

The above figure (Fig 5.2) demonstrates the frequency content of the time trace signal shown in Fig 5.1. At 100 kHz center frequency there is amplitude content from approximately 65 kHz to 145 kHz. Fourier transform was used to calculate the amplitude of the propagated wave at 5 kHz frequency steps within the observed frequency range around the central frequency (Fig 5.5).

Calculation of the group velocity has been described earlier (Eq 5.1). The monitoring locations were placed at sufficient distance (Δx) to obtain a large time difference in the time trace signals that were used to calculate the group velocity (Fig 5.3). The measured time trace signals with 100 mm propagation distance (Fig 4.2) were processed. These signals were filtered above and below the excited frequency in the plate using a HP/LP filter. The utilized frequency window for the filter was in a range of ±25% of the central frequency. The envelopes of the filtered signals were obtained using Hilbert transform. The maximum of the envelopes was calculated in the time domain (Fig 5.3). The indices of the maximum amplitude in the pulses were calculated. These indices were used to calculate their corresponding arrival time and the difference of the arrival time (Δt).

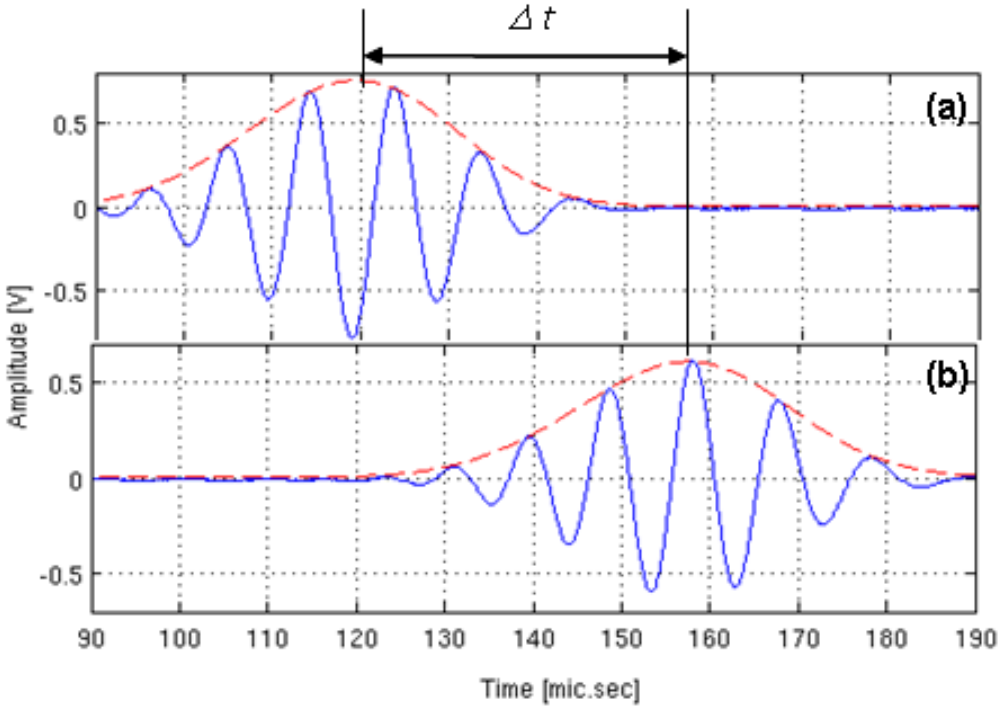

Fig 5.3 Envelopes (dashed lines) of the measured (solid lines) time trace signals at (a) 200 mm and (b) 300 mm from the 100 kHz excitation in 3 mm thick plate.

The difference in the arrival time was substituted in (Eq 5.6) to find the group velocity, where Δx is the distance between the monitoring locations.

$$C_g = \frac{\Delta x}{\Delta t} \quad \text{Eq 5.6}$$

After that, the obtained group velocity has been used to calculate the arrival time in the measured and simulated time trace signals.

5.4 Finite Element Approach

Wave propagation along an isotropic, homogenous 2014-T6 aluminium plate (size: 1000 mm x 700 mm, thickness 3 mm) has been simulated using an explicit FE model (Chapter 4) to validate the experimental findings of the phase and group velocities. The excitation and monitoring of the out-of-plane wave mode was simulated in the middle of the plate thickness at 300 mm distance from edges (Fig 4-1), using the same material properties that were used in the experimental approach. Measurements of the wave propagation at three locations (200 mm, 201 mm and 300 mm from the excitation point) on the x-direction were modelled to simulate the experimental signals. The simulated time trace signals at three monitoring locations were used to calculate the phase and group velocity.

5.5 Verification of the Phase and Group Velocity

Several approaches such as Mindlin theory, Disperse code, the FE method and experimental measurements have been used to calculate the phase and group velocity. The velocity of the A_0 wave mode propagation in an aluminium plate for a variety of frequency-thicknesses products has been predicted using Disperse software [7]. Matlab code was used to obtain the Mindlin theoretical solution for the wave number in the velocity calculations, and to compare the results for the phase and group velocity (Fig 5.4).

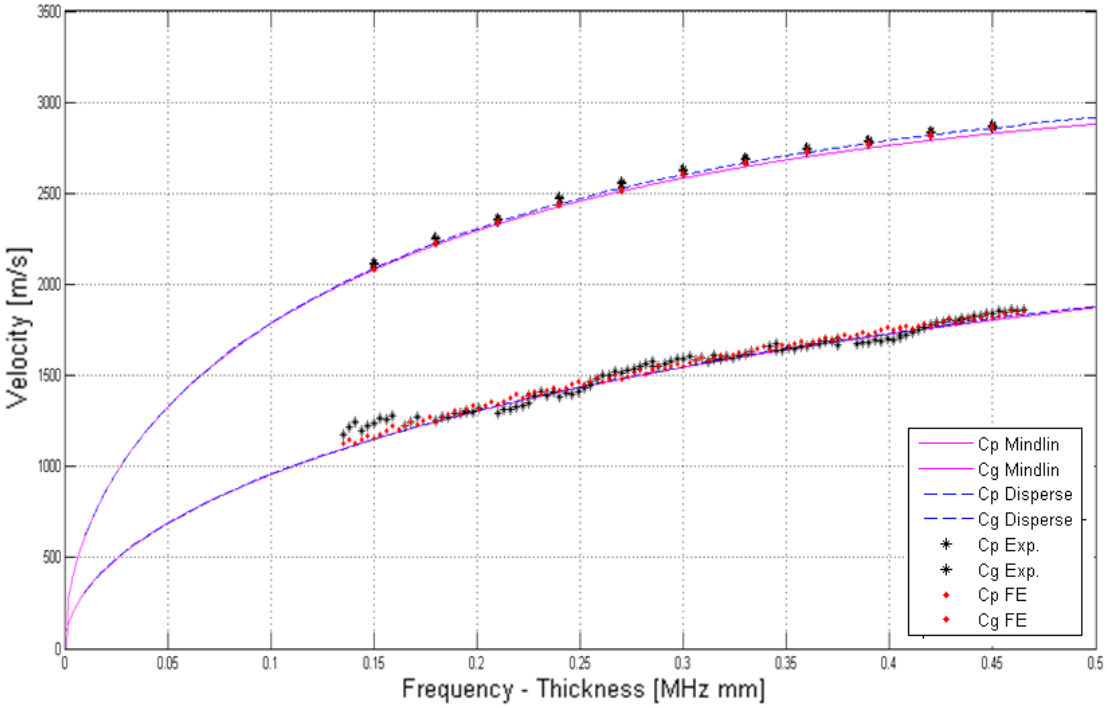

Fig 5.4 Dispersion curves showing phase velocity (lower line) and group velocity (upper line) of A_0 mode in aluminium plate utilizing FE method (red, diamonds), Mindlin theory (pink), Disperse software (dashed blue) and experimental approach (black, stars).

In the FE prediction and experimental measurements, the phase and group velocities were calculated for a range of frequency contents between 50 - 150 kHz (Fig 5.4). Fourier transform was used in the above curve to calculate the phase angles of the predicted and measured time trace signals at 11 excitation frequencies with 10 kHz frequency spacing. The phase velocity was calculated with 1 kHz interval around each excited frequency, and represented by 10 points on the phase velocity curve. On the other hand, for the group velocity curve one point at the excitation frequency for each wave measurement (maximum of the envelope) could be evaluated. Up to 400 kHz.mm frequency thickness product the curve (Fig 5.4) still shows dispersive behaviour for the propagating A_0 Lamb wave mode. The group velocity increases from 2080 m/s at 50 kHz to 2840 m/s at 150 kHz. For 100 kHz a group velocity of 2600 m/s was predicted. The group velocity values are significantly higher than the predicted phase velocity values, e.g., the above figure shows 1550 m/s phase velocity at 100 kHz. In general good agreement between the theoretical predictions, FE and experimental results can be observed in figure 5.4. However, the recorded time trace signal at 100 kHz (Fig 5.1) did not show significant distortion in the 5-cycles pulse shape. The short travel distance from the point source to the monitoring point (100 mm) was not sufficient to show

significant change in the pulse length and energy. A comparison between the used approaches has shown reasonable agreement on the velocity of the propagated wave [66] (Table 5.2).

Disperse code is considered to be the most accurate approach in calculating the phase and group velocity since it solves the three dimensional theory of the wave propagation that includes all possible wave modes. The dispersion curve (Fig 5.4) shows that a very good match was achieved between Mindlin theory and Disperse code in the group velocity with a maximum error of less than one percent at high frequency. Signal processing can produce systematic errors. To reduce the error, the simulated time trace signals were filtered using HP/LP filters and then time-gated. The Disperse theoretical approach has shown a good match with the findings of the FE prediction, though a small error was observed in the group velocity comparison (0.6%). The experimental measurements were expected to give the maximum error, which was found to be 1.2% at 0.24 MHz.mm, whereas a good agreement was achieved in general between the theoretical and experimental findings of the group velocity. On the other hand, the maximum error in the phase velocity calculation, 2.2%, was obtained at 0.14 MHz.mm using the measured time trace signals.

Table 5.2 Phase and group velocity of the A_0 Lamb wave mode at 100 kHz excitation frequency in 3 mm thick aluminium plate.

Approaches	**Phase Velocity** (m/s)	**Group Velocity** (m/s)
Mindlin	1545	2598
Disperse	1676	2633
Experiment	1585	2625
FE	1552	2604

The source of the error in the calculation of the phase and group velocity in the experimental measurements could possibly be related to the accuracy of the material properties such as Young's modulus, Poisson's ratio and the plate density. The difference to the FE simulations can be minimized (0.2%) by increasing the Young's modulus of elasticity from $7.14x10^{10}$ to $7.19x10^{10}$ N/m^2. Moreover, varying the plate density in the calculation of the phase and group velocity can bring about a significant change in the overall error. The uncertainty in material properties and noise level were found to be sources of error in the experimental approach.

In conclusion, understanding of the behaviour of guided ultrasonic waves is important and can be achieved by studying the effect of the frequency change on the wave velocity. The phase and group velocities of the A_0 Lamb wave in plate-like structures have been investigated using several approaches to verify the accuracy of the experimental findings. Results from the Disperse program and Mindlin theory were compared to the FE method. Good agreement can be observed when comparing the theoretical and experimental results. Errors in the experimental results were found to be reasonable and could possibly be reduced by improving the accuracy of the material properties. Finally, the used methods in this chapter will be employed in the next chapter for localizing damage in a large plate structure.

Chapter 6

Defect Localization using Distributed Array

This chapter aims to investigate analysis methods that have been used in the current research to detect and localized damage in a large plate structures. The output from the finite element models simulating Lamb wave propagation and scattering at different excitation/monitoring arrangements (Chapter 4) has been analysed in this chapter. Different types of simulated damage e.g. notches and cracks were localized in this chapter using the obtained time trace signals. The time trace signals, which were obtained experimentally in Chapter 3 for an artificial defect (mass glued to plate), have been evaluated and compared to the results of the simulation models.

6.1 Signal Processing for the FE model

Wave propagation and scattering in an aluminium plate, size 0.6 m x 0.6 m, have been modelled using the FE method. Initially a plate thickness of 4 mm was modelled to obtain an even number of elements in the thickness direction for cubic elements (1 mm edge length). Afterwards, the modeled plate for the defect detection investigation has been modified to the thickness of 5 mm of the stiffened steel plate. Four excitation and measurement locations (point force nodes) were modelled symmetrically 200 mm from the plate edge (Fig 4.3) to localize a simulated notch by exciting an A_0 Lamb wave mode at one node and monitoring the received wave signal at the three other nodes. The employed wave mode in the simulation has been exited using a center frequency of 100 kHz, as the A_0 Lamb wave mode propagation at this frequency thickness range has shown only limited pulse distortion. Moreover, at this frequency range the A_0 mode was found to provide reasonable sensitivity to small defects (wavelength about 18.7 mm).

The central point of the defect was located at 350 mm on the x-axis and 250 mm on the y-axis from the origin of the plate model (Fig 4.3). The propagation distance from the excitation point to the notch, then to the monitoring nodes was calculated for every excitation/monitoring combination. Time trace signals were obtained from the FE model of the wave propagation which contains several pulses. Initial processing for the simulated time trace signals was performed to identify the effective time window for the associated pulses. The first pulse in the baseline signal (no defect present) represents the direct pulse from the excitation to the monitoring location. The time trace signals for each sensor combination were normalized to the amplitude of the direct pulse. The other pulses, which follow the main pulse in the time trace signals, are the reflected pulses from the plate edges. The wave propagation was recorded before and after creating the notch in the plate, respectively the baseline and defect signals shown in Fig 6.1.The difference between the baseline and notch data signals was calculated, and the envelope of the difference signal was obtained using the Hilbert transform.

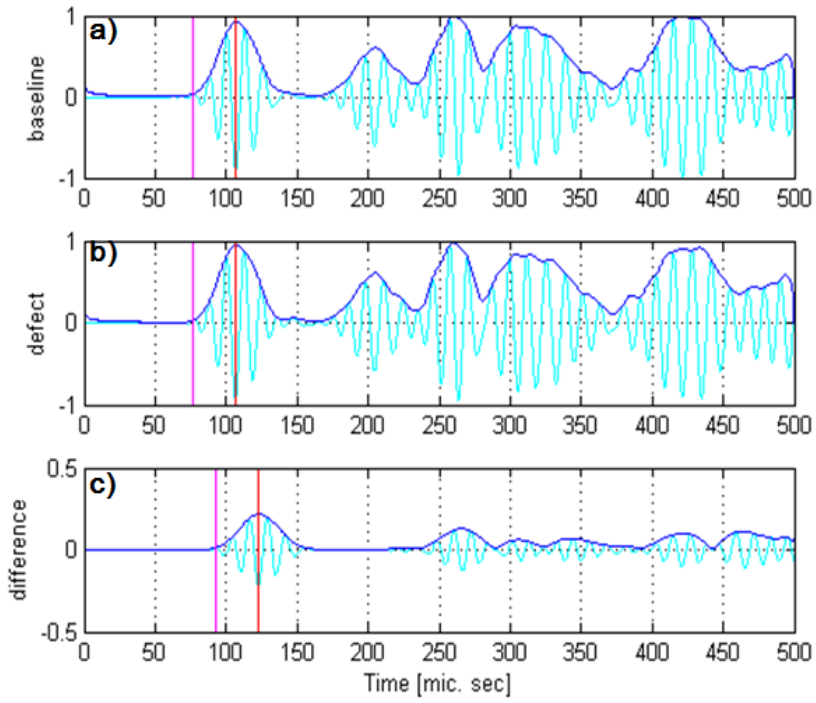

Fig 6.1 Time trace signal of (a) baseline model, (b) defect model (10 mm long notch, through thickness) and (c) time trace difference for A_0 mode propagation in aluminium plate (4 mm thick)at 100 kHz, showing envelope maximum (red line) and expected arrival time (magenta line).

Significant amplitude was observed in the difference signal after baseline subtraction (Fig 6.1), in the order of 10 - 20% of the baseline signal. The actual arrival time (AAT) of the simulated pulse, which represents the propagation and scattering in the simulation period, was calculated using the arrival time of the maximum amplitude of the signal envelope (red vertical line). The travel distance from the excitation location to the simulated defect and then to the monitoring location was calculated. The first arrival time, shown on the above figure (Fig 6.1c), was calculated using the travel distance and the group velocity (magenta vertical line). The subtraction of the baseline from the notch signal (difference signal) has shown secondary pulses in addition to the notch reflection in the difference signal. The additional pulses that arrive after the notch pulse in the difference signal are either due to the scattering of edge reflections at the defect or due to the reflection of the initial scattered wave pulse at the plate edges. Several paths of the scattered wave can produce the additional pulses that appear after the notch pulse in the difference signal (Fig 6.2).

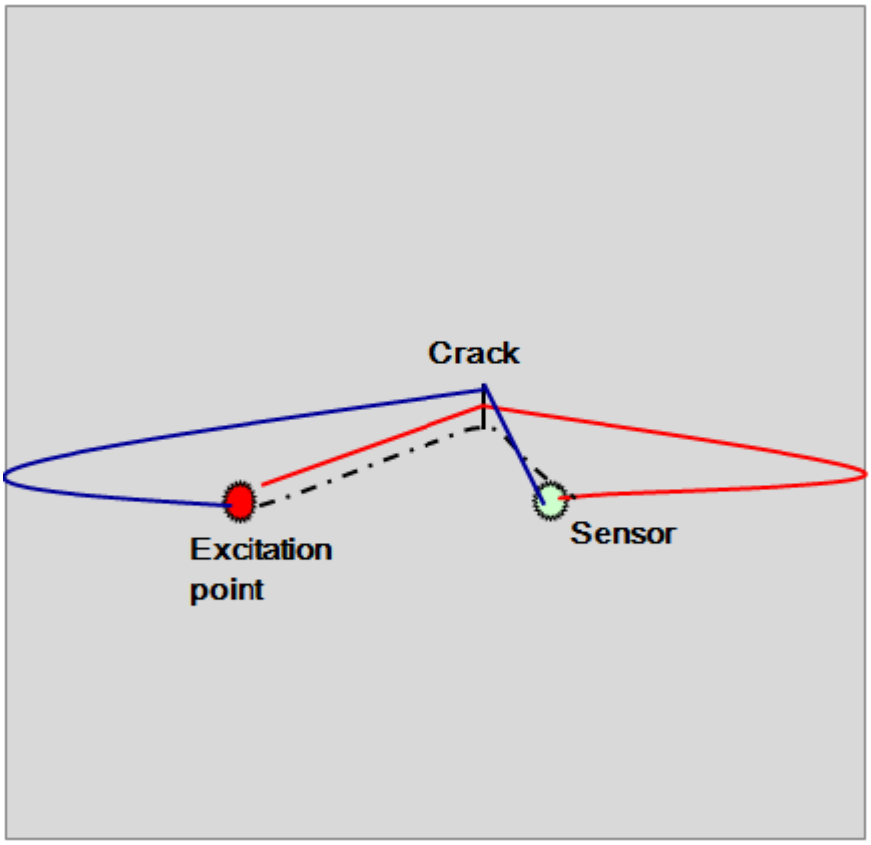

Fig 6.2 Three possible wave paths; dashed line: direct scattering at defect to sensor; red line: reflection of scattered wave at plate edge; blue line: edge reflection scattered at the crack

Signal processing has been performed on the simulated time trace signals to obtain the required accuracy in the group velocity value. The first arrival time was compared to the AAT to verify the observed results. Good match was obtained between the predicted and calculated arrival time in the baseline model, defect model and time trace difference.

6.2 Ellipse Localization Method

The presence of a defect and its location can be detected using several methods. A signal processing algorithm has been developed in Matlab to localize the simulated notch (10 mm length) based on the simulated time series for the different excitation/sensor locations. The travel distance has been calculated using the group velocity and arrival time of the scattered pulse from the notch (maximum of envelope of the difference signal in the baseline subtraction) for every sensor and actuator pair. The locus of the possible damage locations were calculated based on the travel time of the propagated wave. A well-established localization technique from literature [15] was used to determine the crack location based on at least three pairs of transducers. The method can be called the ellipse method of localization since it uses an ellipse shape to obtain potential defect locations. The potential defect locations based on the travel distance form an ellipse around the excitation and monitoring sensor locations (Fig 6.3).

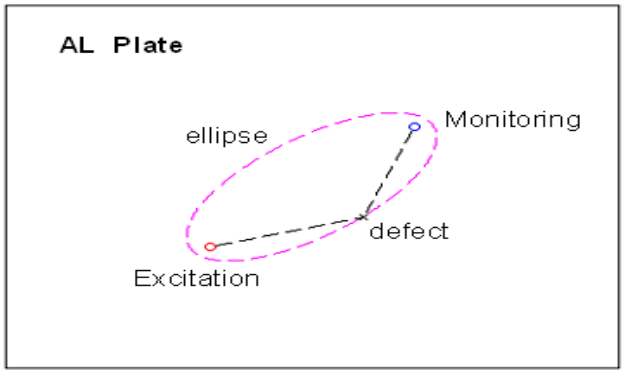

Fig 6.3 Schematic of the Ellipse method showing wave travel distance from the excitation point to the monitoring point via a defect on plate.

The ellipse method has been used in several recent studies [15] as it has important advantages over the other damage localization methods that have been employed with Lamb waves. In comparison to the cross-correlation technique, which requires a distributed array of about 10-15 sensors to determine time delays of the strongest ultrasonic reflection from a defect [78], the ellipse method requires 3 transducers (sensor and actuator pair) to locate similar damage. The arrival time of the first (defect) pulse in the difference signal (Fig 6.1c) has been used together with the sensor locations. The possible wave propagation distance for one excitation/monitoring combination can be illustrated by solving the ellipse equation in Matlab (Fig 6.4a). Applying the ellipse localization method on two different monitoring positions on the plate can reduce the potential defect locations to the intersection of the ellipses at two points (Fig 6.4b). Based on the localization method, the intersection point of the obtained ellipses represents possible damage location in the monitored structure [15]. For more accuracy in defect localization, a locus of six ellipses has been plotted (Fig 6.4c). The intersection area of the ellipses around the damage location was calculated and found to be 10 mm – 15 mm away from the center of the modelled defect (10 mm long notch, Fig 6.4c). In this case, the center of the intersection zone was considered to be the best fit for the ellipses intersection point. The calculated uncertainty around the defect location was found to be acceptable relative to the used wavelength in the model (18.7 mm).

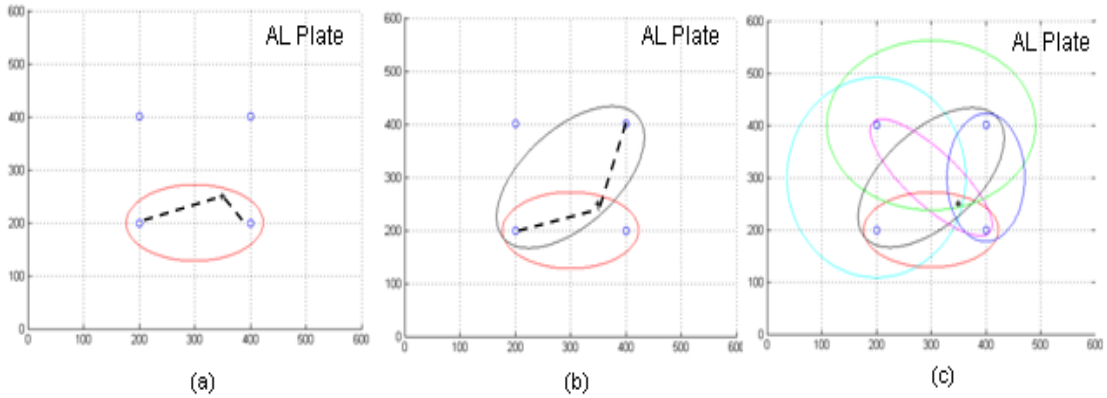

Fig 6.4 Process of defect localization using ellipse method that show excitation/monitoring locations of the simulated A_0 mode in one combination (a), two combinations (b), and six combinations (c) based on AAT for the defect (10 mm notch) pulse.

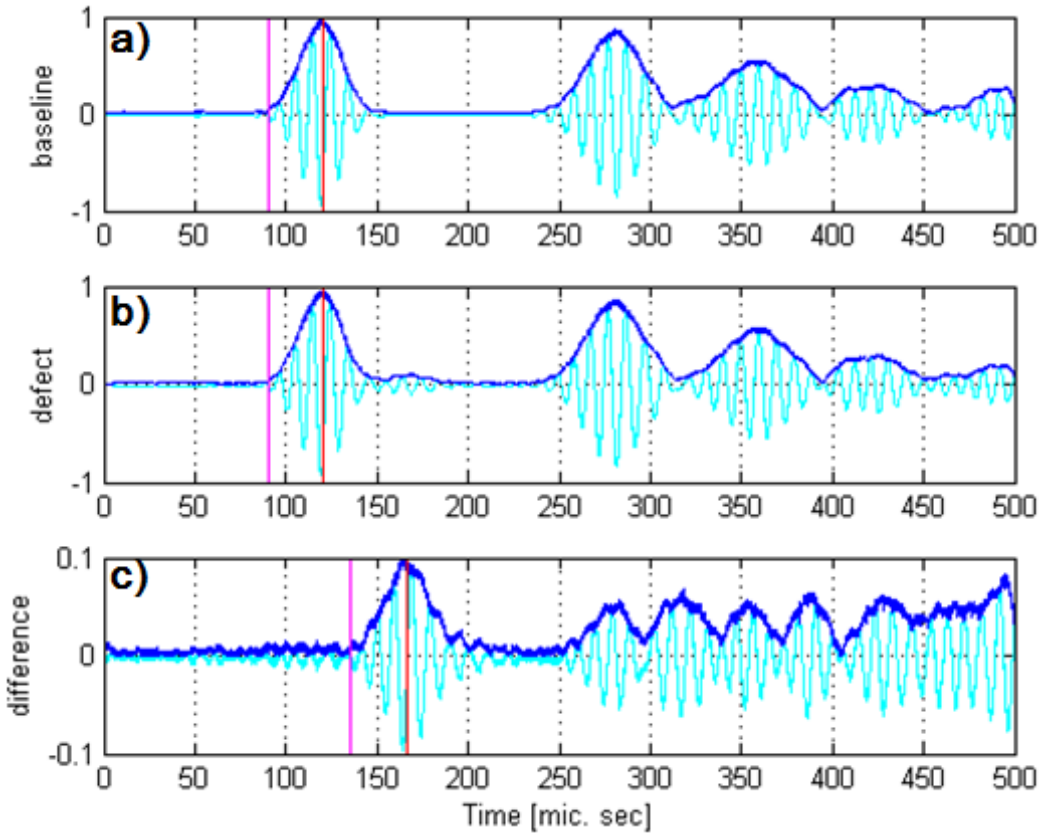

Fig 6.5 Time trace signal of (a) baseline measurement, (b) defect measurement (glued mass) and (c) difference signal for A_0 mode propagation in aluminium plate (3 mm thick), showing arrival time of envelope maximum (red line) and expected arrival times (magenita line).

6.3 Experimental Validation for the Localization Method

A processing algorithm was developed in Matlab to analyse the experimental time trace signals excited by the piezoelectric transducer and monitored in several locations by a laser interferometer. The array measurements have been used to localize a glued cylindrical mass (size: 5 mm diameter and 6 mm length) that represents a defect in the plate structure. The difference between the baseline measurements and the defect measurements was analysed. The maximum amplitude of the Hilbert transform for the experimental time trace signals was calculated similarly to the previous analysis. Figure 6.4 shows the difference between the experimental baseline signal and the defect signal at a monitoring location (600,200) on the aluminium plate. The actual arrival time of the measured pulse (red vertical line) was calculated using the maximum amplitude of the signal envelope, and shown on the time trace signals (Fig 6.5). The first arrival time (travel time) of the propagated wave was calculated using the group velocity (magenta vertical line). Based on the actual arrival time of each pulse and the group velocity, the

localization method was employed to calculate and draw the locus of the travel distance for the first significant difference pulse around the location of the excitation and monitoring sensors. Several ellipses have been used for the different transducer combination to find the intersection point that represents the potential location of the artificial damage in the plate (Fig 6.6).

The location of the defect was captured reasonably well employing the Ellipse method of localization. A reasonably good agreement was obtained between the actual and measured defect location. The error was calculated based on the offset between the ellipses intersection point and the actual defect location. The offset in the notch location for the simulations described above (Fig 6.4c) was found to be less than half of the wavelength, which is similar to the simulated defect size. In contrast, the observed offset from the experimental measurements (Fig 6.6) was about 4 times the size of the glued mass on the plate, equivalent to one wavelength. The defect localization results of the numerical and experimental approaches are found to be as good as expected.

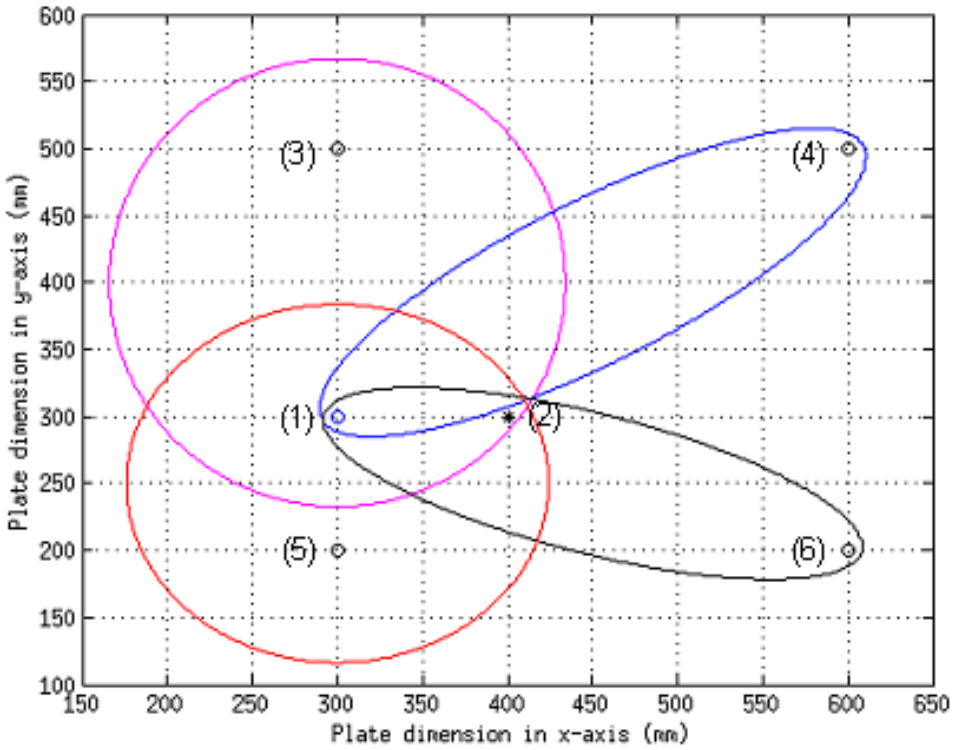

Fig 6.6 Ellipses showing location of cylindrical mass on the aluminium plate, where (1) excitation point, (2) cylindrical mass, (3, 4, 5 and 6) monitoring points.

The maximum spatial resolution that can be achieved was investigated using a synthetic time-reversal imaging method at 200 kHz [38], and found to be 2 – 3 times the wavelength. The obtained resolution in this case was around 150% of the diameter of the scatterer. Further improvement in the image resolution was found to be achievable using advanced back propagation and a parametric inversion method. An alternative damage localization method was used with different vibration modes [79] to detect damage based on synthetic data generated from 3D finite element models. The new method was found successful at locating the damage using a small number of mode shapes identified from baseline structures and damage subtraction. However, this method does not perform well at estimating the corresponding severity of the damage.

To conclude, the modelled and the measured time trace signals in a large plate structure have been processed in this chapter for defect localization. Using the travel time of the scattered pulse the ellipses around excitation and monitoring sensor locations containing potential defect locations have been plotted. The intersection point of the plotted ellipses represents the damage location in the structure. Simulated defect (notch) was localized using this method. Experimental measurements have been performed to validate the numerical approach for localizing damage. Reasonable accuracy between the actual defect location and the intersection point of the ellipse locus has been obtained relative to the defect size and the wavelength of the employed wave mode. Localizing a defect is not trivial, and there are various other localization methods that can be used in the future to improve the accuracy. Wave propagation in more complicated structures, stiffeners and T-joints, usually produce high percentage of pulses overlap in the recorded time trace signal and thus are more complicated to evaluate.

Chapter 7

Reflection and Transmission of Lamb Wave Mode across Stiffener

Understanding the guided ultrasonic wave behaviour in large plates with stiffeners is a crucial step for the detection of structural damage behind the stiffener using the A_0 Lamb wave mode. This chapter will focus on calculating the A_0 mode propagation and scattering across a stiffener to investigate the amount of energy that can be transmitted. The finite element method has been utilised to predict the transmitted and reflected wave from a T-joint weld across the plate width for different wave propagation directions across the stiffener. In this chapter a new approach is developed and validated that employs sets of nodes parallel to the stiffener to monitor wave transmission for a wide range of angles, significantly reducing the simulation effort. The simulated time trace signals were processed to determine the propagation angles at which sufficient energy for damage detection behind the stiffener can be transmitted. The simulation results were verified experimentally. The limitations of the plate geometry, the monitoring zone, stiffener location and excitation locations are essential subjects to address before selecting the monitoring setup for the investigation of the Lamb wave scattering.

7.1 Motivation

The finite element method has been used previously to model the wave propagation across a stiffener in 2D. A separate plane wave model was performed for each propagation direction [35]. The Fourier transform (FFT) was employed in frequency wave number space to determine the wave amplitude at nodes across the stiffener. In contrast, in this project using 3D FE models the real plate geometry has been simulated. The normal and oblique Lamb wave scattering at a stiffener was analysed using the signal envelope in the time domain. Wider observations for the inspected structure can

be provided based on the findings of this research. Eventually, mode conversion should be taken into account to quantify the magnitude of the S_0 Lamb wave mode that has been generated at the stiffener. Calculating the carried energy by the S_0 wave mode that has appeared due to mode conversion from the A_0 Lamb wave mode scattering at the stiffener is important to verify the energy balance between the incident and the scattered waves from the stiffener. Despite the fact that mode conversion occurs for all propagation directions, for simplicity the current research project has only verified the mode conversion at normal A_0 Lamb wave propagation. The future work beyond this project would consider all transmitted and mode converted modes, in a wider range of directions across the stiffener. The FE models, which were used for the A_0 wave mode excitation, can be modified to investigate the S_0 and SH_0 transmission and reflection at the stiffener. These models could be modified, in a further step to investigate different geometries or varying excitation frequency. Experimental measurements were carried out on a welded stiffener to validate the predicted A_0 wave mode scattering.

7.2 Excitation Parameters

This chapter explores in some detail the A_0 Lamb wave mode propagation across a stiffener for a particular set of parameters (stiffener dimensions, excitation frequency). The sensitivity of the transmitted and reflected waves at the stiffener to the parameters listed above was investigated systematically. The A_0 wave mode propagation was simulated in a steel plate (size: 1 m x 1 m, 5 mm thickness). The excitation point was chosen at 300 mm from the bottom edge of the plate and 200 mm from the stiffener location. The stiffener, which has a rectangular cross section on the plate, was modelled as perfect contact with the plate and with material properties similar to the plate material. In addition, the height of the modelled stiffener was shorter compared to the wavelength of the excited wave pulse. Wave scattering at the stiffener location was observed by means of the FE method. Specific signal processing steps were used to analyse the transmitted and reflected pulses at the stiffener.

The minimum required distance between the monitoring location and stiffener is considered as one of the limiting factors for the wave propagation directions that can be

investigated. Sufficient distance between the excitation location and stiffener has to be maintained to obtain a time separation between the incident and reflected wave. Wave reflection from the plate edge can also cause unwanted overlap in time with the incident and transmitted wave pulses at the monitoring location. Therefore, the plate size governs the range of angles that can be used for monitoring wave transmission and reflection from the stiffener. The known distance from the excitation point to each monitoring node has been used with the group velocity of the propagating wave mode to calculate the arrival time of the main pulse. The velocity of the propagated wave at 100 kHz in a 5 mm thick steel plate has been calculated for several guided wave modes (Table 7.1). The propagation of the A_0 wave mode was measured and simulated on a line from the excitation transducer perpendicular across a stiffener [36]. The amplitude of the incident, transmitted and reflected waves from the stiffener were calculated using the complex magnitude of the Hilbert transform of the time trace signals. The reduction in the wave amplitude due to the radial outwards spreading was calculated based on the following relation.

$$A_1^2 r_1 = A_2^2 r_2 \quad \text{Eq 7.1}$$

The reduction in the wave amplitude from A_1 to A_2 (Eq 7.1) was used to calculate the ratio of the transmitted energy through the stiffener relative to the incident waves, whereas r_1 and r_2 are the relevant travel distances from the excitation point to the monitored nodes. The magnitude of one over square root of the travel distance ($1/\sqrt{r}$ curve) has been used to verify the measured and predicted reduction in the wave amplitude due to the radial spreading.

Table 7.1 Group velocity of the S_0, SH_0 and A_0 wave mode in a steel plate of 5 mm thickness at 100 kHz

Guided Wave Modes	Group Velocity (m/s)
S_0	5640
SH_0	3230
A_0	2980

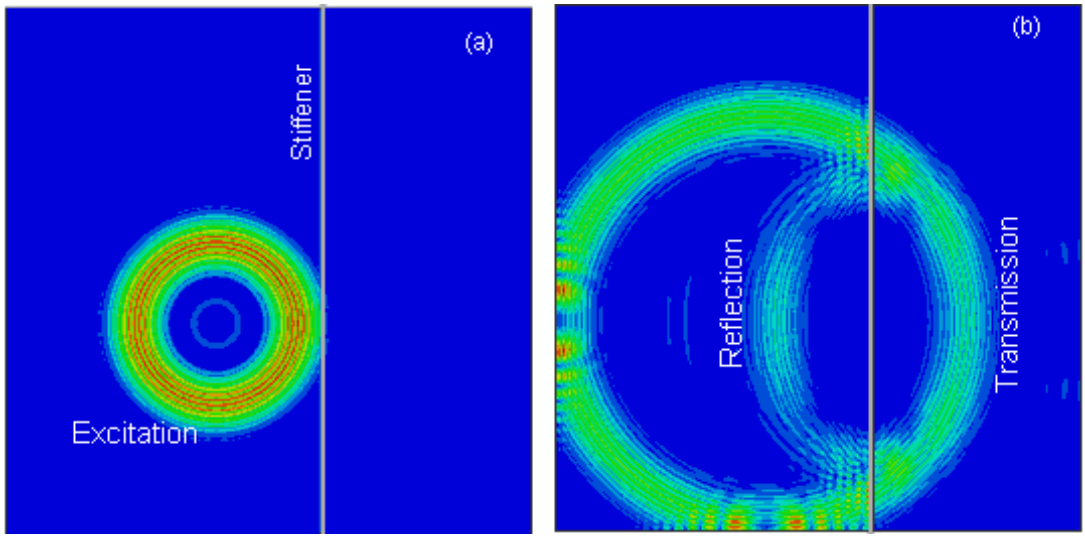

Fig 7.1 Abaqus visualization for A_0 wave mode excitation in steel plate (size: 1 m x 1 m x 5 mm), at 100 kHz (a) left to a stiffener (5 mm thickness, 10 mm height), (b) transmission and reflection from the stiffener.

7.3 Monitoring Lines across Stiffener at Different Angles

Excitation of the A_0 wave mode was modelled in a steel plate (size: 1 m x 1 m x 5 mm). The excitation point was chosen at 400 mm and 300 mm from the plate origin on the x-axis and y-axis respectively. Distance of 200 mm in the positive direction of the x-axis was maintained between the excitation point and the stiffener location. Wave scattering was simulated and observed on both sides of the stiffener. The excitation frequency was chosen as 100 kHz, giving a wavelength of 18.7 mm. The change in the transmitted energy for varying stiffener height and incident angles was monitored (Fig 7.1).

Lamb wave propagation, reflection and transmission across the stiffener are presented at two different times in Fig 7.1 above. Scattering of the A_0 wave mode across a stiffener of 10 mm height and 5 mm thickness have been simulated. For preliminary investigations, the wave transmission and reflection at normal and oblique propagation angles across the stiffener have been monitored. Lines of monitoring nodes have been modelled across the stiffener to investigate the radial spreading of the GUW at several directions 0^o, 15^o, 30^o and 45^o (Fig 7.2).

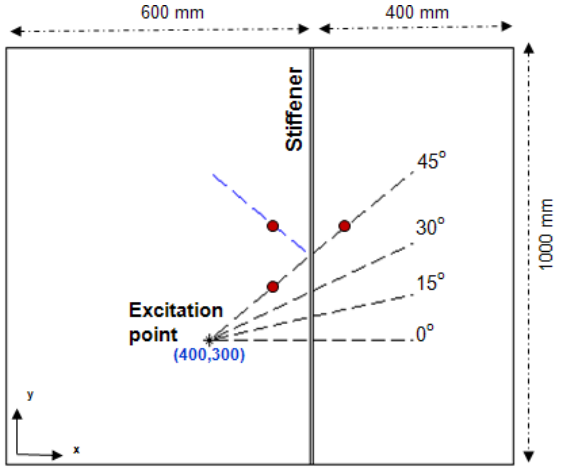

Fig 7.2 Schematic of steel plate showing transmitted A_0 Lamb wave mode across a stiffener in normal and oblique directions (black), and its reflection at 45° (blue).

The maximum of the Hilbert transform has been used to calculate the wave amplitude at the monitoring nodes across the stiffener. The obtained amplitude across the stiffener was normalised to the amplitude of the incident wave at the stiffener location. The simulated amplitude curves were fitted with the theoretically expected $1/\sqrt{r}$ amplitude reduction due to geometrical spreading. Reasonably good fitting has been achieved in front and behind the stiffener (Fig 7.3), especially for the range of angles 0°- 30°. The amplitude reduction for the transmitted wave at the stiffener was found from the fitting procedure.

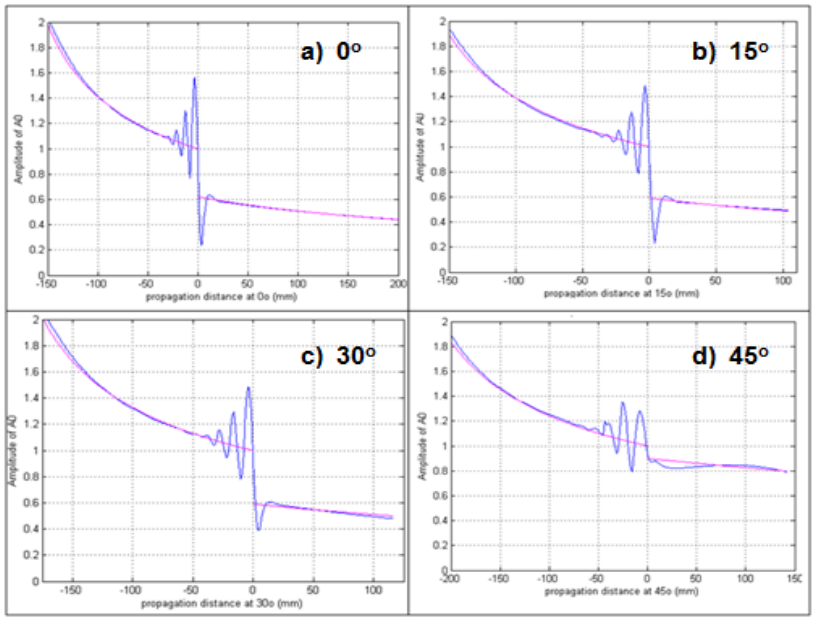

Fig 7.3 Fitting amplitude of monitoring nodes across the stiffener with the geometrical spreading curve ($1/\sqrt{r}$) for different propagation directions.

The amplitude of the incident and transmitted wave at 0^o propagation direction has shown acceptable match with the $1/\sqrt{r}$ curve, especially in the far field zone (Fig 7.3a). Approximately 40% reduction in the wave amplitude can be observed relative to the incident wave at normal propagation across the stiffener. The neglected mismatch that appears between the predicted amplitude and the fitting curve at far distances from the stiffener can be attributed to the dispersion behaviour that the A_0 wave mode shows at 0.5 MHz.mm (Fig 5.4). The incident and transmitted waves at oblique directions (15^o-30^o) across the stiffener have shown amplitude reduction patterns (Fig 7.3b & 7.3c) similar to the pattern that has been obtained at normal wave incident. The amplitude of the transmitted wave at 45^o shows some slight variation around the expected radial spreading curve (Fig 7.3d) with less than 5% amplitude reduction at stiffener location. The variation in the wave amplitude before stiffener could be related to the constructive and destructive interference of the incident and reflected mode. The localized amplitude was found to drop directly behind stiffener due to the thickness change. Other effects were also expected in the scattered wave field at the stiffener due to the unsymmetric thickness change in the plate structure. Scattering of other expected wave modes, S_0 and SH_0, from the same stiffener geometry could be simulated (0^o, 15^o, 30^o and 45^o) using the same FE model. The relative magnitude of the new wave modes could be compared with the scattered A_0 mode at the stiffener to understand how the converted energy from the incident wave mode would be distributed on other scattered modes. The stiffener itself was found to be acting as wave guide for some modes that resulted in mode conversion, as it has been concluded in a previous research [65]. Mostly, the carried energy by shear horizontal modes have shown this behaviour and found to be trapped along the stiffener at mode conversion.

7.4 Monitoring Model for Wide Range of Angles

FE models have been created to quantify the reflected and transmitted wave at a range of incident angles for certain frequency-thickness products. The aim of these models was to study the effect of the stiffener size, plate geometry, excited wave and propagation direction on the transmission and reflection coefficients. Two parallel lines of monitoring nodes have been modelled ahead of and behind the stiffener at 100 mm distances from the stiffener. These lines have been located parallel to the stiffener in

order to obtain the transmission coefficient of the propagating waves at a wide range of directions using less dataset signals. Four hundred monitoring nodes with 1 mm step size in the y-direction have been modelled in each line (Fig 7.4).

Efficient evaluation from simulating two lines of datasets in the time domain was carried out to achieve wave propagation in a range of incident angles using a single FE plate model. Wave propagation across the stiffener was monitored at a range of angles between 0^o and 50^o with an increment of one degree, since the plate geometry prevents investigating propagation directions beyond that. Obtaining the time trace signal for a wider range of incident angles requires increasing the length of the monitoring lines along the stiffener, and maintaining sufficient time separation for the reflected pulses from the stiffener. Processing steps have been developed in Matlab to calculate the travel distance of the propagated waves across the stiffener based on known information about the incident direction and monitoring location. The arrival time of the monitored pulses at the monitoring nodes on the parallel lines was calculated using the travel distance and group velocity. Wave amplitude has been obtained from the maximum amplitude of the signal envelope.

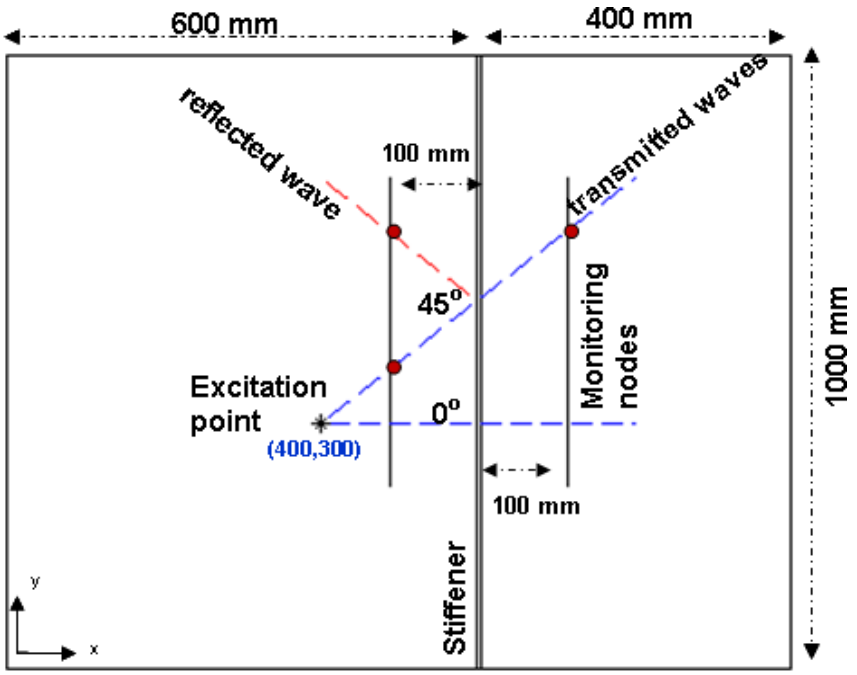

Fig 7.4 Schematic of steel plate showing transmitted A_0 Lamb wave mode across a stiffener in normal direction and oblique direction 45^o (blue) and two parallel lines of monitoring nodes (black).

The reduction in the wave amplitude, due to geometrical spreading, has been obtained mathematically. The amplitude of the incident and transmitted signals in the investigated direction was found based on the amplitude of known signals detected at the closest monitoring points to the wanted direction on the parallel lines of datasets. Interpolation has been performed on the amplitudes of the detected signals (the closest monitoring points to the wanted direction) to calculate the amplitude of the propagated wave in the investigated direction. The amplitude of the incident wave was corrected at stiffener location using the relation of the radial spreading (Eq 7.1). The ratio of the transmitted wave to the incident wave at the stiffener location was used to calculate the transmission coefficient. The percentage of the transmitted wave across the stiffener has been obtained versus the angle of the incident wave. The transmission coefficients of the projected waves at the stiffener location were simulated at 100 kHz for several propagation directions (Fig 7.5).

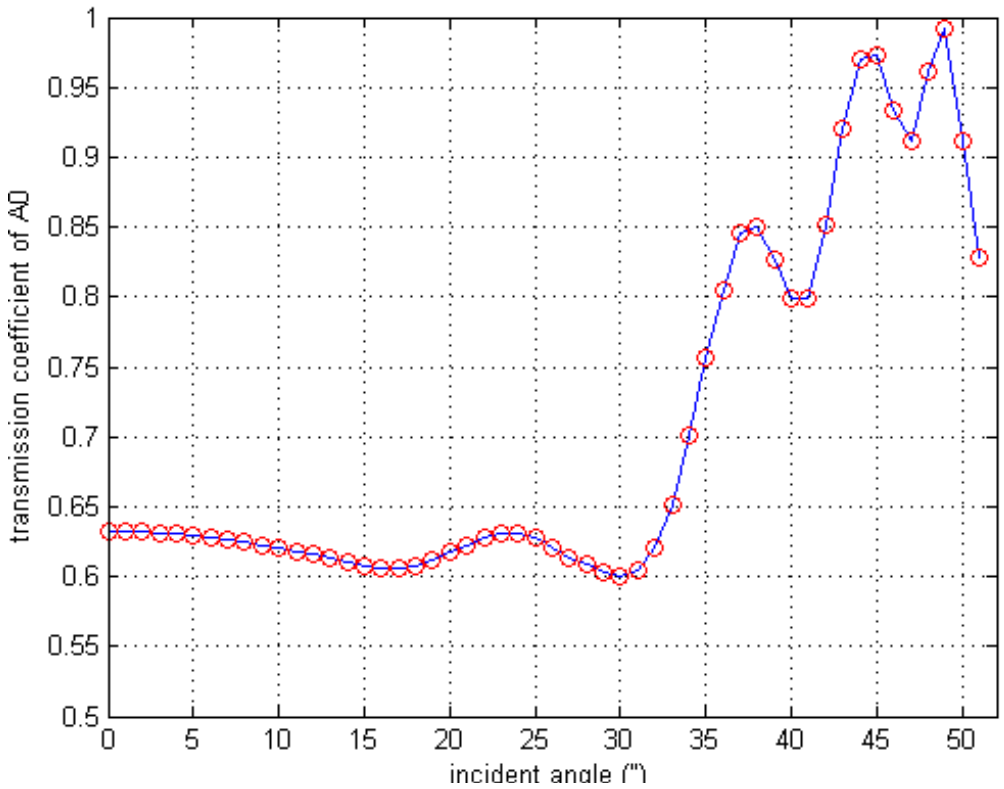

Fig 7.5 Transmission coefficient at a range of incident angles (0^o – 50^o) across stiffener of 10 mm height and 5 mm thickness simulated at 100 kHz.

The above figure 7.5 shows that almost constant transmission coefficients were predicted for incident directions up to 30^o. The transmission coefficients for 0^o and 30^o propagation across the equivalent of a quarter wavelength stiffener thickness (5 mm) were approximately 64% and 60% respectively. Then a stepped increase was predicted in the transmitted wave across the stiffener between 30^o and 48^o propagation directions. This could be due to a change of the apparent propagation distance inside the stiffener, which varies from 5.8 mm for 30^o to 7.5 mm for 45^o. Depending on the stiffener width ratio relative to the wavelength, different magnitudes of the transmitted wave can be observed. Almost 100% transmission has been observed at 49^o wave incidence (Fig 7.5), which might be attributed to secondary wave reflections inside the stiffener. The significant increase in the transmitted wave at 45^o can be also attributed to the acoustic impedance at this direction across the stiffener. The transferred energy to other forms (mode conversion) is expected to be less when there is a significant drop in the acoustic impedance. The range of incident angles that can be obtained in the modelling of parallel lines of monitoring nodes (Fig 7.5) was limited by the plate geometry. A wider range of the incident angles was obtained by extending the plate dimensions and the number of the monitoring nodes along the stiffener. However, elongating the lines of the monitoring nodes ahead of and behind the stiffener without maintaining sufficient time separation for the reflected pulses can bring about local interference at some monitoring locations. The calculation of the arrival time for the possible reflected waves from the stiffener and plate edges will be discussed in more depth in the next chapter (Chapter 8).

The verification was carried out to prove that the predicted wave spreading matches the assumed $1/\sqrt{r}$ curve of GUW radial spreading in plate structure. The amplitude of the first parallel monitoring line in front of the stiffener has been calculated using the maximum of the Hilbert transform of the time trace signal at each monitoring node on the line. The first line of the monitoring nodes has been modelled at different distances from the excitation point ahead of the stiffener to investigate the effect of varying the propagation distance on the radial spreading along the plate. Similarly, the second line of the monitoring nodes behind the stiffener has been modelled at different distances from the excitation point to study the effect of varying the propagation distance on the transmitted waves.

Table 7.2 Numerical uncertainty in the FE simulation relative to geometrical spreading curve ($1/\sqrt{r}$)

distance from excitation to the 1st monitoring line	Incident Angle			
	0°	15°	30°	45°
(% error) at 50 mm	2.6	2.5	1.5	0.9
(% error) at 100 mm	0.4	0.1	1.2	1.9
(% error) at 150 mm	0.1	0.5	0.9	0.8
(% error) at 200 mm	1.3	1.1	0.3	0.1
(% error) at 250 mm	1.4	1.3	0.4	0.3
(% error) at 300 mm	1.4	1.2	0.1	0.9

The wave amplitude was found to match the radial spreading curve $1/\sqrt{r}$, ahead of the stiffener, with acceptable variations that appear to be due to numerical effects in the FE simulation. The obtained amplitude from the first monitoring line has been used to investigate the best propagation distance, which should give limited numerical dispersion in the wave amplitude in front of the stiffener location. The first monitoring line ahead of the stiffener has been modelled at several propagation distances from the excitation location, 50 mm, 100 mm, 150 mm, 200 mm, 250 mm and 300 mm. The numerical effect on the simulated models has been investigated for different incident angles (0^o, 15^o, 30^o and 45^o). The uncertainty in the numerical calculation in each model has been calculated relative to the obtained wave amplitude from the radial spreading relation. The variation in the predicted wave scattering was compatible with the calculated error (Table 7.2), which was found based on the best match between the numerical prediction and the theoretical radial spreading of the guided waves.

The comparison (Table 7.2) shows that the obtained error from all numerical predictions of the excited and monitored waves, ahead of the stiffener, was less than 3% relative to the radial spreading curve $1/\sqrt{r}$. The incident wave was predicted in the

range of 0^o – 45^o across the stiffener in each monitoring model. The incident wave that has been monitored at 150 mm from the excitation point (1^{st} monitoring line) has shown a maximum of 1% uncertainty in the numerical prediction relative to the geometrical spreading curve. Therefore, 150 mm was the suggested distance between the excitation point and the 1^{st} monitoring line ahead of the stiffener for the employed plate model in the next chapter (Chapter 8). For a small plate size with 1 m stiffener length, the measured waves at 100 mm from the excitation point (1^{st} monitoring line) were matching the numerical prediction with reasonable error.

On the other hand, the influence of the monitoring location past the stiffener on the dispersion of the numerical calculation has been investigated as well. The stiffener size has been changed to eliminate the possible interference source (secondary reflections due to wave travelling up and down inside the stiffener) that can complicate the signal processing. A higher stiffener was modelled (Fig 7.6) to study the influence of varying the location of the monitoring line behind the stiffener on the transmission coefficient of the propagated wave across the stiffener. The predicted wave transmission at several perpendicular distances (50 mm, 100 mm, 150 mm and 200 mm) between the stiffener and the 2^{nd} monitoring line, behind the stiffener, has been compared.

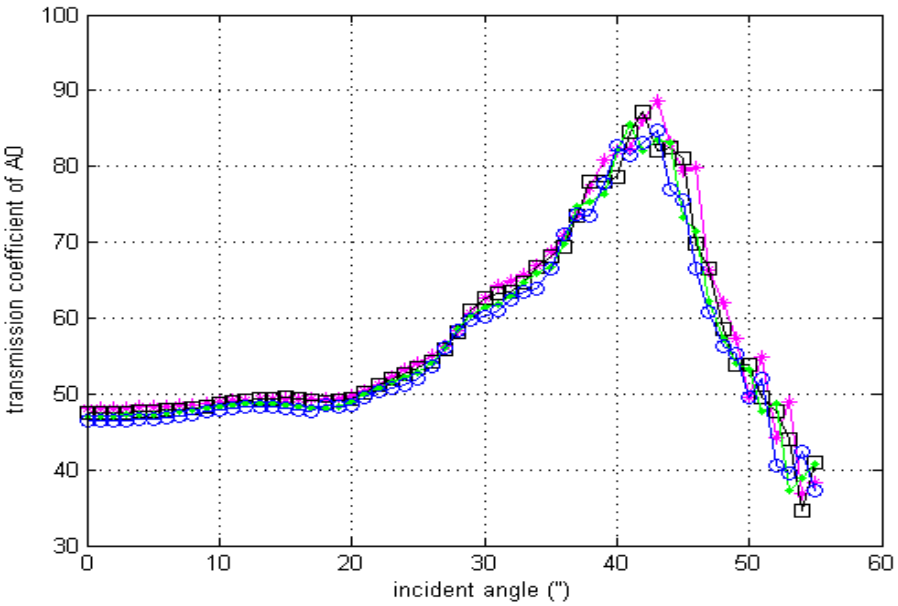

Fig 7.6 Transmission coefficient at a range of incident angles across stiffener of 80 mm height and 5 mm thickness for several monitoring locations, 50 mm, 100 mm, 150 mm and 200 mm from stiffener.

Table 7.3 Numerical uncertainty in the transmission coefficients relative to geometrical spreading curve ($1/\sqrt{r}$)

Distance from stiffener to the 2nd monitoring line behind stiffener	Incident Angle			
	0°	**15°**	**30°**	**45°**
50 mm, uncertainty %	0.7	0.03	0.36	1.8
100 mm, uncertainty %	0.56	0.12	0.48	0.67
150 mm, uncertainty %	1.4	1.7	2.4	9.4
200 mm, uncertainty %	2.8	2.4	4.3	6.5

A different angular dependency was observed for different stiffener dimensions as compared to Fig 7.5 (stiffener of 10 mm height), and this will be investigated further in chapter 8. In general, it can be concluded that the wave transmission, in all directions across the stiffener decreases with increasing stiffener size. The error in the predicted wave transmission at several distances behind the stiffener (50 mm, 100 mm, 150 mm and 200 mm) was calculated. The maximum difference in the wave amplitude relative to the fit curve ($1/\sqrt{r}$) was used to calculate the uncertainty in the predicted wave propagation. The wave transmission at different propagation directions across the stiffener (0^o, 15^o, 30^o and 45^o) was used to obtain the transmission field that has the lowest numerical uncertainty (Table 7.3). Wave monitoring at 100 mm behind the stiffener was found to introduce the lowest error of less than 1% compared with the other monitoring locations, and has been suggested for studying the transmitted wave in the next stage. The highest uncertainty in the predicted wave transmission was obtained at 45^o wave propagation across the stiffener (Table 7.3), possibly due to the amplitude fluctuations observed in Fig 7.3.

7.5 Energy Balance

As discussed in Chapter 2, several scattered wave modes are expected to appear in the plate as a result of the mode conversion at a stiffener. In addition to the excited wave mode (A_0), the other expected modes are the symmetrical wave mode (S_0), and potentially shear horizontal mode (SH_0), trapped modes along the stiffener and

nonpropagating wave modes appearing as local vibration at the stiffener location. Since the experimental work of this research was mainly concerned with the excitation and measurement of the out-of-plane A_0 mode using a laser interferometer, observing the in-plane wave mode (S_0) was not expected experimentally with the used monitoring method. In principle, scattering of the shear horizontal mode (SH_0) due to mode conversion is expected from wave propagation across a stiffener at oblique incident angle. At perpendicular propagation across the stiffener, the Lamb wave modes A_0 and S_0 were the only expected scattered wave modes due to mode conversion. The perpendicular scattering of the fundamental modes A_0, S_0 and SH_0 were simulated for A_0 mode excitation in the middle of the plate thickness to separate the modes. The pure A_0, S_0 and SH_0 wave mode scattering from the stiffener was predicted to validate the theoretical assumption. The amplitude of the scattered wave modes at the stiffener (S_0 and A_0) was used to calculate the transmitted and reflected waves at the stiffener. The employed procedure for quantifying the predicted transmission and reflection coefficients was validated by calculating the energy balance. For simplification, the energy balance has been calculated only at normal wave propagation across stiffener. For further verification, the energy balance investigation should expand to study the S_0 and SH_0 wave mode scattering in oblique directions.

The energy balance has been verified using the coefficients of the incident, transmitted and reflected waves at a stiffener, and then using the carried energy by the scattered modes at the stiffener. Summation of the displacement and stress field across the plate thickness gives the average power flow [73]. The carried energy by each mode was calculated using the power flow value that obtained from Disperse. The through thickness A_0 and S_0 power flow was used to obtain the normalized modes (U_{A_0} and U_{S_0}), and to correlate how much energy was actually carried by each mode. Relating the energy carried by the normalized mode U_{A_0} to the energy carried by U_{S_0} was performed to obtain the energy constant as suggested in previous research [74]. Then the energy carried by each mode was used to check the balance between the incident energy at the stiffener and the sum of the transmitted and the reflected energies, where T_{S_0} and R_{S_0} are respectively the predicted transmitted and reflected wave amplitude of the S_0 wave

mode. The transmitted (T_{A_0}) and the reflected (R_{A_0}) wave amplitude relative to the incident wave amplitude (I_{A_0}) were calculated at the stiffener location using the maximum of the signal envelope and $1/\sqrt{r}$ radial spreading correction. The relation between the incident, transmitted and reflected energy at the stiffener (Eq 7.2) can be applied to check the energy balance as long as there is no leakage in the energy of the propagated wave.

$$\left(\frac{I_{A_0}}{U_{A_0}}\right)^2 = \left(\frac{T_{S_0}}{U_{S_0}}\right)^2 + \left(\frac{T_{A_0}}{U_{A_0}}\right)^2 + \left(\frac{R_{S_0}}{U_{S_0}}\right)^2 + \left(\frac{R_{A_0}}{U_{A_0}}\right)^2 \quad \textbf{Eq 7.2}$$

The energy balance, Δ_E, was investigated using the second approach based on the transmitted (TC_{A_0}) and reflected (RC_{A_0}) coefficients relative to the incident wave mode, $A_{0,}$ at normal propagation across the stiffener (Eq 7.3 & 7.4).

$$TC_{A_0} = \frac{T_{A_0}}{I_{A_0}} \quad \textbf{Eq 7.3}$$

$$RC_{A_0} = \frac{R_{A_0}}{I_{A_0}} \quad \textbf{Eq 7.4}$$

The wave amplitude that has been used in the calculation of the transmission and reflection coefficients was normalized to the maximum wave displacement at the excitation location. The accuracy of the calculated coefficients, TC_{A_0} and RC_{A_0}, was proved by obtaining Δ_E value close to 100% (Eq 7.5).

$$\Delta_E = \left(\frac{U_{A_0}}{U_{S_0}} * TC_{S_0}\right)^2 + \left(TC_{A_0}\right)^2 + \left(\frac{U_{A_0}}{U_{S_0}} * RC_{S_0}\right)^2 + \left(RC_{A_0}\right)^2 \approx 1 \quad \textbf{Eq 7.5}$$

where TC_{S_0} and RC_{S_0} are respectively the transmitted and reflected coefficients of the normal scattering of the S_0 wave mode at the stiffener (Eq 7.6 & 7.7).

$$TC_{S_0} = \frac{T_{S_0}}{I_{A_0}} \quad \textbf{Eq 7.6}$$

$$RC_{S_0} = \frac{R_{S_0}}{I_{A_0}} \quad \textbf{Eq 7.7}$$

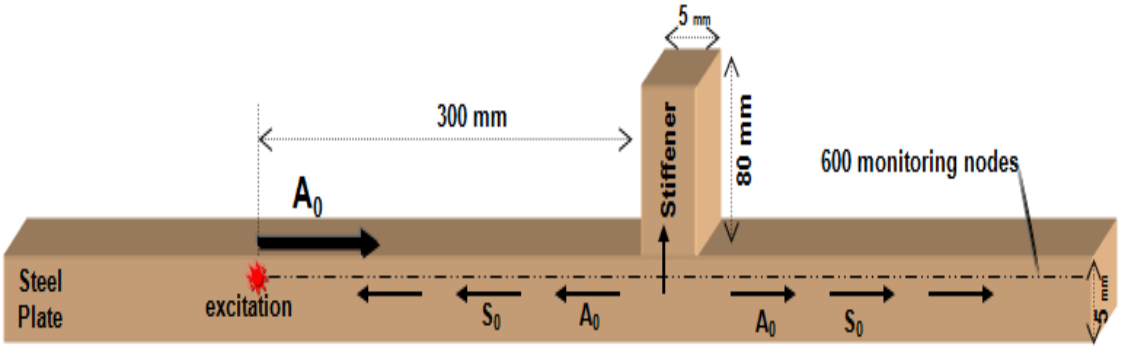

Fig 7.7 Schematic of the incident and scattered wave modes at stiffener simulated along the width of steel plate (1.5 m x 1 m x 5 mm).

Energy balance verification was carried out using a FE plate model (1.5 m x 1 m x 5 mm) that simulates an excitation frequency of 100 kHz for the A_0 Lamb wave mode excitation and propagation along the plate. The excitation location was chosen in the middle of the plate thickness at 300 mm from the simulated stiffener, which is 80 mm high and 5 mm thick. The wave amplitude was monitored along a perpendicular line, of 600 nodes, across the stiffener (Fig 7.7). The pattern of the perpendicular propagation of the flexural Lamb wave and normal scattering at the stiffener including mode conversion were predicted numerically. The sum of the transmitted and the reflected energies was compared with the energy of the incident wave at the stiffener (Eq 7.2). The second check of the energy balance was performed using Eq 7.5. The outcome of the transmission and reflection coefficients has fulfilled the required condition for the energy balance in good approximation (Table 7.4).

Table 7.4 Transmission and reflection coefficients of A_0 and S_0 wave mode from stiffener (size: 80 mm height and 5 mm thickness) at 100 kHz.

TC_{A_0}	RC_{A_0}	TC_{S_0}	RC_{S_0}	Δ_E
0.84	0.53	0.15	0.17	0.98

The above table shows clearly the factor of the converted energy from the A_0 wave mode to the S_0 mode for normal wave transmission across the stiffener. The computation of the energy balance using the coefficients of the incident, transmitted and reflected waves from the stiffener including mode conversion gives a number Δ_E very close to 1 with 2% error. This error can be attributed to the fact that the propagated waves were monitored in the local interference zone at the stiffener. Thus, the probability of obtaining error due to coincidence in the arrival time of the scattered pulses from the stiffener is more than zero. In general, the prediction of Lamb wave transmission and reflection in the normal direction across a high stiffener was examined using the energy balance method and found to be accurate. The energy balance check can also be used to investigate the accuracy of the transmitted and reflected wave in other directions, e.g., 15^o, 30^o and 45^o, across the stiffener. The energy of the transmitted and reflected A_0 wave mode at the stiffener (addition of the squared amplitudes), which was calculated normalized to the incident wave mode (Eq 7.5), was considered a good indicator for investigating the energy carried by the A_0 mode. Without specifically modelling the scattered S_0 and SH_0 modes, the energy carried by the scattered A_0 wave mode gives a good indication of the amount of mode conversion occurring. For the employed wave propagation models in this chapter, the transmitted and reflected energy from the stiffener was mostly carried by the A_0 wave mode, limited mode conversion.

Fig 7.8 Stiffener of L-shaped cross-section (50 mm x 50 mm, 5 mm thick) welded on steel plate (size: 2 m x 1 m, 5 mm thickness).

7.6 Experimental Verification

The A_0 wave mode propagation behaviour across a stiffener was predicted using FE simulations. Different excitation and monitoring configurations were simulated to validate the predicted behaviour. Further validation was performed using laser interferometer measurements across the stiffener with an L-shaped cross-section (size: 50 x 50 mm, 5 mm thick). The L-shaped stiffener is one of the two model geometries that would typically be used for ship hulls. A typical ship hull plate would be of 10 mm to 20 mm thickness, and the welded stiffener would have the same thickness as the plate and 100 mm to 200 mm length on each side of the L-shape. The relative employed plate and stiffener geometries in the experimental verification match the welded stiffener in the ship hull. In principle, the used L-shaped stiffener has a realistic geometry relative to the plate thickness (Fig 7.8), and the guided wave propagation model can be scaled with the frequency thickness product. The propagation and scattering of the A_0 Lamb wave mode in a steel plate, 2 m × 1 m and 5 mm thickness, has been investigated at 100 kHz, 150 kHz and 200 kHz excitation frequency. The propagating waves were measured at several locations in front of and past the stiffener, and all measurements have been performed at room temperature. At the first stage of the measurements, lines of monitoring points across the stiffener were measured at two directions (0^o and 45^o) to calculate the transmission and reflection coefficients. Data signals from the monitoring line across the stiffener at 0^o were fitted with the radial spreading curve, $1/\sqrt{r}$, as shown for both the FE model and experimental evaluation (Fig 7.9).

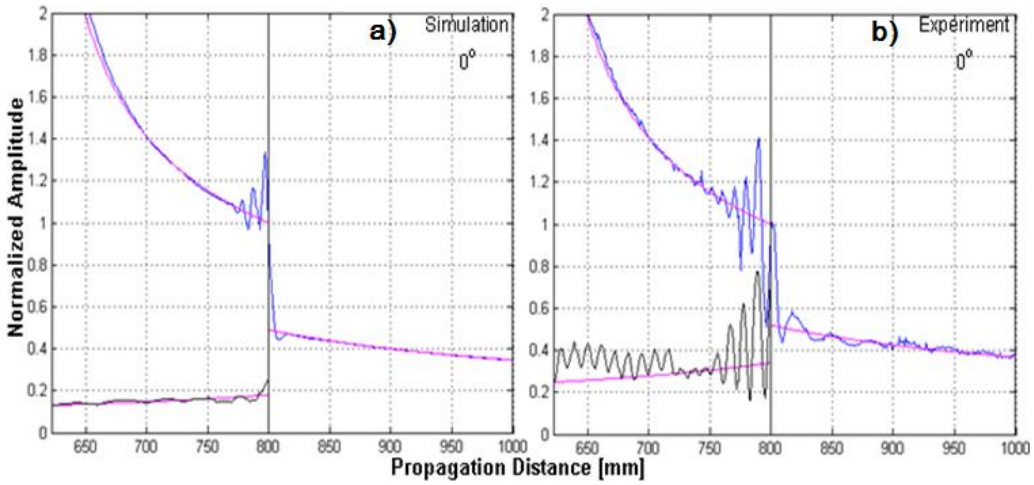

Fig 7.9 Simulated (a) and measured (b) A_0 wave mode transmission and reflection across L-shaped stiffener at 0^o incident angle (steel plate 5 mm thickness; frequency 100 kHz).

The slight shift of the incident wave amplitude from the wave spreading curve at 150 mm distance from the stiffener (Fig 7.9a) has been attributed to the remaining dispersion behaviour of the propagating wave mode at the used *fd* product in the model. The amplitude of the incident, transmitted and reflected wave at 0^o propagation direction in the experimental approach has shown reasonable match with the predicted transmission and reflection behaviour. A reduction of 48% and 52% was observed in the amplitude of the transmitted wave across the stiffener relative to the incident wave in the analysis of the numerical and experimental approaches respectively. The amplitude of the reflected wave in the experimental measurement has shown interference with other reflections (Fig 7.9b). The measured signals were repeated and the analysing process has been examined to reduce the error source in the signal amplitude. Nonetheless, it has been found that the measured reflection coefficients cannot be trusted, because the reflection behaviour does not show the expected match with the radial spreading $1/\sqrt{r}$. The predicted wave scattering at 45^o propagation across the stiffener was validated using experimental measurements across the L-shaped stiffener. A comparison was performed between the outcomes of the FE simulation and the measurements (Fig 7.10).

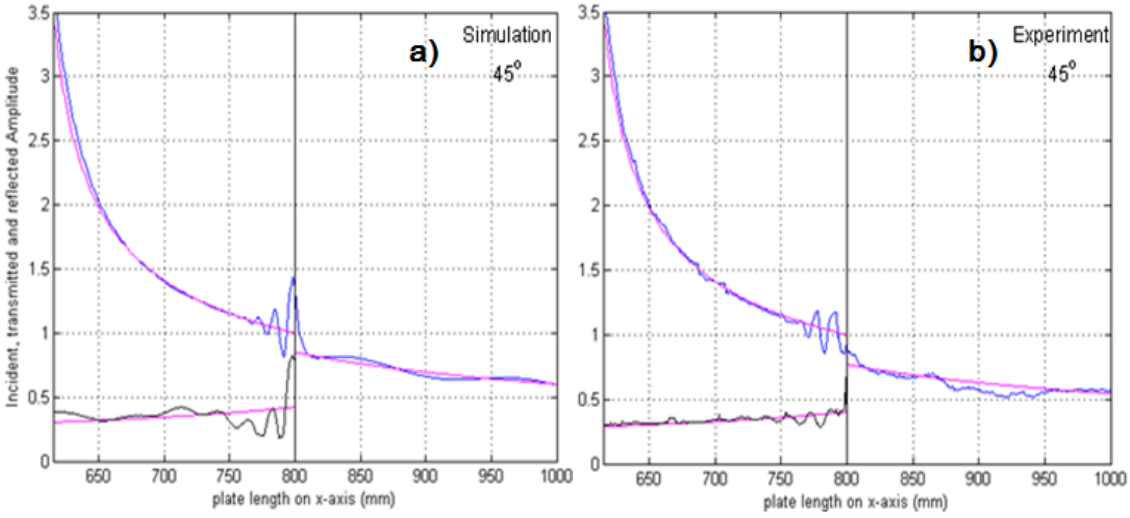

Fig 7.10 Simulated (a) and measured (b) A_0 wave mode transmission and reflection across L-shaped stiffener at 45^o incident angle (steel plate 5 mm thickness; frequency 100 kHz).

The propagating wave at 45^o has shown a slight reduction in the amplitude of the transmitted wave across the stiffener relative to the incident wave. The predicted amplitude for the transmitted wave across the stiffener has shown reasonable match with the radial spreading curve (Fig 7.10a). Different transmission coefficients were observed in the comparison between the measured and predicted wave amplitude (Fig 7.10), respectively 56% and 68%. On the other hand, the predicted wave reflection from the stiffener has shown limited constructive and destructive interference below the fitted curve of the radial spreading (Fig7.10a). In general, a reasonable agreement has been obtained for the comparison between the measured and predicted wave scattering at 45^o propagation direction across a stiffener thickness of 5 mm ($\frac{1}{4}\lambda$). However, a large reduction in the transmitted wave is expected across larger size stiffeners due to the wave traveling inside the stiffener. The comparison between the normal and oblique scattering at the stiffener, Fig 7.9 and Fig 7.10 has shown a very clear dependency of the transmitted wave amplitude across the stiffener on the propagation direction.

The transmitted and reflected waves have been obtained experimentally using the normal (Fig 7.9) and oblique (Fig 7.10) laser measurements across the stiffener. In the second approach, the transmission and reflection coefficients were calculated for a wide range of directions using two parallel lines of measurements, ahead of and behind the stiffener. The parallel lines of measurements have been suggested to replace measurements across the stiffener in each direction. Reasonable agreement was achieved from the comparison between scattering coefficients in the range of 0^o - 45^o from monitoring lines across the stiffener and parallel to the stiffener. The parallel lines of measurements were suggested at 230 mm ahead of the stiffener and 100 mm past the stiffener (Fig 7.11).

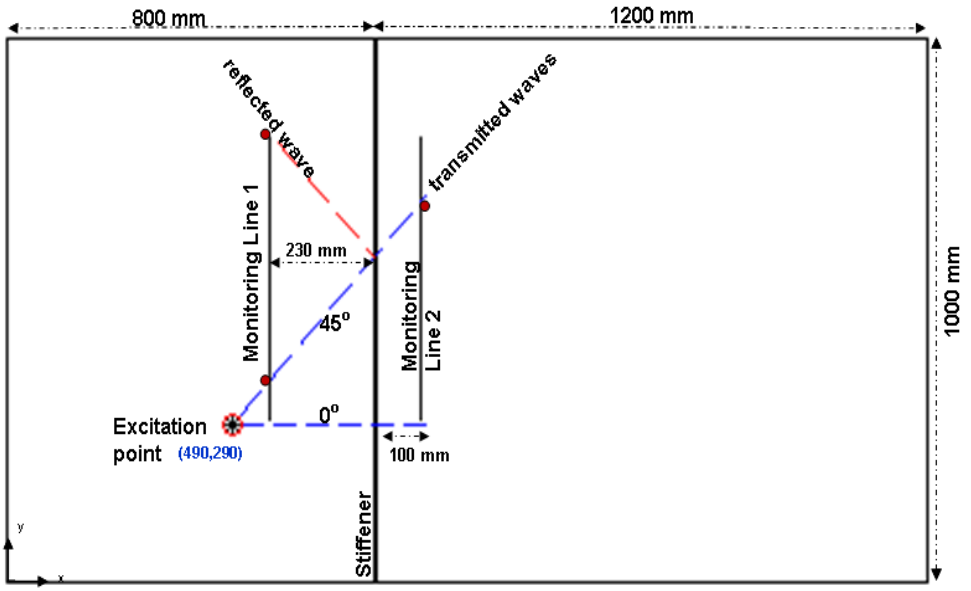

Fig 7.11 Monitoring of A_0 wave mode propagation in front of and past stiffener in a range of 0^o - 45^o

The monitoring zones were arranged parallel to the stiffener to reduce the experimental and numerical work, which was required for obtaining the transmission and reflection coefficients in a range of propagation directions. The suggested locations for the parallel lines allow for sufficient time separation between the transmitted and reflected pulses in a range of incident angles from 0^o - 45^o. Four hundred measurements with 1 mm step size in the y-direction have been performed to obtain each of the parallel lines. Signal analysis has been carried out using Matlab to calculate the travel distance of the propagated waves across the stiffener based on known information about the incident wave direction and the monitoring location. The arrival time at each monitoring node was calculated using the travel distance and the group velocity. The maximum of the signal envelope was obtained. The amplitude of three predicted and measured signals, on the parallel lines (Fig 7.11), was obtained for each propagation direction, and then corrected at stiffener location using the relation of the radial spreading (Eq 7.1). The ratio of the transmitted and reflected waves relative to the incident wave was quantified for a range of angles 0^o - 45^o with an increment of one degree. A comparison with FE simulation results was performed between the analysis of the predicted and measured time trace signals at 100 kHz and 150 kHz (Fig 7.12).

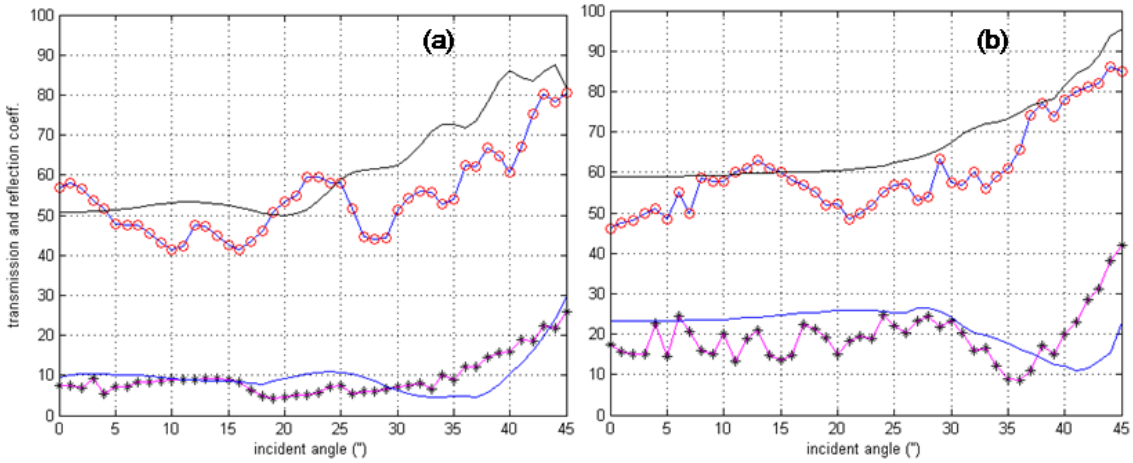

Fig 7.12 Experimental A_0 wave mode transmission (circles) and reflection (stars) coefficients compared to FE prediction of the transmission (black line) and reflection (blue line) coefficients at 100 kHz (a) and 150 kHz (b) across L-shaped stiffener.

The same signal processing steps were repeated for both the measured and simulated signals. In general, the transmission and reflection patterns from the simulated model were reasonably matching the experimental results (Fig 7.12a). The transmission coefficient at 100 kHz was varying between 40 – 80%, and a more or less systematic increase was observed with increasing propagation direction above 30^o. Based on the previous energy balance calculations for normal transmission across the stiffener (Table 7.4), 50% of the incident A_0 wave mode was transmitted, 10% was reflected, and the remaining energy (40%) has been mode converted or trapped at the stiffener (Fig 7.12a). It can be concluded that mode conversion across the stiffener decreases with increasing transmission angle up to 45^o, and less energy is expected to be carried by the S_0 wave mode above 30^o wave propagation angle. The SH_0 wave mode is expected to appear in the scattered guided wave field at oblique wave propagation across the stiffener. The balance between the incident energy at the stiffener and the energy carried by the transmitted and reflected modes is important to explain how increasing patterns can be observed simultaneously for the transmitted and reflected A_0 wave mode with increasing propagation angle (Fig 7.12a). The reflected wave at 100 kHz has shown almost constant behaviour with varying propagation direction up to 25^o, and then a considerable increase in the reflection coefficients was recorded above 35^o. On the other hand, limited wave reflection was obtained from 100 kHz propagation at small incident angles compared to the wave reflection at 150 kHz (Fig 7.12b).

The obtained reflection coefficient at 150 kHz was 20% of the incident wave amplitude at incident angles below 25°, which is approximately twice the observed reflection coefficient at 100 kHz. In contrast, the transmitted waves at 150 kHz have shown a variation pattern almost similar to that observed at 100 kHz (Fig 7.12) with a slight increase at high incident angles. A significant reduction in the reflected wave from the stiffener at 150 kHz was observed above 30° propagation direction (Fig 7.12b). Then above 40° incident angle the reflection pattern of the 150 kHz wave propagation has shown a clear increase up to 45°. The validation at 150 kHz using the numerical and experimental approaches has shown better agreement compared to the validation at 100 kHz. A significant reduction is expected in the S_0 wave mode conversion at 150 kHz and 45° to balance the observed increase of both the reflected and transmitted A_0 mode at the same direction. Wave scattering at 200 kHz was predicted and validated experimentally using the same evaluation approach that has been used for 100 kHz and 150 kHz. Almost constant transmission and reflection was predicted with increasing propagation direction up to 30° and 25° respectively (Fig 7.13). Then the scattering behaviour at higher angles was found to almost match the predicted behaviour at 150 kHz.

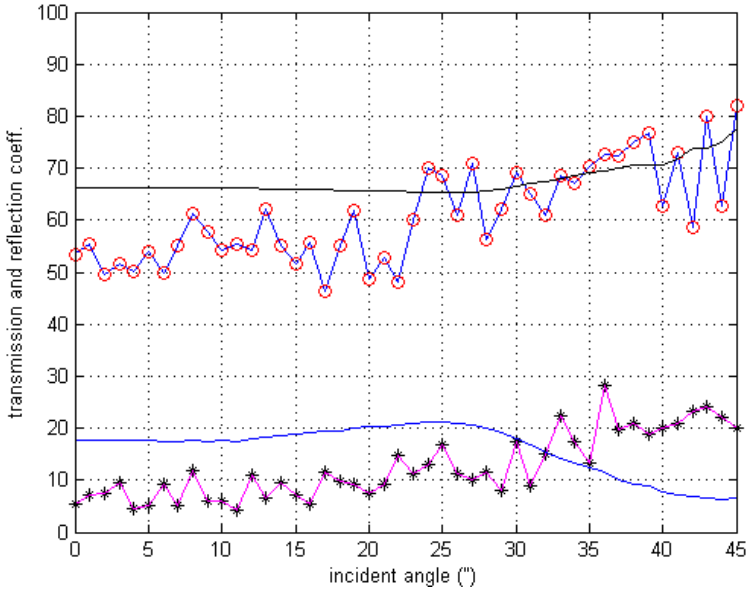

Fig 7.13 Experimental A_0 wave mode transmission (circles) and reflection (stars) coefficients compared to FE prediction of the transmission (black line) and reflection (blue line) coefficients at 200 kHz across L-shaped stiffener.

The obtained transmission coefficients using the experimental measurements at 200 kHz have shown only limited agreement with the pattern of the predicted coefficients for the range of propagation angles (Fig 7.13). In fact, the used plate in the experimental measurements contains a reasonably uniform weld along the stiffener (Fig 7.8), and it has been decided in the numerical approach to neither model the weld butt nor the material changes due to the welding process. The used transducer was functioning very well and good measurements were obtained at 100 kHz and 150 kHz excitation frequency. Reasonably good incident and transmitted signals (5 cycles) across the stiffener were observed in the measurements of 200 kHz. Nevertheless, the quality of the experimental results at 200 kHz was not as good as it was at 100 kHz and 150 kHz. Disagreement was observed in the reflection coefficients between the predicted and measured results for 200 kHz, especially above 30^{o} propagation angle (Fig 7.13). The mismatch between the measured and predicted scattering at 200 kHz can be attributed to the quality of the measured signals, since sudden changes have been observed in the relative amplitude with varying propagation direction. An increase of 5% was observed in the predicted transmission with increasing excitation frequency from 100 kHz to 150 kHz at propagation angles below 20^{o}. In comparison, changing the excitation frequency from 100 kHz to 200 kHz has shown a 10% increase at the same propagation directions. Then a considerable increase in the transmitted wave was predicted for increasing propagation angle, but with different patterns for different excitation frequency.

The dependency of the wave propagation on the excitation parameters was investigated numerically and validated experimentally. However, to investigate experimentally the dependency of the transmitted wave on the stiffener geometry, a large number of welded stiffeners at different geometries would be required. Therefore, this research was focusing on the numerical approach only to understand the influence of varying stiffener size on the scattering behaviour.

7.7 Limitations of the Model Geometry

The expected reduction in the wave amplitude across a stiffener is thought to be governed by the wave geometrical spreading and stiffener size only. However, the obtained results (Table 7.2 and Table 7.3) have shown that numerical errors can affect the simulated wave along the plate. Therefore, excitation and monitoring arrangement has been adjusted to reduce this error. Plate size, stiffener location, distance from excitation point to the stiffener and to the monitoring nodes were found to be affecting the investigated wave along the plate. Covering a wide range of incident angles at reasonable numerical error in the simulated model will limit the scope of this research. Moreover, the computer that has been used for this research (Linux, 16 GB RAM) limit the potential size of FE models. Above eight million elements the required computer running time to finish one explicit Abaqus simulation model because prohibitive due to the memory restrictions for the employed PC. Therefore, the summation of the plate and stiffener elements in the simulation model should not exceed the maximum number of elements available on the used PC. Model stability was maintained in the 5 mm plate and stiffener thickness using 8-node block elements of $\Delta x = \Delta y = 1$ mm, and $\Delta t = 1x10^{-7} s$. The required even number of elements in the plate through thickness was obtained using $\Delta z = 1.25$ mm. A stiffener model of 80 mm height along a plate of 1.5 m length and 1.1 m width has been suggested since the total number of elements (7 million) does not exceed the maximum permissible number. The number of the used element in the FE simulation could be increased using larger computer storage memory.

The plate model (without any absorbing material) includes enough elements of the same plate material around the area of interest to provide time separation between the incident and the reflected pulse. Adding absorbing material around the region of interest in the simulated plate model has been suggested recently by several research groups [75, 76]. The method to enhance computational efficiency by meshing the area of interest only has been examined. Boundary conditions that allow absorbing all the arrival waves at the external region of the model rather than reflect it back to the area surrounding the defect has been discussed [75]. Two models have been used, Perfectly Matched Layers (PML) and Absorbing Layers using Increasing Damping (ALID). The medium of the absorbing material has the same elastic properties and mass density as

the investigated region. It has been proved utilizing the FE simulation that adding perfect matched layers of the absorbing materials allows no energy flow in the added medium [76].

However, zero reflection from the absorbing layers cannot be attained. In fact, adding perfect matched layers of absorbing material was investigated for several reasons. Adding absorbing material was found to be essential to avoid generating standing wave modes. Furthermore, it allows proper representation for the leakage of the propagated wave at the plate edges. However, using the modified model that includes non-reflecting boundary layers would require generating a large number of elements in the absorbing area, which would often lead to large models. The number of the absorbing elements that need to replace the normal plate elements, which give proper time separation, is also considered very large as many as the number of the replaced plate elements. What is more, the additional features in the absorbing elements would require longer computational time to solve additional unknown variables. In conclusion, the previous research has proven that using non-reflecting boundary layers elements will show no change in the required number of elements for model stability. A reduction in the plate size is possible, but still large requirement, so overall memory reduction is limited.

7.8 Summary

The wave propagation, transmission and reflection at a stiffener have been investigated over a range of incident angles. Different stiffener cross-sections, e.g., rectangular and L-shaped, were modelled and the A_0 Lamb wave mode scattering behaviour at stiffeners was predicted for different excitation frequencies. The predicted time trace signals along normal and oblique lines across the stiffener have been used to calculate the transmission coefficients at four directions, 0^o, 15^o, 30^o and 45^o as the first monitoring step. Using an alternative monitoring approach, time trace signals were predicted along two parallel lines ahead of and behind the stiffener. The second monitoring regime was used to calculate the transmission and reflection coefficients up to 45^o propagation direction from a single FE simulation. The applied processing steps

have been validated using different monitoring regimes. The energy balance was calculated to validate the prediction of the transmitted and reflected wave. A PZT transducer was used to excite the A_0 Lamb wave mode at low frequency in a large steel plate with a welded L-shaped stiffener across the plate width. The predicted wave transmission and reflection from the stiffener at different incident angles were validated employing experimental measurements. The coefficient of the transmitted wave across the stiffener has a high dependency on the propagation direction, especially at high incident angle. Variation of the excitation frequency has shown a slight change in the behaviour of the transmitted and reflected waves from the stiffener. Further FE simulations are presented in the next chapter to understand the influence of varying stiffener height and thickness on the transmitted and reflected waves.

Chapter 8

Variation of Stiffener Size and Excitation Frequency

In the previous chapter the radial spreading of the GUW for normal and oblique transmission across a stiffener has been verified, allowing the efficient investigation of the influence of varying stiffener dimensions and the excitation frequency on the A_0 Lamb wave mode scattering. Calculation of the transmission and reflection of the guided wave at the stiffener for a wide range of directions has been achieved using parallel lines of monitoring nodes in front of and past the stiffener. The limitations of the monitoring zone, stiffener location and excitation location have been investigated to select the best simulation model for a systematic study. This chapter will investigate the excitation frequency and the monitoring direction that can generate sufficient transmitted energy for damage detection behind a stiffener welded to a steel plate.

8.1 Time Separation for Local Interference at Stiffener

The main objective in this chapter is to obtain sufficient time separation for the pulse of interest in the incident, transmitted and reflected waves at the stiffener to separate it from the remaining pulses in the received time trace signals. From the beginning it has been decided to use a large plate size to avoid unwanted pulses overlapping, which usually occurs due to wave reflections from plate edges. Predicting the wave transmission across a stiffener in a range of 0^o- 60^o and the wave reflection in a range of 0^o- 45^o was achieved using plate models of size 1.5 m by 1.1 m. The initial calculation of the reflected wave has shown that a minimum of 300 mm distance needs to be maintained between the monitoring nodes and the plate side in each direction. A wider range of incident angles can be obtained by increasing the length of the monitoring lines along the stiffener. However, elongating the lines of the monitoring nodes ahead of and behind the stiffener without maintaining sufficient time separation for the

reflected pulses can produce local interference at the additional monitoring nodes. The initial calculation of the arrival time for the plate edge reflections was found to overlap in time with the direct pulse from the excitation point. To solve this problem, monitoring locations should be modelled far enough from the plate edge to avoid an overlap of unwanted pulses (edge reflection) in the received train of pulses. The required distance between the monitoring nodes and the plate sides can be calculated based on the fact that the angles of the incident and reflected waves are equal. The required calculations for the arrival times of the incident and the reflected pulses in the time trace signal can be performed using the following example for the monitoring setup geometry (Fig 8.1). The excitation location was modelled at (400 mm, 300 mm), with the farthest monitoring point at (500 mm, 600 mm), 100 kHz excitation frequency, 5 cycles pulse width (*PW*), and $50\mu s$ pulse length in the time domain. The tangent of the incident and reflected angle (ϕ) has been used to calculate the opposite sides of the right triangles, 422 mm and 527 mm, relative to their corresponded adjacent sides of 400 mm and 500 mm respectively (Fig 8.1). The perpendicular distance between the excitation and reflection point on the plate side has been calculated (*side*). The travel distance of the reflected wave from the plate side at reflection angle ϕ can be calculated using the hypotenuses of the opposite right triangles.

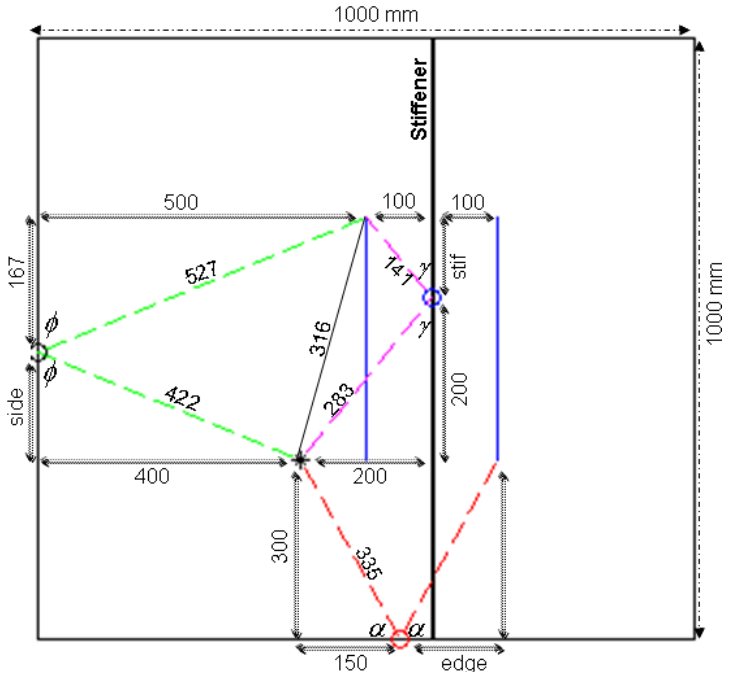

Fig 8.1 The anticipated reflected waves from the plate side (dashed green), bottom (dashed red) and from stiffener (dashed pink) in plate structure with calculated distances in mm.

The travel time of the reflected pulse from the plate side ($refl_{side}$) and the actual arrival time of the direct detected pulse (*AAT*) at the upper end of the 1st monitoring line can be calculated using the group velocity in steel (*2980 m/s*). In a further step, the computed time can be compared to satisfy the time separation between the direct and reflected pulses in the time trace signal (Eq 8.1)

$$AAT + PW < refl_{side} \quad \textbf{Eq 8.1}$$

The same calculation steps have to be performed again for the lower end of the 2nd monitoring line to ensure enough time separation between the direct pulse and the reflected wave from the bottom edge of the plate (Fig 8.1). To avoid having the direct pulse overlap with the stiffener reflection pulse in the time domain, sufficient separation distance has to be maintained between the stiffener and the monitoring line. The interference between the stiffener reflection and plate edge reflection has to be considered using the same method for the calculation of the coefficients of the reflected waves from the stiffener. Calculating the arrival time of the reflected pulses from the stiffener ($refl_{stif}$) and plate side, $refl_{side}$, this problem can be avoided (Eq 8.2).

$$refl_{stif} + PW < refl_{side} \quad \textbf{Eq 8.2}$$

For visualization, the suggested area for good wave excitation and receiving locations, without wave interference in the time domain, has been highlighted on the plate drawing (Fig 8.2). The process of calculating the wave interference in the time domain (Eq 8.1 & Eq 8.2) for a range of incident angles between 0^o – 45^o in the plate model (Fig 8.1) has been repeated for all considered plate geometries in this chapter. To obtain the transmission coefficient for a higher range of incident angles, 0^o – 60^o, the plate dimensions need to be changed.

Fig 8.2 Suggested area (green) for wave excitation and monitoring to avoid pulse overlap in the received time signal.

A plate model of 1.5 m height and 1.1 m width can satisfy the criterion of sufficient time separation between the direct incident wave pulse and the reflected pulses from the plate edges. The monitoring regime for the suggested plate geometry in this case shows 150 mm distance between the excitation point and the 1st monitoring line in front of the stiffener. The 2nd monitoring line behind the stiffener was modelled at 500 mm distance from the excitation point (Fig 8.3). The new plate geometry can provide wave separation between the incident and reflected pulses in a limited range of angles (0^o – 45^o).

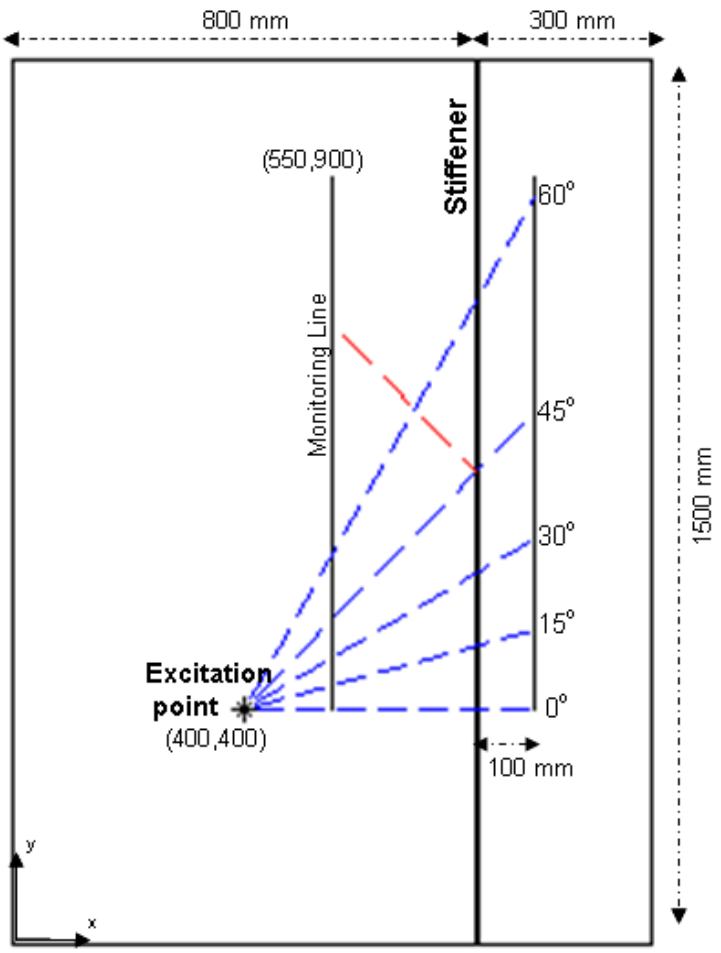

Fig 8.3 Schematic of steel plate showing transmitted A_0 Lamb wave mode across stiffener in normal and oblique directions (dashed blue) , reflection at 45^o (dashed red) and two parallel lines of monitoring nodes ahead of and behind the stiffener; plate size: 1500 mm x 1100 mm x 5 mm.

Another challenge in the signal processing was the interference with a secondary pulse that was scattered from the stiffener for certain stiffener heights due to internal reflections, which arrived with a small time delay after the transmitted and reflected waves at the monitoring locations. Reduction of the effect of the secondary pulses was not dependent on the pulse separation in the time domain described above. Therefore, a different attempt was used to solve the secondary pulse problem by increasing the time gating window additionally by half of the pulse-width, *PW*, to calculate wave amplitude of the time trace signal. The signal processing was slightly improved by this, especially at high incident angles.

8.2 Variation of Stiffener Thickness

The influence of varying stiffener thickness on the transmitted and reflected waves from the stiffener was investigated using FE simulations. A variation of the thickness from 1 – 25 mm with 1 mm step and then from 25 – 40 mm with 5 mm steps were considered. The stiffener thickness in the modelled plate structure was varied for different constant heights to study the influence on the wave behaviour by varying one stiffener dimension at a time. The ratio of the transmitted wave relative to the incident wave was initially predicted across a high stiffener (80 mm height), relative to the plate thickness of 5 mm. The simulation was carried out for a reasonably tall stiffener to reduce the influence of multiple reflections, due to the wave travelling up and down the stiffener, on the predicted wave field. The calculated scattering coefficients in this investigation are presented versus the modelled thicknesses, which were calculated as percentages of the wavelength of the A_0 mode. The wave scattering pattern was quantified at different stiffener thicknesses and several propagation directions (Fig 8.4) using 100 kHz excitation and 18.7 mm wavelength (λ). The reduction in the transmission ratio with increasing thickness of a relatively high stiffener was predicted (Fig 8.4a). This reduction is more or less linear for oblique wave transmission (45^o) across the stiffener. The normal wave transmission pattern (0^o) shows an initial sharp reduction for an increase of the stiffener thickness to 25% of the wavelength. For thicker stiffeners with an axial extent up to 2λ small variations of the transmission ratio, around 40% amplitude, were observed. Increasing the propagation angle from 45^o to 60^o and increasing the stiffener thickness up to a wavelength, a significant drop was observed in the transmitted wave across the high stiffener. An increase in the transmitted wave at 60^o was recorded at stiffener thickness from 70% to 130% of the wavelength (Fig 8.4a), with almost no transmission for stiffeners thicker than 130% of the wavelength.

In general, a significant increase was observed for the oblique reflection (45^o) of the A_0 wave mode with an increase of the stiffener thickness up to about the wavelength (λ) (Fig 8.4b). For a larger thickness ($>\lambda$) the scattered wave field at the stiffener has shown an almost constant reflection coefficient of about 90%.

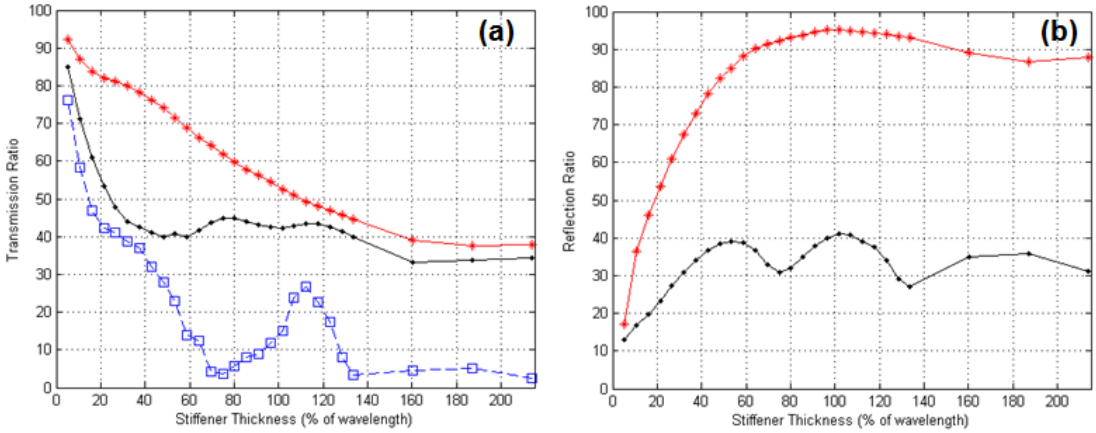

Fig 8.4 Ratio of the transmitted *(a)* and the reflected *(b)* waves from 80 mm stiffener height for several thicknesses at 0^o (dots, black), 45^o (stars, red) and 60^o (squares, blue) incident angle.

The normal reflection from a tall stiffener has shown an initial increase with stiffener thickness and then a systematic constructive and destructive interference with the variation of the stiffener thickness. A similar plate geometry with a thickness reduction instead of the additional thickness, which represents the stiffener height, has been studied by Demma et al [31], and the normal reflection has been predicted. The maximum interference in the normal reflection from the simulated notch was obtained at 50% and 100% of the wavelength, and a similar reflection pattern, but with smaller amplitude variations, was predicted from the scattered wave field for the tall stiffener (Fig 8.4b). This shows how the reflected wave from a thickness change in the plate is highly dependent on the length of the obstacle relative to the wavelength. The transmission and reflection coefficients (Fig 8.4) have shown a significant shift in the patterns between wave propagation in the normal direction and the oblique (45^o) direction across the stiffener. For further understanding of the influence of the propagation direction on the wave transmission and reflection behaviour, scattering for two more propagation directions, 15^o and 30^o, was investigated. The scattering behaviour, which was observed from the additionally investigated directions at several stiffener thicknesses (Fig 8.5), was found to be very close to what has been shown before for the normal (0^o) propagation direction.

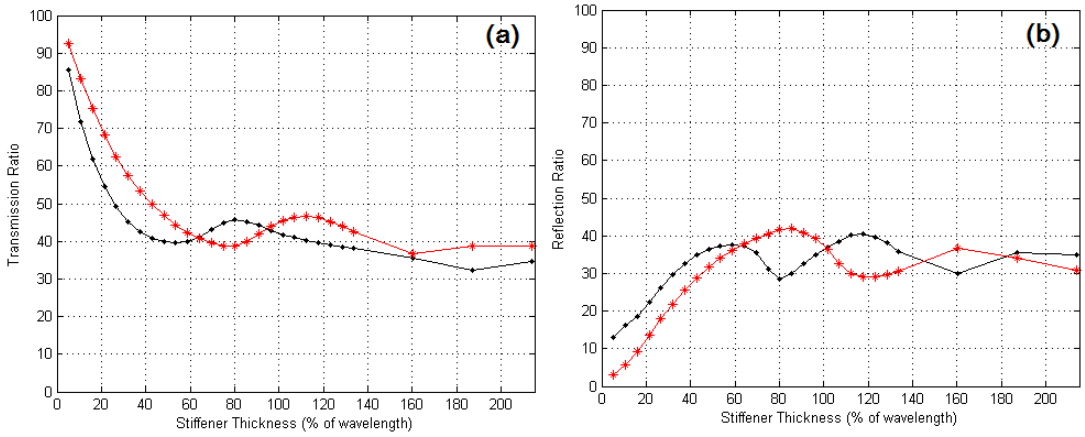

Fig 8.5 Ratio of the transmitted *(a)* and the reflected *(b)* waves from 80 mm stiffener height for several thicknesses at 15° (dots, black) and 30° (stars, red) incident angle.

The transmitted waves at 15° and 30° have shown significant decrease with varying the thickness up to 50 - 60% of the wave length, and then almost constant transmission pattern with a small effect of interference observed at the higher stiffener thickness (Fig 8.5a). Nonetheless, the minima and maxima of the 15° and 30° transmission patterns were obtained at different stiffener thicknesses. The constructive and destructive interference in the reflection pattern at 15° and 30° (Fig 8.5b) were achieved at the thickness that was showing respectively maximum and minimum interference in the transmission. Significant increase was observed with varying stiffener thickness up to 50% of the wave length, in an opposite behaviour to the transmission pattern. Limited change was observed in the scattered wave field at a tall stiffener of thickness more than 60% of the wavelength (Fig 8.4 & 8.5). Varying stiffener thickness has shown a potential increase for the energy carried by the S_0 mode to balance the predicted reduction in the A_0 mode (Fig 8.4a) at normal wave transmission across the stiffener. In the case of oblique wave propagation, up to 30° (Fig 8.5), the used energy to balance the A_0 mode reduction mostly depends on the scattered guided waves from mode conversion. At thick stiffener (>1.5λ) the transmission patterns above 45° (Fig 8.4a) have indicated that the total energy carried by the A_0 wave mode (addition of the squared amplitudes) is about 40% of the incident energy. A significant amount of mode conversion and other effects, e.g., local boundary layer at stiffener and secondary scattered pulses, appear to happen. However, obtaining the exact energy carried by the other modes requires further FE simulations.

Further signal analysis was carried out to quantify the scattered wave field at a high stiffener (80 mm) for a range of propagation directions. The modelled stiffener thickness was 15 mm, just below the wavelength (18.7 mm) and above 60% thickness for which limited change was observed (Fig 8.6). The calculated scattering coefficients at the specific angles 0^o, 15^o, 30^o and 45^o (Fig 8.4 & 8.5) are shown for comparison in Fig 8.6. Almost constant transmission and reflection coefficients were predicted for incident directions up to about 30^o. The transmission and reflection coefficients for 0^o and 30^o propagation across the equivalent of one wavelength stiffener thickness were approximately 40% and 35% respectively. Then significant variation was observed with increasing propagation angle, e.g., a drop of the transmission coefficient and an increase in the reflection coefficient above an angle of 45^o. The same calculation method can be applied to all modelled stiffeners to obtain more details about the propagation behaviour in a wide range of directions. For the case of a high stiffener, in general the transmitted and reflected amplitudes show an opposite behaviour, i.e., high transmission and low reflection coefficient or vice versa. However, the transmitted and reflected A_0 mode amplitudes do not balance the amplitude of the incident wave, and some of the energy is carried by the other scattered wave modes (S_0 & SH_0) due to mode conversation. In addition, energy could as well be trapped inside the high stiffener.

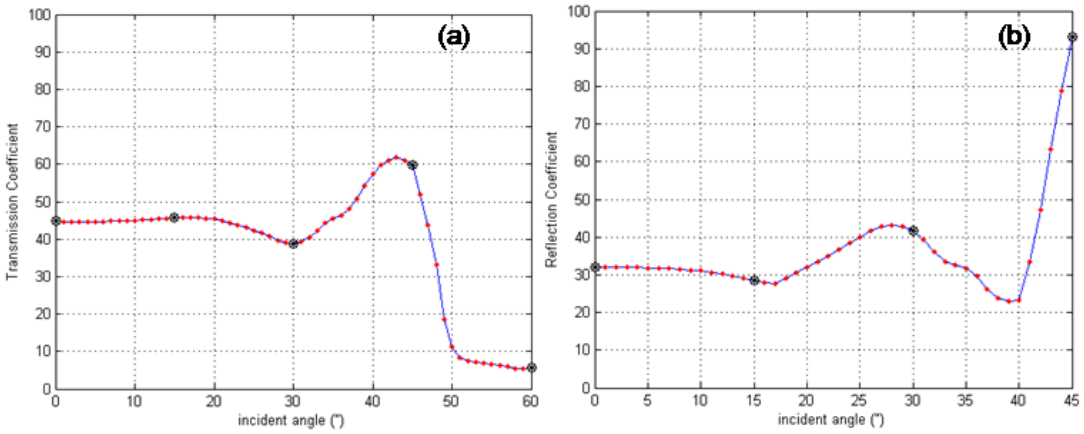

Fig 8.6 Coefficients of the transmitted (a) and reflected (b) waves from a tall stiffener (80 mm height, 15 mm thickness) at a range of propagation angles with black dots for comparison to Fig 8.4 & 8.5.

In the next step the effect of varying the thickness relative to the wavelength on the scattered A_0 wave mode from a short stiffener (height 5mm) was predicted (Fig 8.7). Considerable destructive and constructive interference was respectively observed at a stiffener thickness equivalent to half and full wavelength (Fig 8.7c) for the oblique transmission (45^o) across the short stiffener. The maximum and minimum reflection from the short stiffener (Fig 8.7d) was predicted at the same thickness (50% and 100% of the wave length respectively). The evaluation has again shown almost constant transmission and reflection coefficients for stiffener thickness larger than λ at 45^o propagation direction. The perpendicular (0^o) transmission and reflection from the short stiffener have shown similar behaviour to that obtained for oblique propagation (45^o).

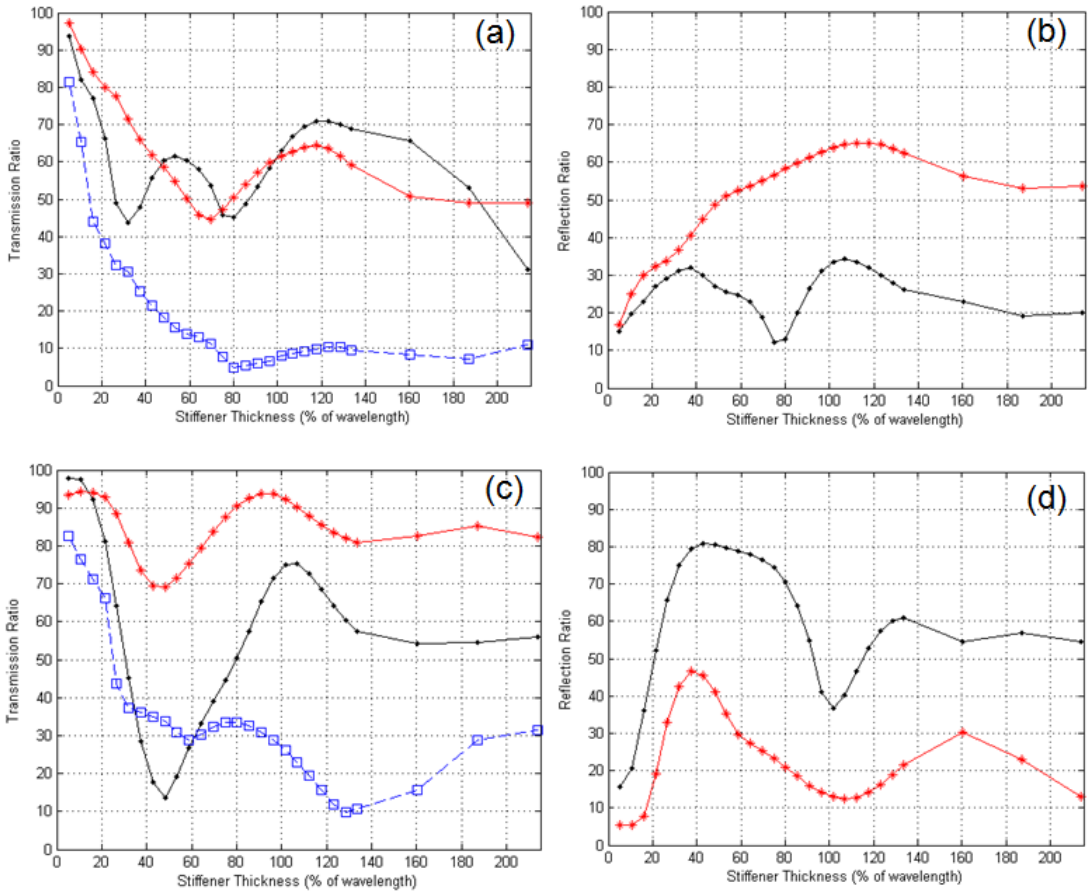

Fig 8.7 Transmission and reflection coefficients at 20 mm height (a, b) and at 5 mm height (c, d), for several thicknesses and incident angles, 0^o (dots, black), 45^o (stars, red) and 60^o (squares, blue).

A significant and sharp increase was obtained in the reflection at the short stiffener with increasing stiffener thickness up to 40% of the wavelength. The maximum reflection was observed approximately at the thickness that shows the minimum transmission coefficient (Fig 8.7c). Furthermore, the normal reflection from the 5 mm high stiffener was about twice the reflection at oblique propagation (Fig 8.7d), matched by a significantly lower transmission coefficient. Patterns of the scattered wave from the short stiffener were also investigated at 15^o and 30^o propagation angle (not shown). The obtained transmission and reflection coefficients at 15^o and 30^o were found to be reasonably similar to what have been predicted at the perpendicular propagation across the stiffener (similar to the 80 mm high stiffener investigated previously).

The effect of the multiple reflections due to the wave travelling inside the stiffener was more obvious in the prediction of the scattered wave field across the 20 mm stiffener height (Fig 8.7a & 8.7b). The transmission pattern at the normal and oblique propagation across the stiffener with 20 mm height, which is a medium high stiffener between the modelled tall and short stiffeners, was found to be more or less similar to the transmission across the short stiffener. On the other hand, reflected wave patterns from the medium high stiffener have shown reasonable match with the normal and oblique reflection from the tall stiffener (Fig 8.4b). The scattered wave field at the medium high stiffener has shown more or less similar transmission in the range of 0^o - 45^o, and then a significant reduction was obtained with increasing incident angle above 45^o (Fig 8.7a). The oblique reflection (45^o) from the medium high stiffener has demonstrated an increase with increasing thickness up to 100 – 120% of the wavelength, and then a constant reflection pattern was observed with small changes due to the signal interference (Fig 8.7b). The first destructive interference in the normal transmission across the medium high stiffener was observed for 35% of the wavelength, which also showed the constructive interference in the normal reflection pattern. The second minima in the normal transmission and the first minima in the normal reflection were observed at the same thickness, 80% of the wavelength, of the scattered wave field at the medium high stiffener.

The outcomes of varying the stiffener thickness have shown clear constructive and destructive interference in the wave scattering patterns at normal propagation. Similar scattering behaviour was attained in the patterns of the propagating waves between 0^o and 30^o. There was always a significant drop in the transmission coefficients with increasing propagation angle above 45^o. The pattern of the propagating waves at 60^o across a stiffener has shown a significant decrease in the transmission coefficients with increasing thickness (Fig 8.4a, 8.7a & 8.7c). In general, high transmission was obtained across thin stiffeners, and with increasing stiffener thickness significant decrease was observed at high propagation angles (above 50^o). The amplitude of the reflected wave was very low for a thin stiffener, and for thicker stiffeners more variation was observed with changing the incident angle. The scattering patterns at a short stiffener (Fig 8.7c & 8.7d) have predicted a slight increase in the energy carried by the A_0 mode (addition of the squared amplitudes) below 45^o incidence angle. Limited energy carried by the scattered A_0 mode can be predicted (10% of the incident energy) from a medium stiffener height with varying stiffener thickness above one wavelength (Fig 8.7a & 8.7b). Therefore, the energy carried by the S_0 and SH_0 modes increases to balance the reduction in the energy carried by the A_0 mode.

8.3 Variation of the Stiffener Height

The previous chapter showed significant differences in the waves scattering at high and short stiffeners. Therefore the effect of variations of the stiffener height on the transmitted and reflected wave was investigated. Variation of the stiffener height was implemented while the other model dimensions and excitation parameters were kept fixed to relate the change in the transmission ratio to the modified height. Numerical simulations using FE were performed at a range of stiffener heights from 1.25 mm up to 20 mm ($\sim\lambda$) using a 1.25 mm step size (element size in z-direction). To obtain more information about the wave scattering sensitivity to the stiffener height, using less simulations, the height has been varied from 20 mm up to 40 mm using a 5 mm step size, and from 40 mm up to 80 mm using a 10 mm step size. The transmission and reflection ratio, which are relative to the incident wave, were calculated for each simulated stiffener over the range of angles up to 60^o. In a first step the transmission

and reflection coefficients were predicted for the wave propagation across a 20 mm thick stiffener (Fig 8.8).

In general, significant variations were predicted in the scattering coefficients below 40 mm ($\sim 2\lambda$) stiffener height. Only small changes were observed in the coefficients of the transmitted and reflected waves above that height. The first transmitted and reflected pulses from the stiffener interfered with the second wave pulse from the wave propagation up and down inside the stiffener. Significant reduction was observed in the normal transmission across the stiffener, from 90% to 30%, with varying stiffener height up to 0.5λ (Fig 8.8a). This reduction can be attributed to the multiple reflections within the stiffener that cause destructive interference. Afterwards, the normal wave propagation pattern has shown a significant increase in the wave transmission, from 30% to 70%, with varying the stiffener height up to one wavelength. The maximum interference that resulted from the wave travelling inside the stiffener was found to be the main cause for the recorded increase in the transmitted wave. The second destructive interference in the normal transmission has been obtained with increasing the stiffener height up to 2λ, and then constant transmission is observed with small effect of interference at higher stiffeners.

The reflected wave at 0^o incident angle shows the opposite behaviour with a maximum reflection coefficient at $\sim 0.5\lambda$ stiffener height and a minimum at λ height (Fig 8.8b). The transmitted waves at 45^o propagation angle show a different behaviour with a continuous decrease with increasing stiffener height up to about $\sim 1.5\lambda$. Then again only small changes are observed in the transmission coefficient above $\sim 1.5\lambda$ stiffener height. The reflected waves at oblique propagation direction across the stiffener (45^o) show an initial dip and then constant increase with increasing stiffener height, again staying rather constant for a high stiffener (Fig 8.8b).

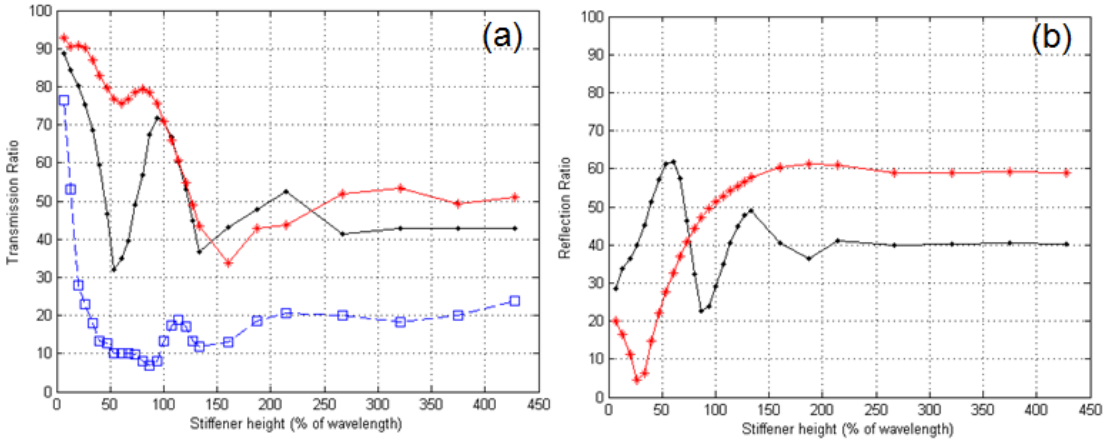

Fig 8.8 Ratio of the transmitted *(a)* and the reflected *(b)* waves from 20 mm stiffener thickness for different stiffener height at 0° (dots, black), 45° (stars, red) and 60° (squares, blue) incident angle.

Investigating the transmission behaviour at a larger propagation angle of 60° shows a very clear and sharp drop in the transmitted wave amplitude with increasing stiffener height. Then the transmission coefficient at 60° stays very low for high stiffeners. The evaluation has shown that constructive and destructive interference mostly occurred at perpendicular incidence across the stiffener. In a very clear harmonic behaviour, the maximum transmission was observed with the minimum reflection coefficients at a stiffener height of half the wavelength, and the minimum transmission was found together with the maximum reflection at a height corresponding to the wavelength. In a further step, the obtained change in the wave scattering behaviour with propagation angles between 0° and 45° was investigated using the predicted behaviour at 15° and 30° incident angle (Fig 8.9).

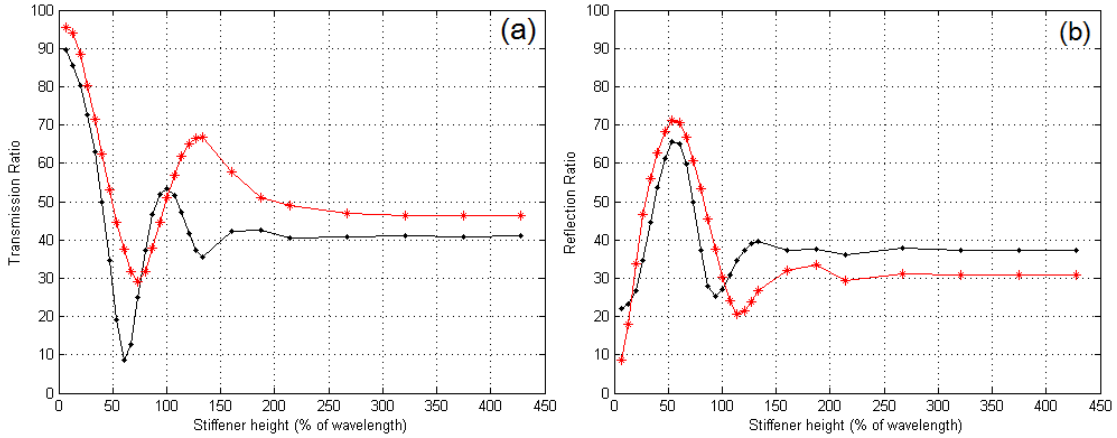

Fig 8.9 Ratio of the transmitted *(a)* and the reflected *(b)* waves from 20 mm thick stiffener for different stiffener height at 15° (dots, black) and 30° (stars, red) incident angle.

The evaluation at 15^o and 30^o propagation angle across stiffeners of different heights have shown a similar pattern with a slight shift, and were found to be very similar to the scattering behaviour at 0^o incident angle. With varying stiffener height, a clear constructive and destructive interference was observed at a height corresponding to about half and full wavelength for the scattered wave field at 15^o and 30^o (Fig 8.9). Then the scattering coefficients stay reasonably constant with increasing stiffener height above 2λ. The energy carried by the A_0 mode across a thick stiffener (Fig 8.8) is predicted to increase from 30% to 50% of the incident energy with increasing stiffener height above 1.5λ in the range of 0^o – 45^o incident direction. A significant amount of the incident energy is either trapped at the stiffener or mode converted to balance the reduction in the A_0 mode energy, and the calculation of the exact energy distribution would require further FE simulation.

Further investigations for the effect of varying stiffener height on the transmitted and reflected wave were performed using the FE simulation of the wave propagation across stiffener thicknesses corresponding to one and two times the plate thickness. The scattered guided wave field was predicted at 10 mm and 5 mm thickness for different stiffener heights (Fig 8.10). The variation in the scattering behaviour at the investigated thicknesses, 10 mm and 5 mm, was more obvious for short stiffeners ($h < 2\lambda$). For normal transmission across the stiffener a pattern with high transmissions coefficients due to constructive interference was obtained at the smallest considered height (1.25 mm), and heights corresponding to 0.5λ and λ. Low transmission coefficients due to destructive interference were obtained at about 0.25λ and 0.75λ height (Fig 8.10a & 8.9c). The normal reflection coefficient showed the expected opposite behaviour, with low amplitude due to destructive interference from a 5 mm thick stiffener obtained at 1.25 mm, 0.5λ and λ height, while high reflection coefficients due to constructive interference were obtained at 0.25λ and 0.75λ height (Fig 8.10d).

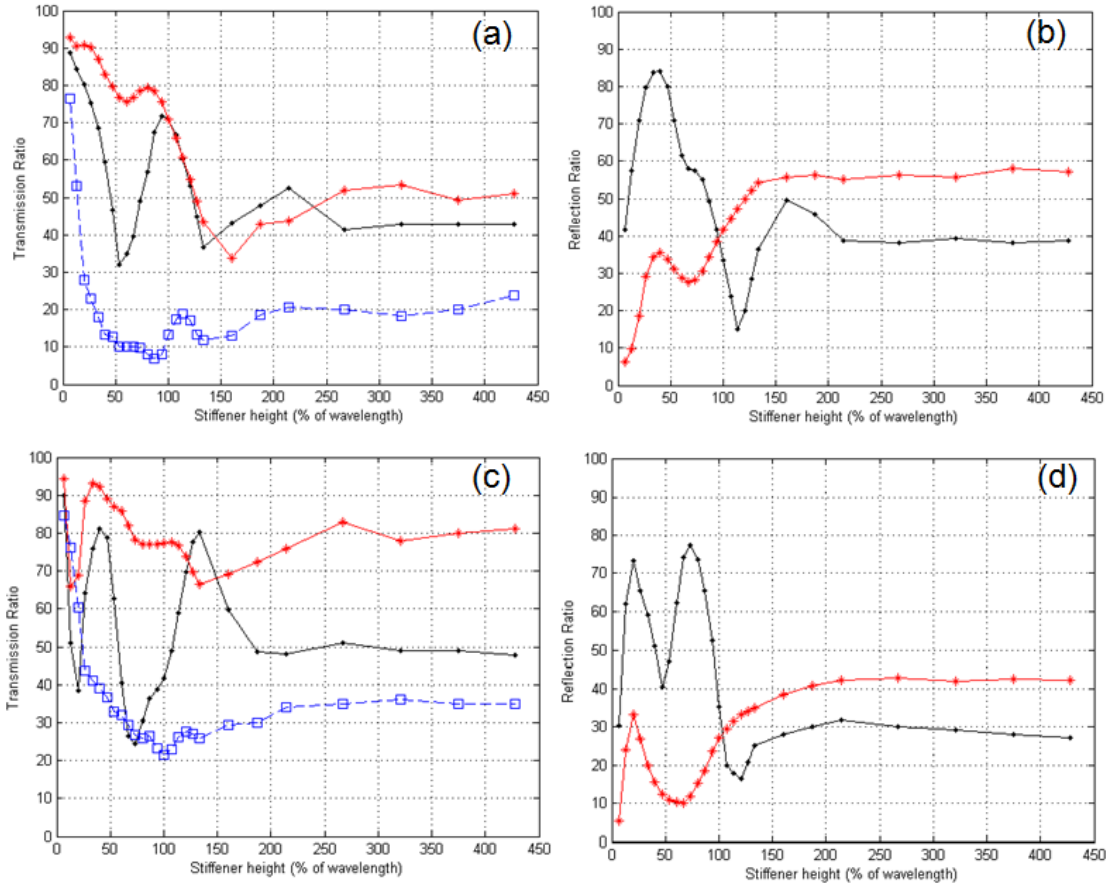

Fig 8.10 Transmitted and reflection coefficients at 10 mm thickness (a, b) and at 5 mm thickness (c, d), for different stiffener heights and several incident angles, 0^o (dots, black), 45^o (stars, red) and 60^o (squares, blue).

As the propagation angle increases from 0^o to 30^o, the observed wave scattering pattern was similar to what has been found at normal propagation direction. Then an obvious increase in the transmitted wave amplitude was observed at 45^o propagation direction. A more complicated wave scattering pattern was seen for different propagation directions before it showed a sharp decrease in the wave transmission at 60^o (Fig 8.10a & 8.10c). The comparison between the height variation for 5 mm and 10 mm stiffener thickness has shown that the oblique and perpendicular reflection from tall stiffeners ($h > \lambda$) is approximately constant (Fig 8.10b & 8.10d). Different behaviour was observed in the patterns of the normal and oblique reflections from short stiffeners (Fig 8.10c & 8.10d). Further evaluation was performed to understand the wave scattering behaviour for a range of the transmitted (0^o to 60^o) and reflected angles (0^o to 45^o). Studying the wave propagation across thin stiffeners (5 mm & 10 mm) shows a significant variation in the energy carried by the A_0 mode across stiffeners shorter than 1.5λ height (Fig

8.10). The expected transmission and reflection patterns from stiffeners taller than 1.5 λ height (Fig 8.10c & 8.10d) indicate a significant increase in the energy carried by the A_0 mode with increasing the incident angle up to 45^o. About 80% of the incident energy, which was calculated normalized to the incident wave mode (Eq 7.5), was found to be carried by the A_0 mode at oblique incident direction. Therefore, a slight amount of mode conversion and other effects are expected to appear at the oblique incident direction (45^o). With increasing stiffener thickness from 5 mm to 10 mm a significant reduction (from 80% to 25% of the incident energy) was obtained in the energy carried by the A_0 mode at 45^o. A significant amount of mode conversion and other effects appear to happen, in the normal and oblique propagation with increasing the thickness of the stiffener above 0.5 λ, but cannot be quantified without further investigation. For one stiffener geometry (50 mm height and 5 mm thickness) the coefficients of the transmitted and reflected waves were calculated for a range of propagation directions (Fig 8.11).

Slight variation was obtained in the transmission ratio between 0^o and 30^o. Then a stepped increase was predicted in the transmitted wave across the stiffener between 30^o and 45^o directions followed by a sharp decrease with increasing incident angle up to 60^o. Almost constant reflection with some variation was predicted in the range of 0^o - 40^o, with a significant increase for the 45^o propagation direction. Only small variations were observed in the transmission and reflection coefficients with varying stiffener height above ~2λ for all modelled thicknesses, 20 mm, 10 mm, and 5 mm. The variation in the transmitted and reflected wave pattern can be attributed to the wave travelling inside the tall stiffener (higher than 2λ) and multiple reflections from the stiffener sides. In addition to the initial interference from the first transmitted and reflected pulse from the stiffener, the multiple reflections within the stiffener can produce secondary interference affecting the scattered wave field. More complicated wave scattering patterns were observed for different propagation angles at lower stiffeners. The variation of the stiffener height has shown constructive and destructive interference at normal propagation direction. An almost similar wave scattering pattern was seen for the range of 0^o - 30^o direction of the wave propagation across most of the modelled stiffeners at different heights (Fig 8.11).

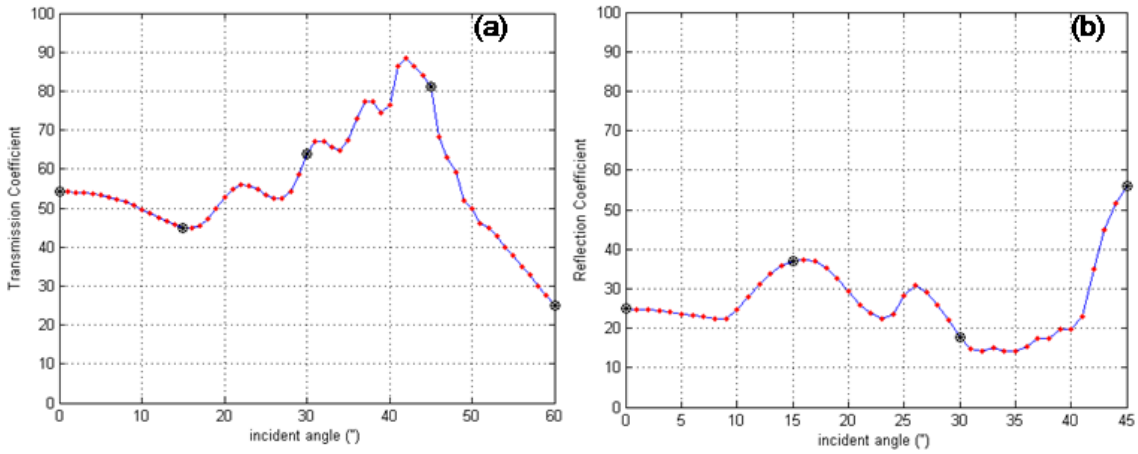

Fig 8.11 Coefficients of the transmitted (a) and reflected (b) waves from stiffener (50 mm height, 5 mm thick) at a range of propagation angles, black dots show coefficients discussed above.

Different behaviour was observed with varying stiffener height at 45^{o} incident angle for realistic stiffener thicknesses. The wave propagation in this direction has shown the maximum transmission coefficient in most of the cases. A sharp drop of the transmitted wave amplitude has been predicted between 45^{o} - 60^{o} incident angles. The transmitted wave across a stiffener has shown a high dependency on the propagation direction.

In general, the wave transmission across a stiffener was found to drop by over 50% for incidence angles above 45^{o}. Furthermore, the transmission ratio also drops at large stiffener size (higher than 3λ and thicker than) 1.5λ, due to the lost energy inside the stiffener. Based on previous research [31], varying the wavelength of the wave propagating across up and down steps with changing axial extent was found to shift the patterns of the reflected wave coefficients. The axial extent and wave velocity were found to have a significant effect on the predicted reflection pattern. Similar behaviour was observed from the patterns of the transmitted wave across a stiffener in the parametric study that has been conducted in this chapter. The maximum and minimum coefficients in the transmitted wave patterns were found to be shifted with increasing angle of the incident wave from 0^{o} to 45^{o}. The shift in the transmission pattern can result from the increase in the travel distance across the stiffener, and due to internal reflections inside the stiffener.

8.4 Variation of the Excitation Frequency

The sensitivity of the scattered guided wave field to the variation of the excitation frequency was predicted using the FE method. This preliminarily investigation can guide the experimental work and was performed prior to the practical inspection of the examined plate structure. The wave scattering at a stiffener of 80 mm height and 20 mm thickness was predicted in the first case considered. The transmitted and reflected energies of the A_0 wave mode at the simulated stiffener were observed at a range of excitation frequencies from 50 - 220 kHz (Fig 8.12).

The transmitted wave across the stiffener in the case of the perpendicular incident wave has shown a considerable linear increase in the transmission ratio with increasing excitation frequency (Fig 8.12a). The same observation was valid for varying propagation directions up to 45^o, but above that angle a significant change was predicted. The propagated wave across the stiffener at 60^o has shown a systematic increase in the transmission coefficient with varying excitation frequency up to 100 kHz. Then a constant value followed by a reduction was recorded in the transmission ratio with increasing excitation frequency. The results of varying the excitation frequency for a tall and thick stiffener indicated a significant reduction in the reflected A_0 wave mode. At low excitation frequency, roughly similar behaviour was predicted from the normal and the oblique wave reflection with changing wavelength due to the change in excitation frequency (Fig 8.12b). Wave reflection coefficients of 85% and 70% were obtained respectively from oblique and normal propagation at 50 kHz. A consistent decrease in the reflection coefficient was found for all incident angles with increasing excitation frequency. The comparison has also shown higher reflection from the perpendicular wave propagation with respect to the obtained reflection coefficient for oblique propagation above 120 kHz, with low values for all considered angles.

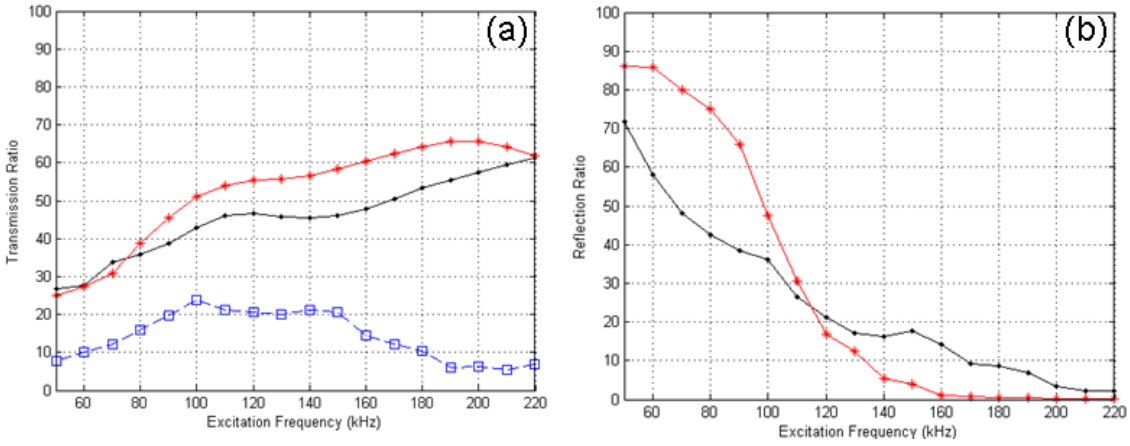

Fig 8.12 Ratio of the transmitted *(a)* and the reflected *(b)* waves from a stiffener of 80 mm height and 20 mm thickness for several frequencies at 0^o (dots, black), 45^o (stars, red) and 60^o (squares, blue) incident angle.

The changes in the transmission and reflection coefficients with varying propagation angles were examined for 15^o and 30^o propagation directions for the same stiffener size (80 mm height, 20 mm thickness) (Fig 8.13).

Consistent increase of the transmission coefficient was observed with increasing excitation frequency from 50 kHz to 220 kHz. In contrast, an almost linear drop in the reflected wave amplitude was predicted over the same range of frequencies. Based on the obtained transmission and reflection field at high stiffeners (Fig 8.11), the energy carried by the A_0 mode was calculated (addition of the squared amplitudes) and found in the range of 20 - 30% of the incident energy at several frequencies. Significant increase is expected in the mode conversion (the scattered S_0 and SH_0 mode) and other effects to balance the drop in the energy carried by the scattered A_0 mode at high stiffeners, relative to the energy of the incident mode.

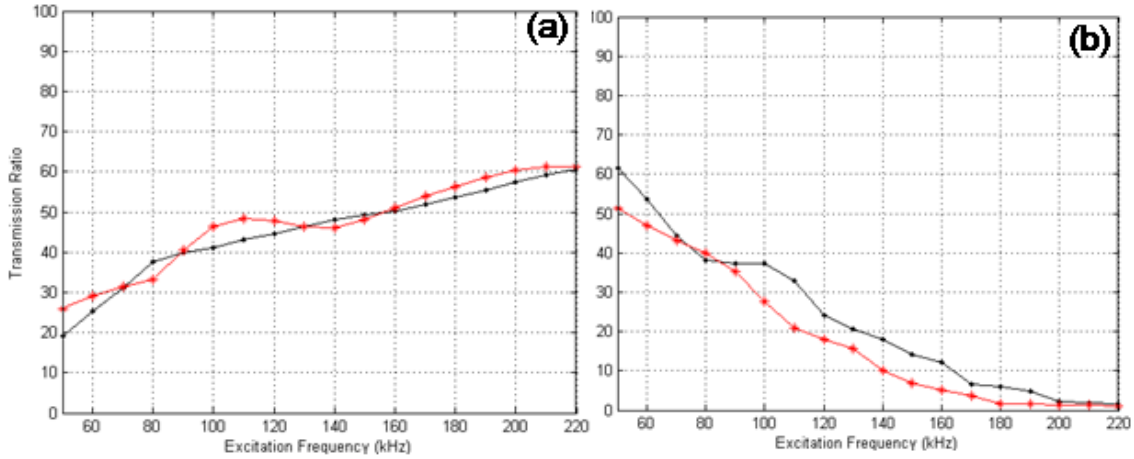

Fig 8.13 Ratio of the transmitted *(a)* and the reflected *(b)* waves from a stiffener of 80 mm height and 20 mm thickness for several frequencies at 15° (dots, black) and 30° (stars, red) incident angle.

Further investigations were performed for different stiffener dimensions. The transmission and reflection coefficients from two thin stiffeners with large and small height (size: 80 mm x 5 mm, and 5 mm x 5 mm) were predicted using the FE simulation (Fig 8.14).

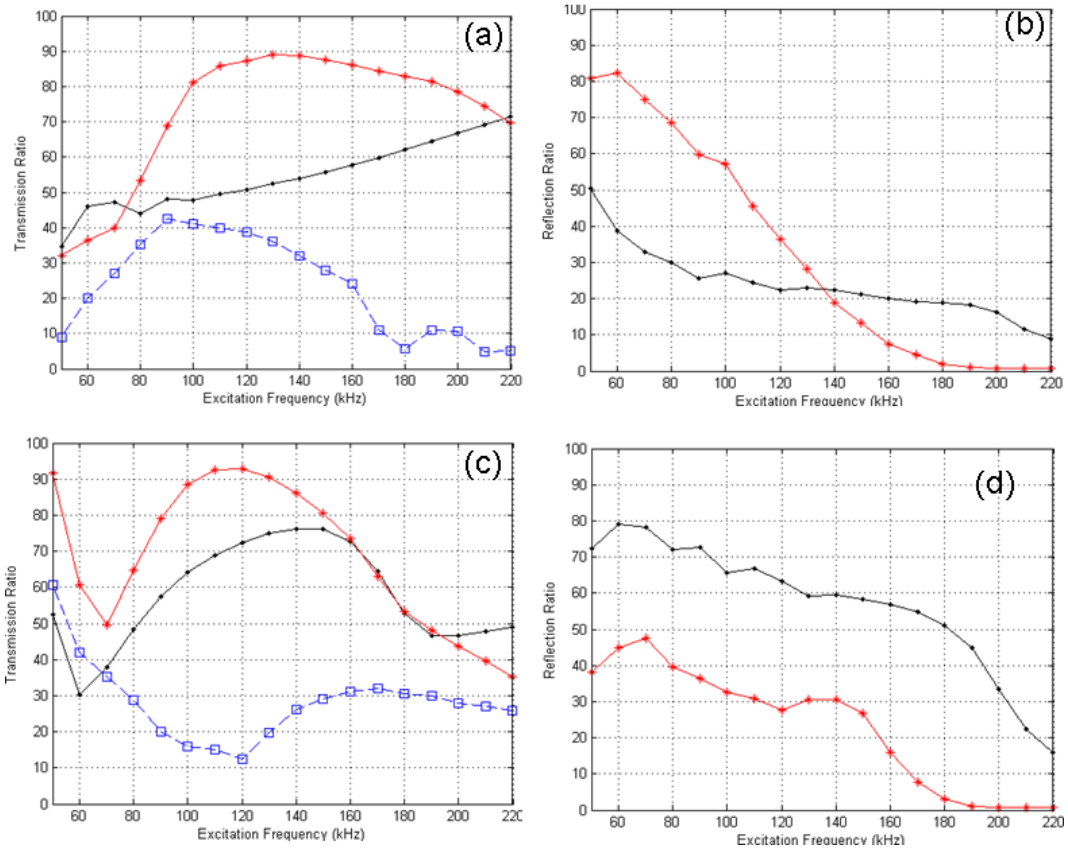

Fig 8.14 Transmission and reflection coefficients at 80 mm x 5 mm stiffener (a, b) and at 5 mm x 5 mm stiffener (c, d), for different excitation frequency and several incident angles, 0° (dots, black), 45° (stars, red) and 60° (squares, blue).

The predicted wave scatterings at a tall stiffener (80 mm x 5 mm) and at a short stiffener (5 mm x 5 mm) have shown a clear variation with changing excitation frequency and propagation direction. Similar behaviour was observed in the transmitted wave between 0^o – 45^o across the short stiffener (Fig 8.14c), while the pattern of the transmitted waves in these directions across the tall stiffener has shown a different behaviour (Fig 8.14a). Systematic increase was obtained in the normal transmission pattern across the tall stiffener with varying excitation frequency up to 220 kHz. The oblique transmission pattern at 45^o across the tall stiffener has shown a significant increase with varying excitation frequency up to 120 - 140 kHz, and then a slight reduction was observed with increasing excitation frequency (Fig 8.14a). Opposite behaviour was predicted in the propagating wave at higher angles (60^o) across the tall and short stiffeners. The transmission pattern at 60^o has shown maximum and minimum interference respectively at the tall and short stiffener (Fig 8.14a & 8.14c) in the same frequency range (100 – 120 kHz). The oblique reflection at 45^o from the tall stiffener (Fig 8.14b) was found to be twice the reflection obtained from the short stiffener (Fig 8.14d) below 100 kHz excitation. On the other hand, the normal reflection from the tall stiffener was found to be half of the normal reflection from the short stiffener for the same frequency range. The wave scattering pattern in the oblique propagation direction has shown almost negligible reflection from the tall stiffener for higher excitation frequencies above 180 kHz. The normal reflection from the tall stiffener has shown more constant coefficients with varying excitation frequencies from 110 kHz to 200 kHz. In contrast, about 65% reduction was predicted for the normal reflection coefficient from the short stiffener with increasing the excitation frequency.

The required energy balance between incident and scattered wave modes from a stiffener has been used to predict patterns of the mode conversion to the S_0 and SH_0 wave modes with varying excitation frequency. The energy carried by the A_0 mode at normal incidence direction, which was calculated normalized to the incident wave mode (Eq 7.5), has shown a significant increase (from 35% to 90%) with increasing the stiffener height at low excitation frequencies (Fig 8.14). On the other hand, the energy carried at 45^o incidence direction has shown opposite behaviour with changing the stiffener height from 5 mm to 80 mm. A considerable drop from about 65% to 10% of

the incident energy was observed with increasing the stiffener height at high excitation frequencies. Over the investigated range of frequencies, the expected mode conversion and other effects to balance the reduction in the A_0 mode energy (relative to the incident energy) was not much in the case of the high stiffener (Fig 8.14a & 8.14b). In contrast, the required mode conversion to balance the reduction in the energy carried by the A_0 mode (the addition of the squared amplitude) was found to be considerable at the short stiffener (Fig 8.14c & 8.14d).

Further comparison was performed between the coefficients of the oblique reflection from the tall stiffener at several excitation frequencies. The predicted reflection from the high stiffener in the oblique direction was found to be twice the one predicted from the short stiffener at low frequency. The change in the transmitted wave pattern due to varying incident angle with stiffener size and excitation frequency in different configurations was predicted. Additionally, the scattered guided waves at 15^o and 30^o incident angles from the tall and short stiffeners were predicted. The propagated wave across the stiffeners with 80 mm and 5 mm height at 15^o and 30^o did not show much difference to the predicted results at normal incidence (Fig 8.13). In contrast, the influence of varying stiffener height on the wave scattering pattern at angles above 45^o was significant, especially with increasing excitation frequency (Fig 8.14a & 8.14c). The previous investigations have shown that different scattering behaviour can be observed for variations of the excitation frequency and propagation direction, and this also varies for different stiffener geometries.

To conclude, an increase of the excitation frequency has shown an approximately systematic increase and decrease in the transmission and reflection coefficients respectively for a tall and thick stiffener. The reduction in the oblique reflected wave was significant and independent of the stiffener size in the frequency range 50 – 220 kHz. A systematic increase in the perpendicular transmission was observed with increasing excitation frequency at a realistic stiffener geometry, 80 mm height and 5 mm thickness. With varying excitation frequency, reasonably similar behaviour can be obtained for the transmitted and reflected waves from a short stiffener in a range of

directions between 0^o and 45^o. Above 45^o the transmission pattern was found to be changing to the opposite, a different behaviour with generally very low transmission coefficients. In general, good wave transmission across the stiffener requires an excitation frequency in the range of 100 – 160 kHz and wave incidence in the range of up to 30^o - 45^o propagation angle across the stiffener.

8.5 Recommendation for the Plate Monitoring

Designing a structural monitoring system requires *a priori* knowledge about the obtainable sensitivity in the experimental measurements to plan the distribution of the used sensors for the monitoring setup. Predicting the mechanisms that governs the scattered guided wave field at a stiffener was crucial for understanding the relation between the stiffener geometry and the propagated wave across it at normal and oblique directions. Almost all (about 95%) of the simulated models of the guided wave propagation and scattering at a stiffener with different dimensions have shown similar wave scattering pattern in a range of propagation directions from 0^o - 30^o. Only a maximum 10% difference was observed between the scattering coefficients of the predicted wave propagation for these directions. In general, the propagating wave in the range of 30^o- 45^o across the stiffener has shown a significant increase in the transmitted energy and the next chapter (chapter 9) will consider whether this energy is sufficient for defect detection. Above 45^o strong variations in the transmission behaviour were observed with typically rather low transmission coefficients. Therefore, the recommended largest monitoring direction for the propagated wave across the stiffener is 30^o if possible, or it can be varied up to 45^o as a maximum. One excitation location thus cannot provide full area coverage in the suggested range of propagation directions for good transmission across a welded stiffener, especially in a large plate structure. Therefore excitation and monitoring should be performed using several sensor configurations to obtain full area coverage at the required minimum wave transmission across the stiffener. Designing excitation and monitoring configurations that can ensure sufficient wave transmission across the stiffener (Fig 8.15) at reasonable detection sensitivity was found to be achievable.

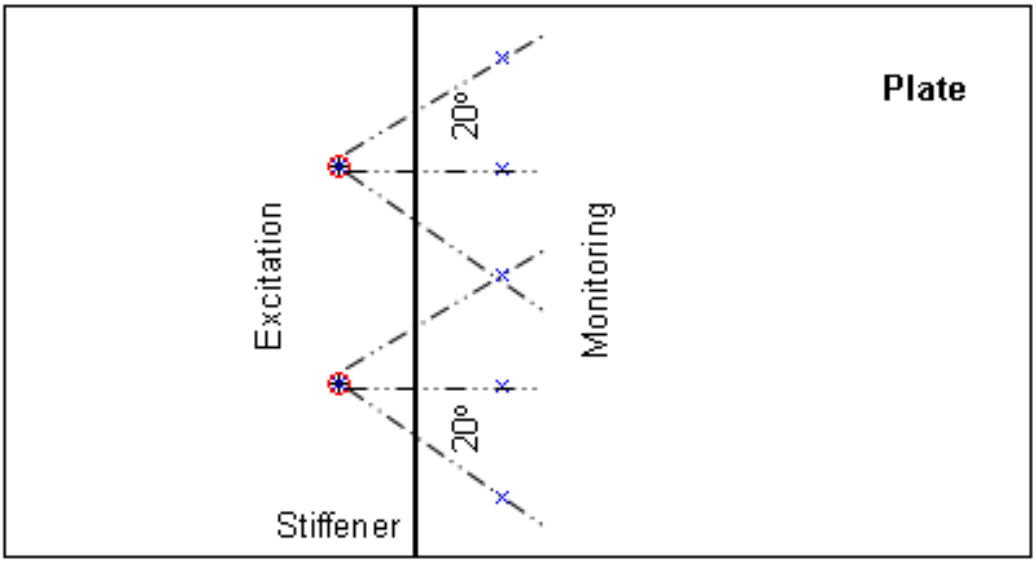

Fig 8.15 Excitation and monitoring design that provides good transmission across a stiffener in a plate structure.

However, there will be an area at and behind the stiffener in which the distributed array cannot detect defects effectively, and the detection in this area would require higher propagation angles across the stiffener above 45^{o}. Unfortunately, this is the critical area of the heat affected zone near the weld where the cracks and corrosion defects can be found. Therefore, increasing the number of the employed sensors along the weld (Fig 8.15) can be an alternative solution to obtain the required detection sensitivity. The similarity between wave scattering patterns in the range of 0^{o} - 30^{o} can reduce the required time for modelling through-thickness wave propagation in thin plates. Moreover, the required analysis for obtaining normal propagation across a stiffener is considered reasonably simple, and signal processing can be performed easily for the simulated time trace signals. In principle a 2D FE model, which requires limited computation time compared to a 3D model, could be used to simulate typical SHM applications with perpendicular wave propagation across the stiffener. Based on the match between patterns of the transmitted wave in the range of 0^{o} - 30^{o}, the 2D model can vary the excitation and monitoring parameters and predict the transmitted wave efficiently [77].

8.6 Summary

Stiffeners of rectangular cross-section were modelled to calculate the A_0 Lamb wave mode transmission and reflection for different stiffener dimensions and excitation frequencies. Wave propagation was monitored using two sets of monitoring points arranged in parallel lines ahead of and behind the stiffener. The FE simulation was utilized to obtain a relation between the direction of the propagated wave across the stiffener and the magnitude of the transmitted and reflected waves. The required time separation was calculated before varying the stiffener dimensions and studying the wave scattering at the stiffener. The verified wave processing algorithm from the previous chapter has been used for calculating the coefficients of the transmitted and the reflected A_0 Lamb wave mode at the stiffener. Wave transmission at a wide range of incident angles (0^o – 60^o) was calculated for different stiffener geometries. The findings of the wave transmission for different stiffener heights and thicknesses were compared. The reflected waves were analyzed for a more limited range of directions (0^o – 45^o). Typically a significant drop was observed in the transmitted wave across the stiffener at incident angles above 50^o. The predicted wave transmission across tall and thick stiffeners was not as good as the transmitted wave across short and thin stiffeners, but was found to be high enough for SHM applications.

The variation in the scattered wave field due to variations of the stiffener size has been analyzed. The change in the wave scattering behaviour was studied for a realistic variation of the excitation frequency. The change in the energy carried by the A_0 mode at several stiffener geometries and different propagation directions has been discussed. However, calculating the exact energy carried by the other modes, due to mode conversion to the S_0 and SH_0 wave modes, requires further FE simulations. Similar patterns of the transmitted and reflected waves from a stiffener for a range of incident angles up to 30^o were found, potentially allowing the modelling of further variations in the stiffener geometry using faster 2D FE simulations. Propagation directions up to 30^o are recommended to ensure good transmission across the stiffener. The detection sensitivity in inaccessible areas behind the stiffener was discussed and found to be dependent on the incident angle.

Chapter 9

Analysis of the Wave Reflection from a Flaw located behind a Stiffener

Areas of stress concentration around welded structures are likely to lead to fatigue cracks. Performing periodical nondestructive testing for these areas is crucial for maintaining structural health and preventing accidental shutdown of the system. Structural damage can be localized using a distributed array of sensors that monitors Lamb wave propagation in the plate structure. Wave reflections from a defect can be monitored and analyzed based on known information about the excitation and monitoring locations. However, the problem with stiffened plate structures is accessibility that might prevent access to some parts of the structure to be inspected. This means that placing SHM sensors in all parts of the stiffened structure is not always possible, and that excitation and monitoring sensors can only be placed in the accessible parts. In this case, the guided wave propagated across the stiffener would allow the inspection of the inaccessible part, i.e., behind the stiffener (Fig 9.1), using limited access to one side of the stiffener.

The capability of a SHM system that could be used for observing a defect behind a stiffener mainly depends on the magnitude of the reflected wave from the monitored defect in the targeted area. The configuration that can assure adequate energy for wave propagation and transmission twice across the stiffener, taking the reflection from the damage into account, has been discussed in this chapter.

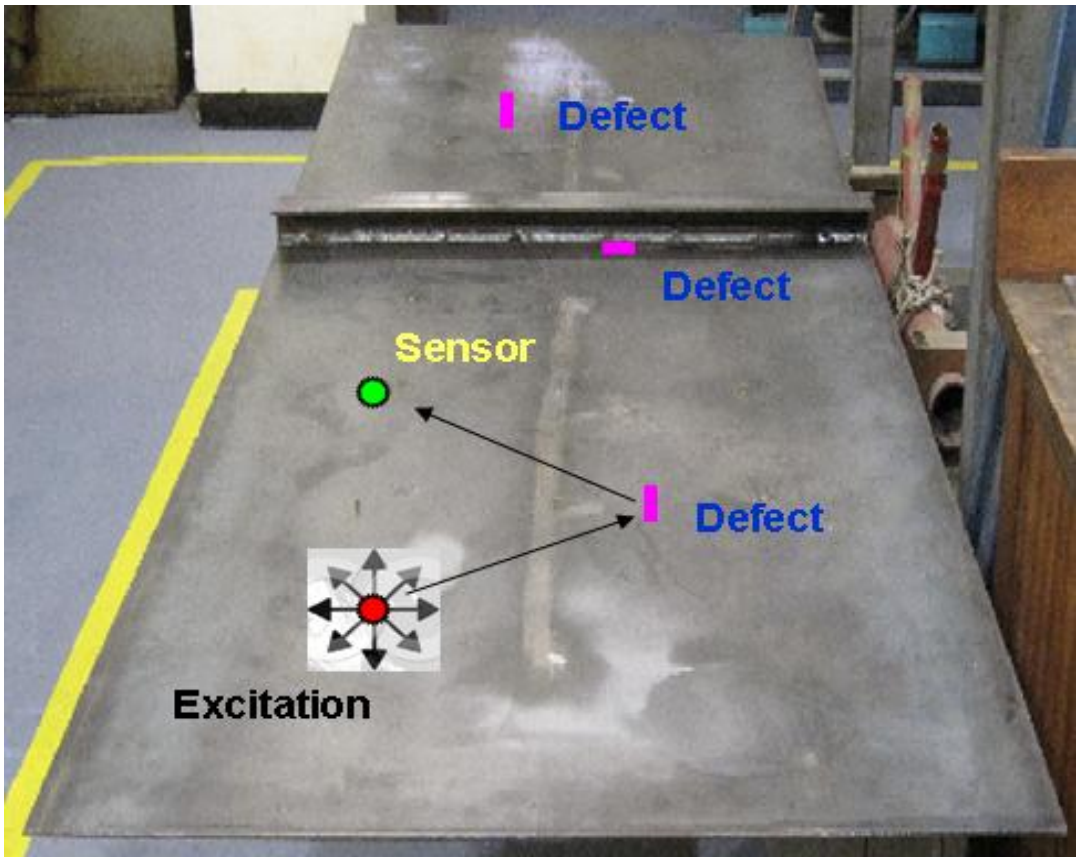

Fig 9.1 Schematic of steel plate with welded stiffener showing the excitation of GUW and the monitoring of its reflection from several expected defects using distributed array of PZTs.

Knowing whether the reflected energy from a defect is sufficient or not for the damage detection requires a *priori* knowledge about the acceptable noise in the measured time trace signal. The ability of the used experimental set-up in the SHM system to obtain the required signal quality is another important aspect to be considered before selecting the detection method. The detectable signal amplitude should be investigated experimentally before evaluating the measurements. The signal-to-noise ratio (SNR) was found to be a good parameter to check the quality of the measured pulse relative to the noise level in the time trace signal. The reflected pulse from a defect should be above 1% (40 dB) of the excited wave amplitude to be measurable, as found in previous research [55]. Ideally, in order to obtain a clear defect signal the noise in the signal should be less than one tenth of the defect pulse (20 dB). In this case, the ideal SNR would be 60 dB, with the excitation pulse 1000 times larger than the noise level in the measured signals.

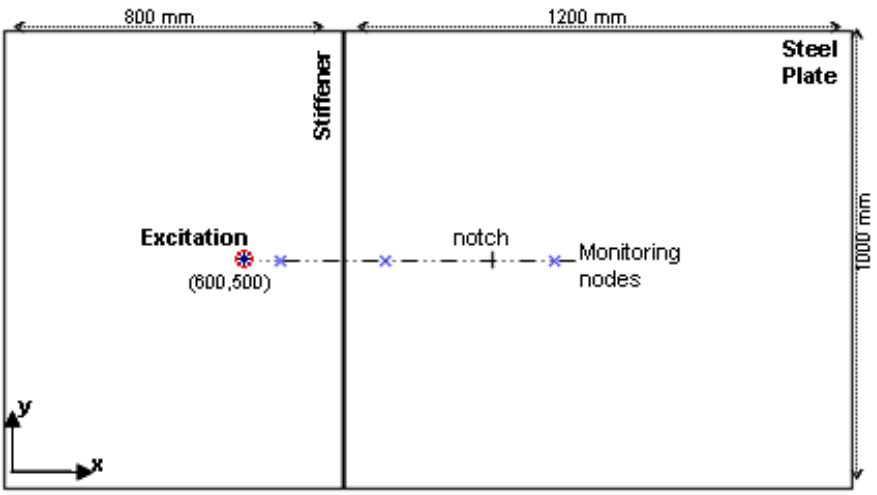

Fig 9.2 Schematic of plate model with stiffener along the width and notch modelled behind the stiffener to investigate wave propagation on a line of monitoring nodes between the excitation point and notch.

9.1 Prediction using FE Simulation Models

FE models were employed to simulate the A_0 wave mode reflection from a notch behind the stiffener. The same notch geometry was modelled at various distances from a simulated stiffener. The notch location behind the stiffener was varied to study the limitations of detecting damage at inaccessible areas. The steel plate of 2 m length and 1 m width, 5 mm thickness, with an L-shaped stiffener used for the experiments was simulated (Chapter 4). The excitation was modelled in the middle of the plate at a distance of 200 mm from the stiffener (Fig 9.2) in order to maintain sufficient time separation for the reflected waves from the stiffener and plate edges. The reflected wave from the simulated notch was monitored along a perpendicular line between the excitation point and notch (Fig 9.2). The purpose was to investigate and understand the guided wave

The simulated time trace signals of the wave propagation and scattering were processed. Matlab code was employed to analyse the modelled signals using the maximum of the signal envelope. The wave displacement at each monitoring location across the stiffener was evaluated. The wave propagation across the stiffener and scattering from a notch (20 mm length; 5 mm through thickness) located respectively at 2 mm, 150 mm, 300 mm and 450 mm behind the stiffener (Fig 9.2) was predicted. Efficient evaluation was performed to show the normalized amplitude of the reflected wave from the stiffener and the transmitted wave past the notch (Fig 9.3).

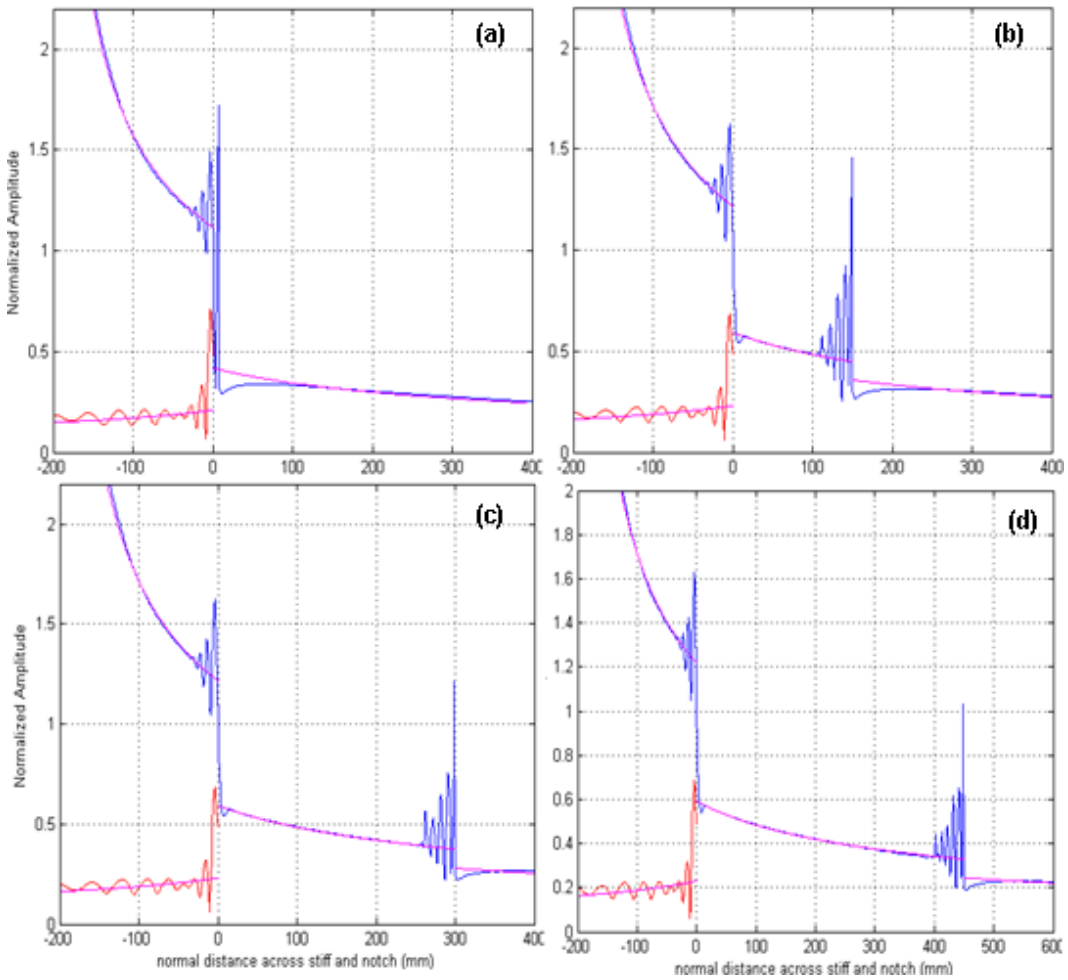

Fig 9.3 Normalized amplitude of the reflected (red) and transmitted (blue) waves at 0^o direction across stiffener (zero position) and notch at (a) 2 mm, (b) 150 mm, (c) 300 mm and (d) 450 mm behind stiffener.

Exactly the same scattering pattern was predicted from the simulated notches behind the stiffener (Fig 9.3b, 9.3c & 9.3d) as expected. The predicted wave scattering field from the notch at the stiffener location (Fig 9.3a) was overlapped on the scattering pattern of the stiffener. The amplitude of the signals at normal propagation and transmission across the stiffener and notches have shown the expected match with $1/\sqrt{r}$, the radial spreading curve of the guided waves (Fig 9.3). The time trace signal containing the notch reflection using access to one side of the plate, i.e., excitation and monitoring at the same point, were simulated. The reflected waves back from the notch at different locations past the stiffener are shown in Fig 9.4.

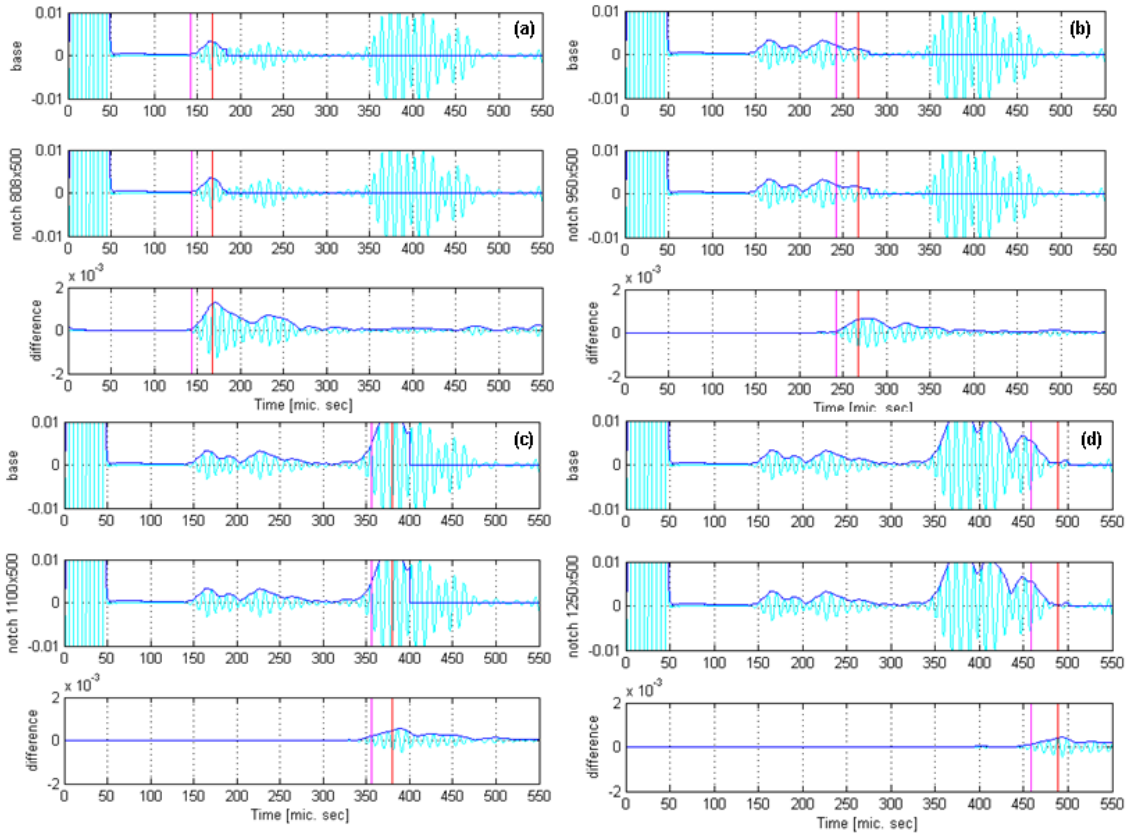

Fig 9.4 Difference between baseline and defect signals (monitored at excitation point) showing maximum envelope (red line) and expected arrival time (magenta line) of time gated reflection from a notch at (a) 2 mm, (b) 150 mm, (c) 300 mm and (d) 450 mm behind the stiffener.

The above time traces show a high percentage of overlap of the notch reflection pulse with secondary reflections from the stiffener and plate edges as would be expected for a realistic structure. Baseline subtraction method has been used to remove the secondary pulses. Separation of the notch reflection from the plate edges and stiffener reflection was obtained in the residual time trace signals (Fig 9.4). The amplitude of reflected A_0 wave mode from the simulated notches past the stiffener is found to be below 20% of the first stiffener reflection pulse using single plate side access. Finite element prediction was used to calculate the ratio of the reflected wave pulse from a simulated notch at 150 mm, 300 mm and 450 mm distance from stiffener location. The normal signal analyzing method using the maximum of the envelope has shown considerable local interference in the amplitude of the reflection from the notch as it was difficult to separate it from the wave scattering at the stiffener. Therefore, a different analyzing method has been used to isolate the notch reflection from the stiffener scattering.

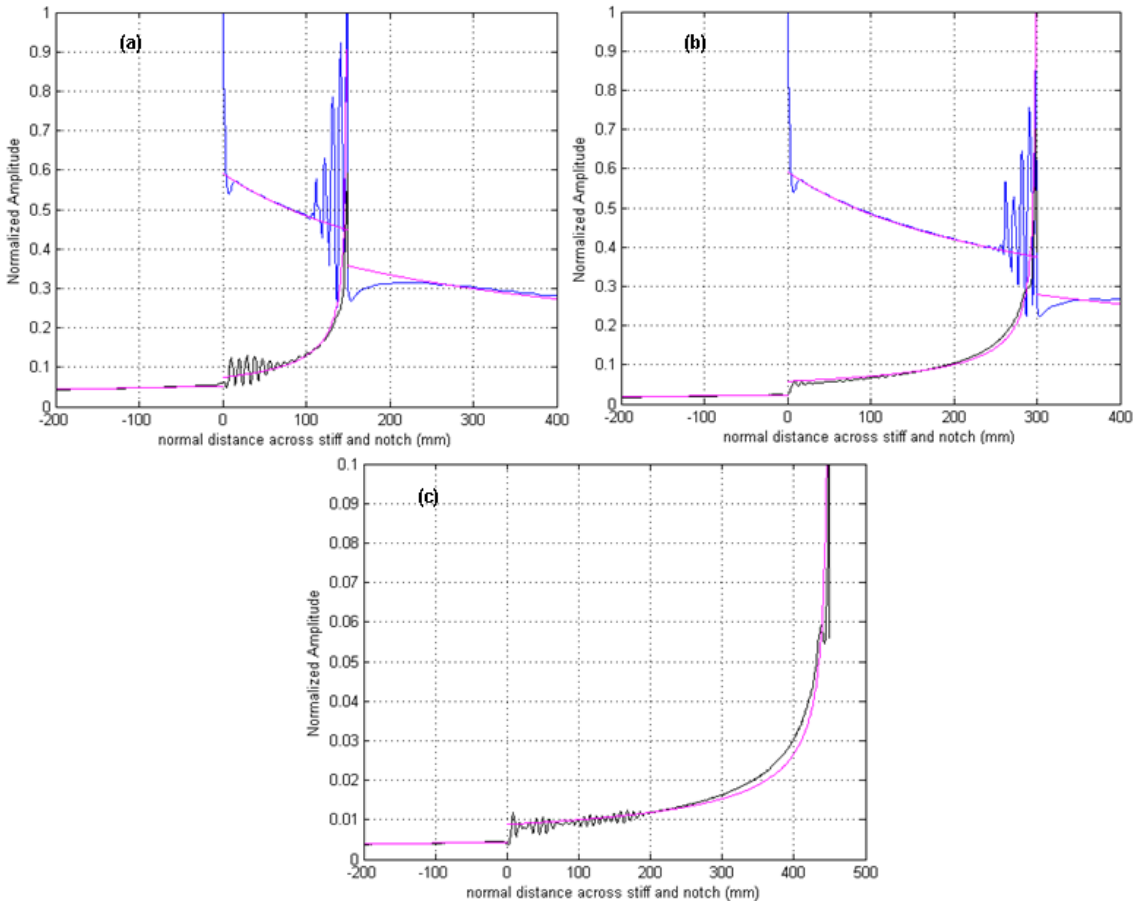

Fig 9.5 Normal transmission (blue) and reflection (black) calculated using baseline subtraction from notch at (a) 150 mm, (b) 300 and (c) 450 mm past stiffener location at zero position and radial spreading $1/\sqrt{r}$ (pink).

A baseline model of the intact stiffened plate without a notch has been used to predict the normal wave propagation and scattering at the stiffener. The residual signal after subtracting the stiffener scattering field from the notch reflection has been used to calculate the amplitude of the reflected pulse from the notch. This baseline subtraction allowed the accurate prediction of the notch reflections at different distances behind the stiffener (Fig 9.5).

Based on the literature review [57], using baseline subtraction has shown limitation for observing small changes (below 40 dB) in the time trace signal. Using the predicted transmission and reflection coefficients from the previous chapter, especially the normal scattering at a stiffener, the incident and scattered wave amplitude can be computed and corrected at any point on the plate. The back reflection from a defect at a

known distance past the stiffener can be calculated effectively. The received signal at a defect using single plate side access can be predicted taking into account the amplitude decrease due to the radial wave spreading ($1/\sqrt{r}$), the ratio of the transmitted wave across the stiffener (towards the notch), the reflected wave from the notch, and the transmission across the stiffener again towards the sensor element. This means that the notch reflection from any distance behind the stiffener can be calculated effectively without using additional numerical simulations. Based on the FE prediction of the scattered guided wave field at the L-shaped stiffener (Fig 9.3b, 9.3c & 9.3d), 60% of the incident wave was transmitted at normal propagation across the stiffener. The normal notch reflection was 22% of the incident wave at the notch (Fig 9.5a, 9.5b & 9.5c). The reflected wave from notches at 150 mm, 300 mm and 450 mm behind the stiffener has been calculated theoretically relative to the first reflected pulse from the stiffener (Fig 9.3). A good match has been achieved between the numerical and theoretical prediction of the notch normal reflection that was received at the excitation point using access to one side of the plate (Table 9.1).

The evaluation results have in principle shown the capability to obtain the amplitude of the reflected wave from a notch located behind a stiffener with access to only one side of the stiffener. Significant drop was observed in the signal amplitude due to radial spreading of the excited wave, propagation across the stiffener towards the notch, and then notch reflection that was received at the excitation point in front of the stiffener. The obtained signal amplitude after baseline subtraction should be above 10% (20 dB) of the first stiffener pulse to be detectable. The predicted amplitude of the reflected wave from a notch located at 300 mm - 450 mm behind the stiffener was 10 - 2% relative to the 1st reflected pulse from the stiffener and insufficient to detect and characterize a damage employing access to one side of the plate. For detecting damage further than 300 mm behind the stiffener, monitoring using array configurations with access to both sides of the stiffener is required.

Table 9.1 Normal reflection from notch at 150 mm, 300 and 450 mm behind stiffener location predicted (relative to the 1st stiffener pulse) at the excitation point using access to one side of the plate.

Prediction Method	Notch reflection relative to stiffener pulse (%)		
	150 mm behind stiffener	**300 mm** behind stiffener	**450 mm** behind stiffener
Numerically (FE)	20	10	2
Theoretically ($\frac{1}{\sqrt{r}}$)	24	12	2

9.2 Experimental Measurements with FE Verification

The normal reflection from a machined through slot (approximately 20 mm length; 5 mm through thickness) was measured experimentally to validate the output of the simulated A_0 wave mode scattering from a notch behind stiffener. The slot was machined at 200 mm past the stiffener location. Two piezoelectric transducers were glued next to each other on the laboratory plate, one of them to excite A_0 wave mode and the other to detect the stiffener and slot reflection (Fig 9.6). Additional laser measurements of the guided wave were performed on the opposite side of the stiffener behind the slot to check the possibility of detecting the scattered guided wave field at that location. Wave excitation and monitoring was performed at 100 kHz for baseline measurements and defect measurements, which were recorded respectively before and after cutting the slot in the plate. The dimensions of steel plate (2m x 1m x 5mm) available were modelled using the excitation/monitoring configuration and the notch geometry that was suggested in the optimization stage (Fig 9.6). The propagation of the A_0 wave mode in two FE models, with and without a notch, was analysed to predict the behaviour of the scattered waves for the experimental detection and the residual signal after baseline subtraction.

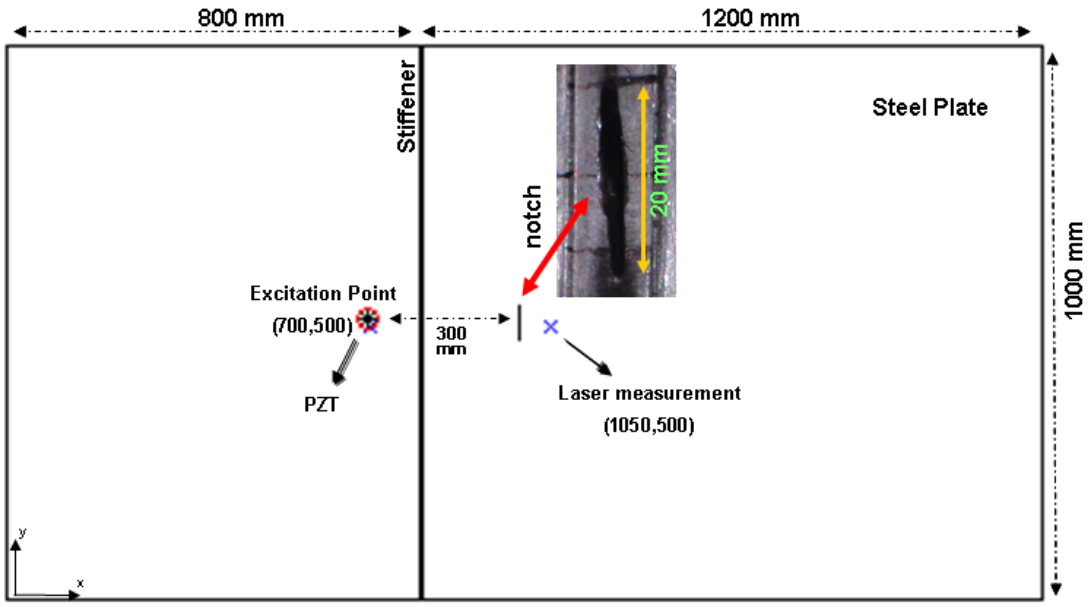

Fig 9.6 Schematic of A_0 mode excitation and reflection from a notch (20 mm length) behind the stiffener showing measurement locations using PZT (at excitation location) and laser beam (50 mm behind notch location).

The same signal processing steps were performed to evaluate both the FE simulation and the experimental measurements for the stiffener and notch geometries. The processing steps were applied to identify the first reflection from the stiffener and notch using a *priori* knowledge about their locations in the plate and the expected arrival times of their pulses in the time domain signal. The change in the waveform due to artificial damage was quantified and then compared with the recorded signals before and after damage introduction.

9.2.1 Accessibility to both Plate Sides

In the first stage of the investigation, the ability of detecting an artificial slot behind the stiffener using laser measurements close to the defect location was discussed. The change in the waveform at 250 mm behind the stiffener was simulated numerically before and after adding the notch to the model (Fig 9.6). For an experimental validation, the baseline and defect signals were measured at 50 mm distance behind the slot (Fig 9.7).

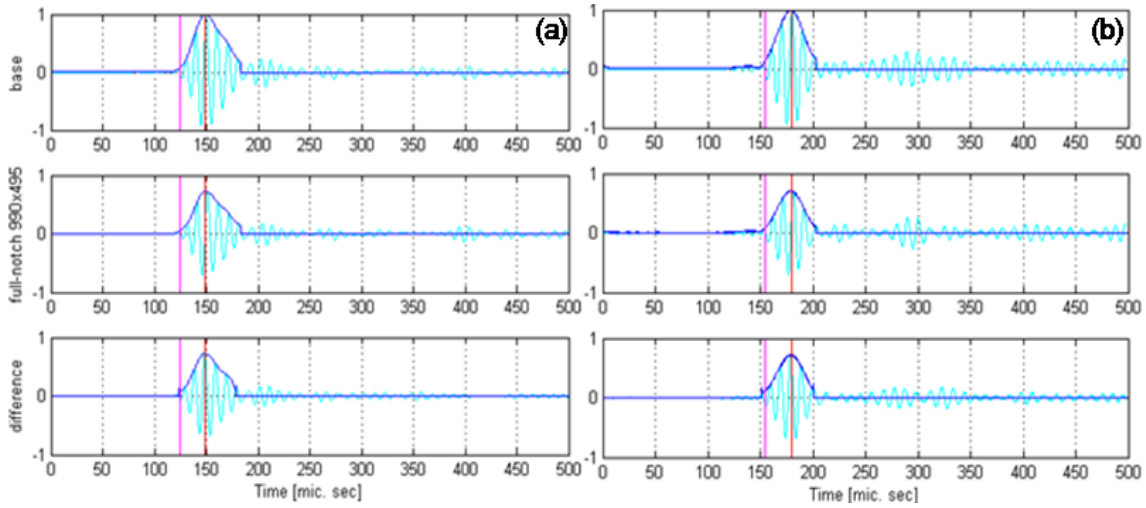

Fig 9.7 Difference between baseline and defect signals at 50 mm past through thickness notch showing time gated reflections from (a) FE prediction and (b) measurements.

The change in amplitude of the transmitted wave behind the notch was predicted from the FE simulations and was about 70% relative to the incident wave pulse for the undamaged plate with a stiffener (Fig 9.7a). A slight delay (Half pulse length) in the arrival time was observed in the experimentally measured wave at 50 mm behind the notch location (Fig 9.7b), which might be due to a problem in the triggering. The experimentally measured change in amplitude due to the scattering from the slot was again about 70%, significant enough to allow detection of the defect as expected (Fig 9.7b). Using two-side-access monitoring has shown a good match between the predicted and experimentally measured wave scattering at the notch. Given the fact that the weld butt and material changes due to welding process have not been modelled and that the size of the machined slot did not match exactly the modelled notch, the agreement in the results is very satisfactory. Measurement with the laser interferometer behind the notch is obviously not the ideal approach to detect and characterise damage in a typical onsite inspection, but it was used here to ensure that the utilized methods for modelling and signal processing can predict what would be measured experimentally.

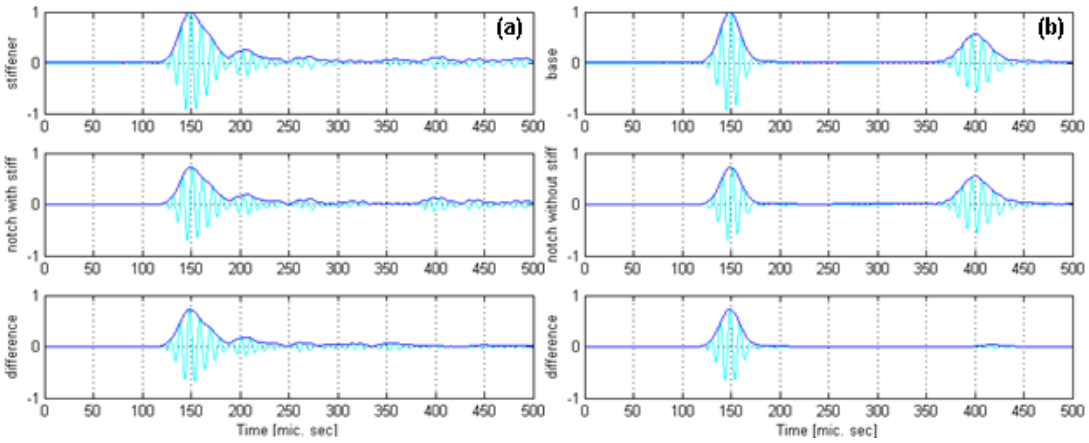

Fig 9.8 Residual signal after baseline subtraction predicted behind the notch using FE plate model (a) with stiffener and (b) without stiffener.

Another numerical simulation was performed without the stiffener to investigate the difference between the scattering at the notch, with and without the stiffener present (Fig 9.8). The residual (difference) signal after baseline subtraction of the predicted scattering at 50 mm behind a notch past a stiffener (Fig 9.8a) was compared with the residual signal in the case of plate model without stiffener (Fig 9.8b). About 8% difference (normalized to incident wave) has been observed due to the effect of the stiffener.

9.2.2 Single Plate Side Accessibility

In the second stage, the ability for the detection of the signal change due to a defect located behind the stiffener was examined using a PZT sensor at the excitation location (the accessible part of the structure). Experimental measurements of the reflected wave from a through-thickness slot located 200 mm behind the stiffener were performed using the monitoring method of single-sided access. A comparison was performed between the experimental results and the numerical prediction (Fig 9.9). The residual signals after baseline subtraction for the FE prediction (Fig 9.9a) and the experimental measurements before and after cutting the slot (Fig 9.9b) were evaluated. To observe a significant difference in the subtracted signals, sufficient wave reflection from the through thickness notch is required. Defect detection behind a stiffener in a plate-like structure requires significant back reflection (14 dB of the 1st stiffener pulse), which is more than 1% (40 dB) of the excited pulse. The normal analysing method of the experimental measurements at the excitation location showed a signal to noise ratio

(SNR) equivalent to 1.9% of the incident wave pulse (Fig 9.9b). The experimental defect reflection pulse was quantified relative to the excited pulse as 2%. This means that the SNR was too high relative to the defect reflection. In comparison, the FE simulations predicted notch reflection using the single plate side access was found to be 1.3% of the excited wave, which is about 4 dB of the detectable back reflection.

In the experimental baseline subtracted signal wave amplitude larger than the expected change in the stiffener reflection, about 4 dB, was observed in front of the slot pulse. The pattern of the additional pulses in the residual signal appears similar to the pattern of the reflections at the stiffener in the baseline signal (Fig 9.9b). The numerically predicted A_0 wave mode before and after introducing the notch obviously did not show these secondary pulses in front of the notch reflection pulse in the residual signal (Fig 9.9a). The appearance of the extra pulses in the PZT measurements might be attributed to several causes. The measurements' sensitivity to temperature change could be a possible reason for the observed changes [55]. However, in this case it was probably due to electrical problems with a wire connection becoming loose during the measurements and requiring re-attachment. Further checks were performed to identify the extra pulses ahead of the slot reflection pulse. The reflection from the slot behind the stiffener was measured for different slot length and depth using the PZT transducer at the accessible side of the plate.

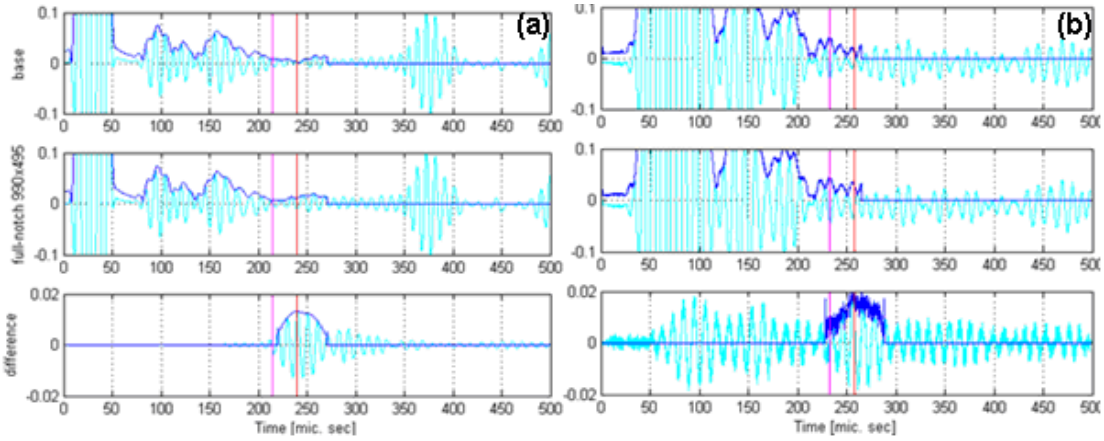

Fig 9.9 Baseline subtraction of signal obtained at excitation location showing the time gated reflection from a through thickness notch (20 mm length) located 200 mm behind the stiffener, (a) predicted and (b) measured.

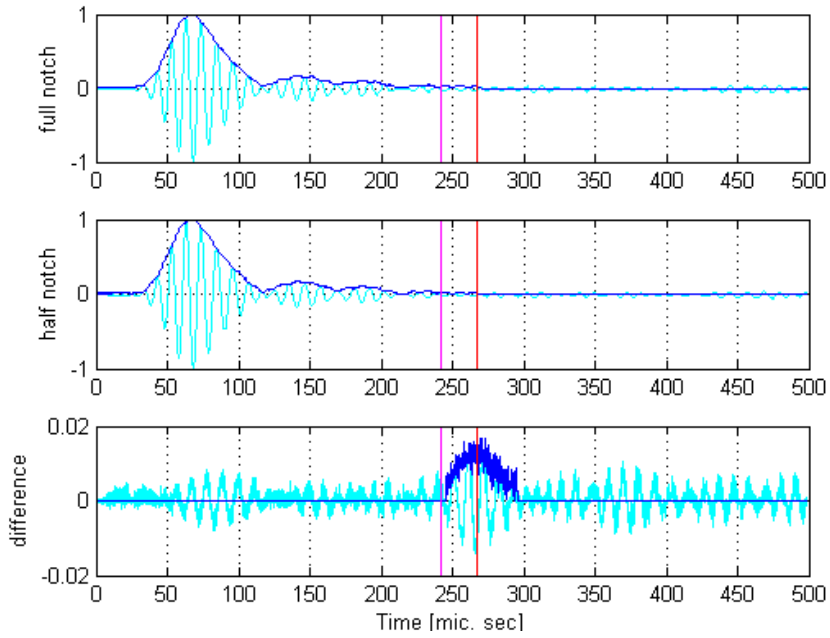

Fig 9.10 One-side-access measurements showing baseline subtraction of the normal reflection from two slots machined with different depth in the same location behind stiffener.

The difference between the two measurements, which shows the change in the wave reflection from the part-thickness to the through-thickness slot, was evaluated (Fig 9.10). Significant reduction was observed in the noise level of the residual signal that was obtained from the subtraction of the wave measurements at different slot depth (Fig 9.10). The obtained SNR from the difference of slots reflections that were received at the excitation zone was about 0.4% of the incident wave pulse. The observed amplitude from the residual slot pulse was quantified relative to the excited pulse as 1.6%, which is four times higher than SNR. The PZT measurements have shown the clear need for eliminating any secondary pulses in the residual signal when there is limited access to the plate. Evaluation of the secondary reflections in the time trace signal requires advance signal processing strategy, and some knowledge about the expected defect type and orientation in the inspected area [49]. Further analysis for the predicted reflection from the notch, simulated with and without the stiffener, was performed (Fig 9.11). Taking into account the excitation and monitoring at one side of the stiffener and wave reflection from the simulated notch behind the stiffener location, the difference after baseline subtraction was calculated (Fig 9.11a). The normal notch reflection that was received at the excitation point in front of the stiffener was compared with the notch reflection in the case of plate model without a stiffener (Fig 9.11b).

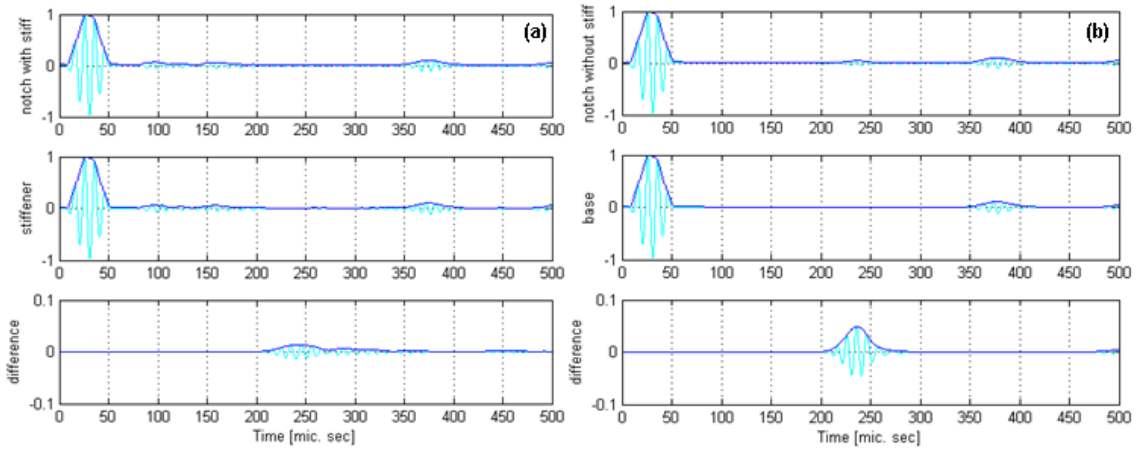

Fig 9.11 Residual signal after baseline subtraction predicted at the excitation location using FE plate model (a) with stiffener and (b) without stiffener.

About 71% reduction in the amplitude of the reflected wave from the notch was observed in the presence of the stiffener. A comparison was performed between the predicted normal reflection from a notch in a stiffened and non-stiffened plate using access to one or both sides of the stiffener (Table 9.2).The predicted reflection from the simulated notch behind the stiffener was validated experimentally employing accessibility to one or both sides of the plate, and a good agreement has been obtained (Table 9.2). In principle, detection of damage behind a stiffener requires high defect reflection received at the excitation location if there is limited accessibility to the plate.

Table 9.2 Measured and predicted notch reflection (relative to the excited pulse) in a stiffened and non-stiffened plate using single side and two sided access.

	Notch reflection		
Plate accessibility	Predicted (FE)		Measured with stiffener
	without stiffener	with stiffener	
one-side-access	4.6 %	1.3 %	2.0 %
two-side-access	81 %	73 %	70 %

9.3 Prediction of Defect Localization using FE simulation

The early stage of localizing a defect past the stiffener was discussed based on the accessibility to the stiffener sides. The FE method was used to predict the scattering of the A_0 wave mode from a through thickness notch modelled significantly behind the L-shaped stiffener. Sufficient time separation was maintained between the stiffener and notch reflection. The obtained time trace signals were processed in Matlab to calculate the travel distance based on the known group velocity. Baseline subtraction method was applied to the baseline and defect signals to quantify the arrival time of the first reflection from the notch. The localization method that was explained before in Chapter 6 has been applied to calculate the travel distances, and to draw the locus of the ellipses around the excitation and monitoring sensor locations. Possible complications due to secondary reflections in the difference signal, resulting from wave travelling up and down stiffener, were not taken into account for this preliminary investigation. Various excitation and monitoring configurations were simulated to predict the notch location behind the stiffener using limited access or access to the complete plate structure. The excitation point was modelled at 100 mm ahead of the stiffener and the notch (20 mm length) at 200 mm behind the stiffener (Fig 9.12).

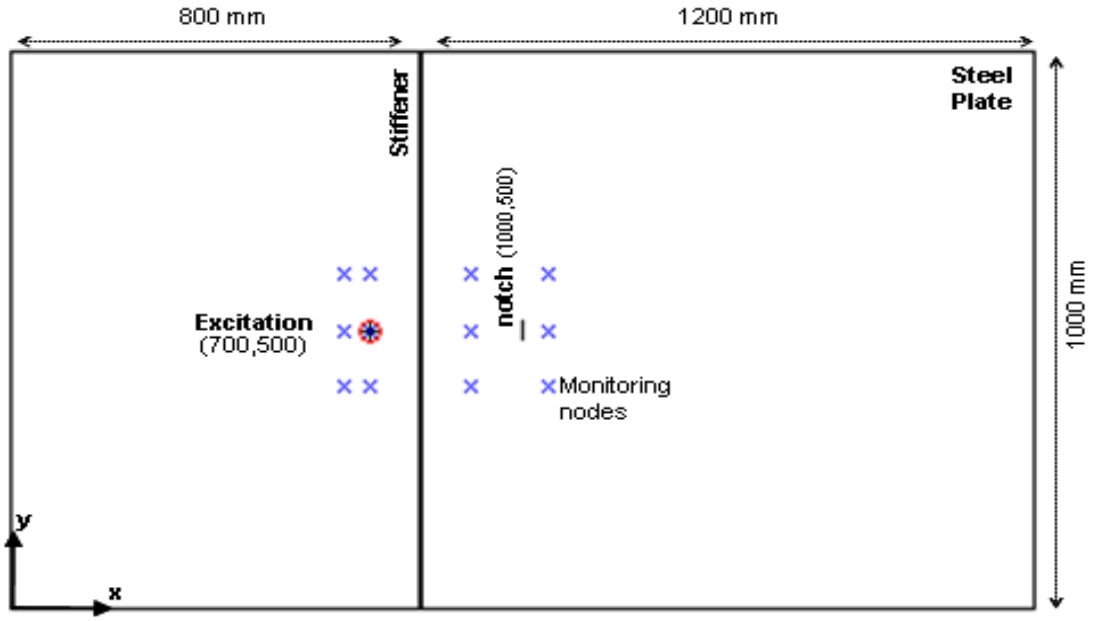

Fig 9.12 Schematic of typical laboratory specimen showing the A_0 mode excitation point surrounded by an array of monitoring nodes to localize simulated notch behind the stiffener.

An array of 12 monitoring nodes was simulated in 4 parallel lines to the stiffener (Fig 9.12). Two lines were modelled in front of the stiffener (100 mm & 150 mm), one line in the middle between the stiffener and the notch, and the last line of monitoring nodes was simulated behind the notch (50 mm). The distance between each two monitoring nodes in the monitoring line was 100 mm. The intersection point of the ellipses at the damage location behind the stiffener was calculated using single sided access to the plate, i.e. using only the 6 monitoring points to the left of the stiffener (Fig 9.12).

The ellipses were intersecting with shallow angles at approximately the location of the notch (Fig 9.13). The zone where the ellipses intersected appears as a rather large area of uncertainty around the notch location. Intersection area up to about 20 – 30 mm from notch center was observed using limited access to single plate side. On the other hand, notch localization using access to both sides of the stiffener was investigated based on monitoring the scattered guided wave field around the notch location (6 monitoring points located to right of stiffener, Fig 9.12).

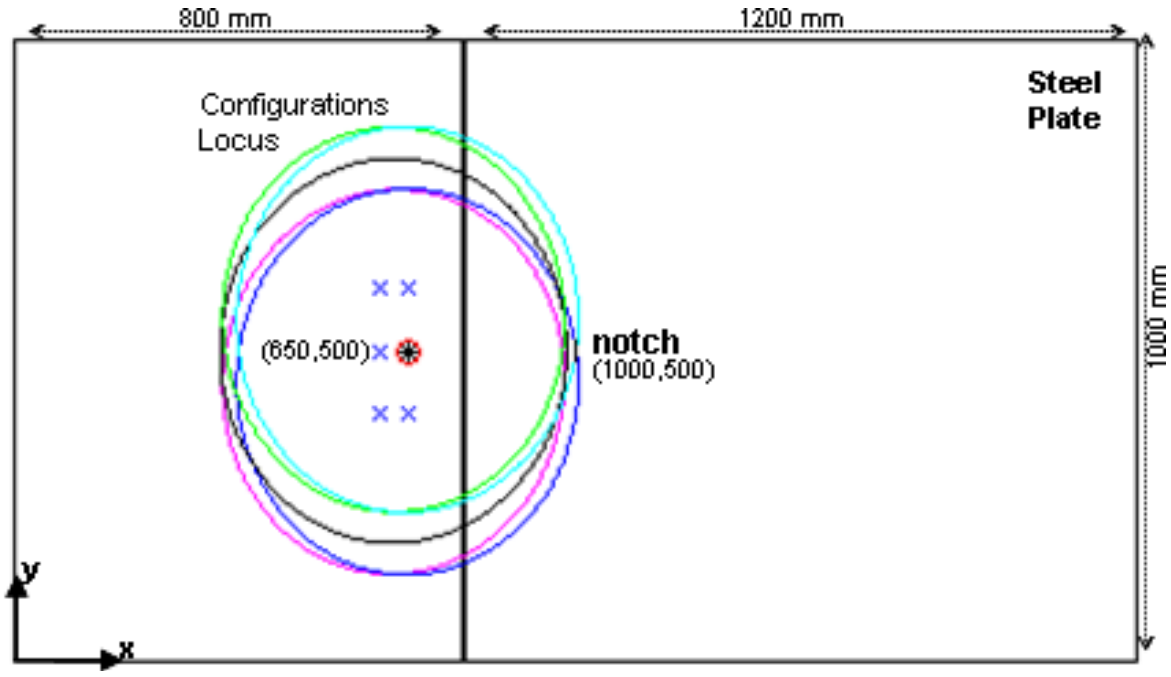

Fig 9.13 Locus of the travel distances for six excitation monitoring pairs showing the intersection of the calculated ellipses at the notch location in the plate using one side access configuration.

The calculated ellipses using Lamb wave excitation on one side of the stiffener and monitoring on the opposite side were intersecting with good accuracy at the simulated notch location with sharp angles (Fig 9.14). Using access to both sides of the plate, the offset in the ellipses intersection point from the center of the simulated notch (Fig 9.14) was about 2 mm. Ellipse intersection at sharp angels was found to allow for very limited level of uncertainty in the defect localization compared to the shallow intersection angles found for single sided access. The method that has been used for the signal processing for damage localization behind the stiffener should be verified by further experimental measurements. The sensors array in the verification measurements should be distributed based on the modelled array to reduce the geometrical error.

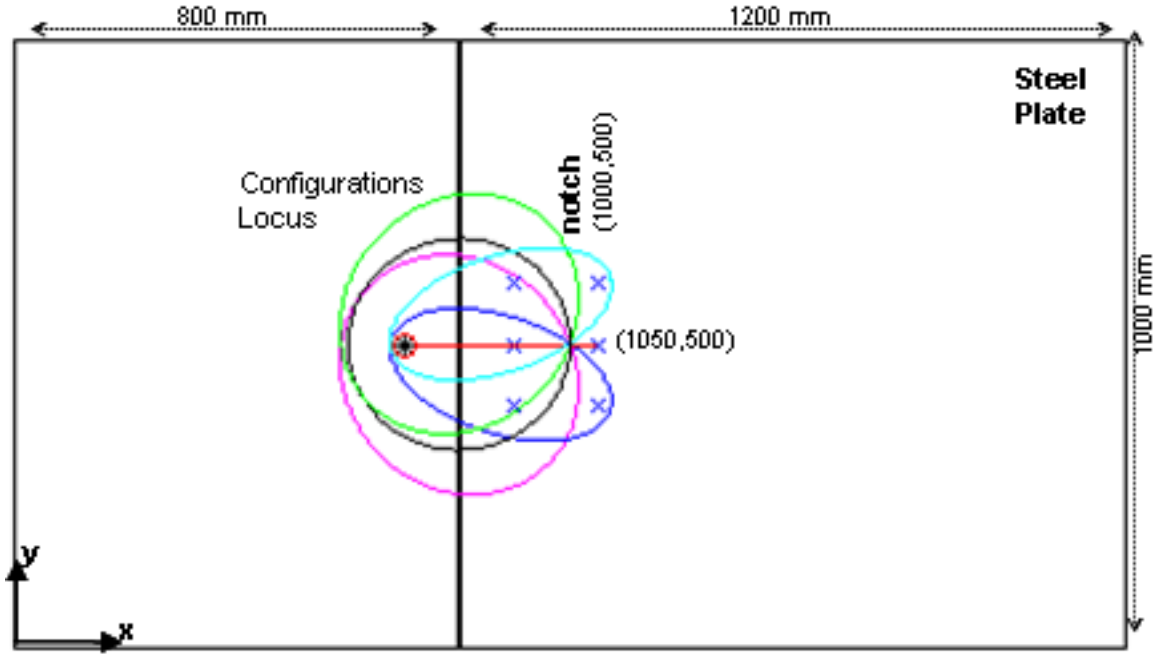

Fig 9.14 Locus of the travel distances for six excitation monitoring pairs showing the intersection of the calculated ellipses at the notch location in the plate using two sided access configuration.

9.4 Summary

Monitoring potential defects in the stress concentration zone behind a welded stiffener using single sided access to the plate was the main motivation for the presented work in this chapter. Accessibility to all parts of the structure to distribute a sufficient number of piezoelectric transducers is not always possible. An alternative choice could be the excitation and monitoring of the GUW scattering from the accessible part of the plate. The reflection from a notch at different distances behind the stiffener was predicted using FE simulations. The notch location that can provide sufficient reflected energy using single-sided-access for the monitoring array and proper time separation between reflected pulses was discussed. The suggested notch location in the numerical simulation was used in the experimental part of the research to verify the outcome of the FE model. The scattered field of the guided wave was predicted and measured at two locations, the excitation side of the plate and behind the notch location. Damage localization was performed employing single stiffener side access and two-sided-access based on the simulated wave propagation. The main obstacle in the damage detection behind the stiffener using single plate side access was the noise level in the measurements of PZT transducers, probably due to measurement problems. Significant reduction was observed in the signal to noise ratio using the subtraction of two reflected pulses from two slots machined in the same location, but of different sizes. Improving the experiment to provide repeatable measurements would enhance the signal to noise ratio.

Chapter 10

Conclusion and Future Work

The literature review of Lamb wave applications for monitoring large plate structures was outlined at the beginning of the PhD thesis. This chapter summarizes the experimental and simulation results that have been obtained from studying A_0 Lamb wave mode propagation and scattering in a large plate structure. The numerical method that has been used to simulate the propagated wave across a stiffener and the experimental measurements that have been performed to validate the predicted behaviour are summarised in this chapter. Future work is proposed at the end of the chapter.

10.1 Applications of Guided Ultrasonic Waves

The propagation of guided waves in a large plate structure has been investigated widely using theoretical, numerical and experimental approaches. The propagation of the fundamental modes of guided waves can be controlled and analysed easily below the cut-off frequency of the higher wave modes. The flexural wave mode A_0 has been chosen out of the potential fundamental wave modes that propagate at low frequency thickness products. The reason for employing the A_0 wave mode in many SHM applications is that it can be excited easily with single side access of the plate using standard ceramic piezoelectric transducers. On the other hand, the out-of-plane motion of the fundamental A_0 wave mode allows it to be measured well using a laser interferometer. Therefore, A_0 Lamb wave mode propagation and scattering at low frequency thickness were used in this research, and were found to show only limited dispersion and pulse distortion around 0.5 MHz.mm.

10.2 Experiments

The A_0 Lamb wave mode excitation and monitoring were performed to understand the way that guided waves are scattered at a stiffener in large plate structures. A PZT transducer was used to excite the A_0 Lamb wave mode and a laser vibrometer to measure the out-of-plane propagation in the low frequency range. Experiments were performed to measure the phase and group velocities. The measurements of the phase and group velocity were analysed in Matlab and compared with the predicted results in Chapter 5. Lamb waves in a large aluminium plate have been used in another experiment to localize an artificial defect using a distributed array of sensors. A comparison was performed in Chapter 6 between the detected damage using experimental measurements and the predicted damage location. Scattering of the A_0 Lamb wave mode at a stiffener welded across the width of a large steel plate has been measured using a laser vibrometer. Lines of measurements at normal and oblique directions across the stiffener were performed to obtain the coefficients of the transmitted and reflected waves. Measurement of wave scattering at each propagation direction employing lines of measurements across the stiffener has been replaced by two parallel lines of measurements on each side of the stiffener. The measured transmitted and reflected waves have been presented in Chapter 7 to validate the FE model. The reflection of the A_0 wave mode from a defect machined behind the welded stiffener was detected and characterized experimentally. The scattered waves at the notch were monitored based on single sided access and access to all parts of the plate. The signal processing strategy that was carried out to separate the notch reflection from the stiffener reflection has been discussed in Chapter 9.

10.3 FE Models

The finite element method was used to simulate the A_0 Lamb wave mode propagation in a large plate structure. A brief description of the finite element method and the commercial software (Abaqus), using explicit time integration, has been introduced in Chapter 4. The element size relative to the wavelength of the propagating wave mode and the travel time between two nodes need to be considered for model stability. Matlab has been used to create automatically an input file that can be modified easily to simulate different plate sizes and provide better control for defect geometry and

stiffener shape. Furthermore, the Matlab code has been used to calculate the number of each node and element in the model, and to provide automatic implementation for changes of the location of the simulated defect and stiffener. Variation of the material properties, excitation parameters, and monitoring locations can be obtained easily using the Matlab code. Several configurations such as phase and group velocity measurements, defect localization, transmission and reflection at a stiffener, and a notch behind the stiffener have been modelled to predict the propagated and scattered guided wave field. Scattering of the fundamental A_0 wave mode at the stiffener and the resulting mode conversion have been simulated. The coefficients of the transmitted and reflected A_0 mode waves from the stiffener modelled across the plate width were predicted. The transmitted and reflected waves from the stiffener have been simulated at different excitation frequencies, and at a range of propagation directions. Normal wave propagation and scattering from a simulated notch past the stiffener were predicted. The possibility of detecting and characterizing a notch behind the stiffener based on access to one or both sides of the stiffener on the plate have been investigated.

10.4 Phase and group velocity

The dependency of the wave velocity on the excitation frequency has been discussed. The dispersive behaviour of the guided waves has been investigated in Chapter 5 to obtain the frequency thickness that provides limited pulse distortion of the propagating wave. The variation of the phase and group velocities has been calculated at low frequency thickness product to study the characteristics of the propagating wave and mode dispersion. The phase and group velocity measurements and FE simulations were processed and analysed in Matlab. The phase velocity has been calculated using the Fourier transform, whereas the Hilbert transform was used for the calculation of the group velocity. The obtained phase and group velocity results have been compared against the theoretical solution using Mindlin theory. Further comparison was made against Disperse code predictions for different material properties. Good match has been achieved between the measured and predicted phase and group velocities.

10.5 Localization Algorithm

Structural damages such as notches and cracks can be detected and localised using A_0 Lamb wave measurements. Artificial damage was created experimentally using a cylindrical mass glued to a large aluminium plate. A distributed array of piezoelectric transducers has been employed to detect and localize the damage. The obtained time trace signals from the distributed array were recorded before and after creating the damage in the plate. The difference between the baseline measurements and damage signal has been used to obtain the residual signal. The travel distance has been calculated for all excitation/monitoring configurations using the envelope of the residual signal and corresponding arrival times. The potential location for the defect has been reconstructed by drawing an ellipse around the locations of the excitation and monitoring sensors. Several ellipses have been used for different transducer configurations to find the intersection point that represents the defect location in the plate. Obtaining three ellipses is the minimum required observation for damage localization, and for higher precision a larger number of ellipses are required. The simulated defect has been detected and localized using distributed sensors, and the detection sensitivity has been validated experimentally. Reasonable match of the defect location has been observed and is presented in Chapter 6.

10.6 A_0 Wave Mode Reflection and Transmission at a Stiffener

The finite element method has been used to model wave scattering at a surface feature in large plate structures. The variation of the plate and stiffener geometry, the excitation and monitoring parameters, has been performed efficiently with the help of the developed Matlab program. Lines of monitoring nodes at normal and oblique angles across the stiffener have been simulated to calculate the transmission and reflection coefficients at several directions. Quantifying the scattered wave from the stiffener at a wide range of angles has been made more efficient by modelling two parallel lines of nodes ahead of and behind the stiffener. Verification has been carried out to ensure that the radial spreading of the predicted transmitted and reflected wave shows the expected $1/\sqrt{r}$ dependency of the guided wave spreading in a plate structure. The mode conversion at the stiffener was investigated at normal propagation and reflection from the stiffener. Multimode scattering was monitored and validated by calculating the

energy balance between the incident and the scattered waves at the stiffener. A comparison between the incident, transmitted and the reflected A_0 Lamb wave modes has been performed and the results have been presented in Chapter 7.

The limitations of the plate geometry, the excitation and monitoring zones were studied before varying the stiffener size and evaluating the wave scattering at the stiffener. Adequate distance has been maintained between the monitoring lines and the plate edges to preserve a time separation between incident and reflected wave pulses. Similarly, sufficient distance has been maintained between the monitoring lines and the stiffener to reduce the effect of the localised interference around the stiffener. Efficient evaluation was performed on the obtained results to correct the amplitude of the propagated wave based on the $1/\sqrt{r}$ dependency and interpolating between the nodes of the parallel lines. Experimental measurements were performed on a steel plate with a welded stiffener in the laboratory to verify the FE results of the wave scattering at the stiffener. The monitoring zone that provides time separation for the reflected wave from the stiffener was selected for monitoring the wave propagation and scattering. For a realistic steel plate, it has been observed that for propagation directions up to 45^o good transmission of the A_0 wave mode across a welded stiffener can be achieved.

10.7 Variation of Stiffener Geometry and Excitation Parameters

The A_0 Lamb wave mode transmission and reflection at different stiffener geometries and excitation frequencies were investigated using FE simulations. Wave scattering was simulated using two groups of monitoring nodes arranged in parallel lines ahead of and behind the stiffener. The processing algorithm, which has been verified in Chapter 7, has been used in Chapter 8 for calculating the coefficients of the transmitted and the reflected A_0 Lamb wave mode at a simulated stiffener of a rectangular cross-section. The simulation outcomes have shown the dependency of the scattered wave on the incident angle and stiffener dimensions. The relation between the direction of the propagating wave across the stiffener and the coefficients of the transmitted and reflected waves has been discussed. Wave transmission and reflection at a wide range of incident angles were calculated for different stiffener dimensions. The findings of the

wave scattering from several stiffener heights and thicknesses were compared. Significant reduction has been obtained in the transmitted waves across a stiffener with increasing stiffener dimensions until constant behaviour was observed for additional increases in the stiffener height or thickness. The maximum of the transmission coefficients was obtained at 45^{o} propagation direction across a stiffener, and for higher angle a different behaviour has been observed. The influence of varying the frequency of the propagating wave across the stiffener has been predicated numerically. The choice of an optimum excitation frequency, which can produce maximum transmission across a stiffener for a specific plate, was recommended.

10.8 Reflection from Notch behind Stiffener

The FE method has been used to investigate the possibility of detecting and characterizing the reflection of the A_0 Lamb wave mode from a through-thickness notch behind the stiffener. The limitations of the detectable defect behind the stiffener have been investigated by varying the notch location. A baseline model has been created to predict the wave propagation before adding a notch to the model. The scattered wave from a simulated notch was characterized using the residual signal after baseline subtraction. Signal processing has been used to time-gate the predicted arrival time of the pulses reflected at the notch and stiffener. The energy of the transmitted wave across the stiffener was adequate to characterize simulated damage behind the stiffener. The evaluation has shown that detecting a defect at an inaccessible area behind a stiffener is achievable if the signal-to-noise ratio was above 30 dB. The suggested excitation and monitoring parameters from Chapter 8 have been used to perform laboratory measurements ahead of and behind a welded stiffener of L-shaped cross-section. The normal reflection of the A_0 wave mode from a slot behind the stiffener was detected and characterized using two different approaches based on the access to sides of the stiffener in the plate. A comparison between the experimental and numerical results has been performed in Chapter 9. The noise level in the experimental measurements affected the detection results significantly. However, the notch pulse has been observed using baseline subtraction, and improving the experiment would enhance the signal-to-noise ratio. In principle, detection of severe damage in an inaccessible area using the normal reflection from damage might be possible.

10.9 Future Work

The reflection of the fundamental A_0 wave mode from damage located behind a stiffener (inaccessible area) has been characterized in Chapter 9. The parameters that affect mode conversion and the transmitted energy across the stiffener should be further investigated.

10.9.1 Mode Conversion and Transmitted Energy

The possibility of calculating wave mode conversion has been investigated along a perpendicular line of monitoring nodes across the stiffener using FE simulations. Further investigations could be performed on the mode conversion and the calculation of the energy carried by each mode in a wider range of propagation directions to validate the calculated coefficients of the transmitted and the reflected flexural waves. The wave propagation and scattering coefficients have been studied at realistic stiffener geometry. The influence of varying stiffener dimensions on the mode conversion and multimode propagation could be investigated.

10.9.2 Localizing a Flaw in an inaccessible area behind the Stiffener

Structural damage such as a crack could be localized using distributed sensors. Since the process that distinguishes between two reflected pulses from a notch and a stiffener was discussed earlier, localizing a flaw located significantly behind the stiffener would be an interesting target for further studies. Baseline and defect measurements in the intact and damaged plate should be performed using a distributed array of monitoring sensors. Analyzing the propagated signal should be based on the processing strategy that has been used in Chapter 9, which however required sufficient reflection from the flaw. The probability of detecting small damage, relative to the wavelength of the propagated wave, could as well be discussed at this stage.

10.9.3 Detection of a defect at the Stiffener Location

Welded stiffeners usually create stress concentrations at the heat affected zone on the plate. Areas of corrosion and fatigue are more likely to appear along the welded stiffener. Having understood the problems that could complicate the reflection from a defect behind the stiffener, this research could go further to study the processing strategy that could quantify the reflected pulse from a defect at or near the weld. Localizing damage behind the stiffener using a distributed array requires solving the wave propagation problem. However, localizing damage at the stiffener or plate boundaries relies more on solving the signal processing problem. Since the arrival time of the slot and stiffener reflection would be the same, it would be impossible to separate the reflected pulse of the defect from the stiffener reflection. Therefore, the alternative choice for detecting a defect at the stiffener weld would be observing the change in the scattering pattern before and after introducing a defect. Based on the obtained information about the change in the transmission and reflection coefficients across the stiffener, similar scattering behaviour would be obtained from an artificial damage at the stiffener weld. The difference between the normal and oblique reflection at a slot could be used for detecting and characterizing the damage.

Several applications could benefit from the better understanding of the scattered and transmitted guided wave fields in a stiffened plate structure found during this research project. The scattered wave field at a defect behind a stiffener could be predicted based on measurements on the accessible side of the plate. The reflection pattern at a stiffener could be examined to find out if there is variation from the predicted scattering field, which might indicate a defect at the weld. Overlap pulses are expected between the stiffener reflection and scattered wave field from a defect at the stiffener location. Therefore, the detection and localization method that has been used in Chapter 6 might need to be modified to take into account additional scattering at the stiffener location. The accuracy of the defect localization method could be examined numerically and validated experimentally. The number of sensors in the distributed array could be optimized based on the required sensitivity of the detection method.

To conclude, this research has provided the understanding of guided wave propagation and transmission across a stiffener based on the numerical prediction and experimental validation. The FE method has been used to investigate the influence of the stiffener geometry and excitation parameters. The obtainable sensitivity in the experimental measurements has been investigated. The simulation has shown that with acceptable signal-to-noise ratio it should be possible to detect and characterize damage located inaccessibly behind a stiffener, or at the stiffener weld. Since it is possible to predict the wave scattering field for an intact, welded stiffener in a plate structure, deviations in the reflection pattern could be used to detect a defect located at the stiffener.

References

[1] P. Fromme and M. B. Sayir, "Detection of cracks at rivet holes using guided waves," *Ultrasonics*, vol. 40, no. 1–8, pp. 199–203, May 2002.

[2] V. Giurgiutiu, *Structural health monitoring with piezoelectric wafer active sensors*. USA: Academic Press, 2008.

[3] H. Lamb, "On waves in an elastic plate," *Proceedings of the Royal Society of London. Series A, Containing Papers of a Mathematical and Physical Character*, vol. 93, no. 648, pp. 114–128, Feb. 1917.

[4] J. L. Rose, *Ultrasonic waves in solid media*. UK, Cambridge University Press, 2004.

[5] R. Mindlin, "Influence of rotatory inertia and shear flexural motions of isotropic elastic plates," *Journal of Applied Mechanics*, vol. 18, pp. 31–38, 1951.

[6] D. E. Chimenti, "Guided Waves in Plates and Their Use in Materials Characterization," *Applied Mechanics Reviews*, vol. 50, no. 5, pp. 247–284, Feb. 1997.

[7] B. Pavlakovic, M. Lowe, D. N. Alleyne, and P. Cawley, "A general purpose program for creating dispersion curve," *Rev. of Prog. in Quantitative Nondestructive Evaluation, ed. by D.O. Thompson and D.E. Chimenti, New York*, vol. 16, pp. 185–192, Jul. 1996.

[8] Y. Lu, L. Ye, Z. Su, and N. Huang, "Quantitative evaluation of crack orientation in aluminium plates based on Lamb waves," *Smart Materials and Structures*, vol. 16, pp. 1907–1914, Feb. 2007.

[9] S. von Ende and R. Lammering, "Investigation on piezoelectrically induced Lamb wave generation and propagation," *Smart Materials and Structures*, vol. 16, pp. 1802–1809, Feb. 2007.

[10] D. Alleyne and P. Cawley, "A two-dimensional Fourier transform method for the measurement of propagating multimode signals," *The Journal of the Acoustical Society of America*, vol. 89, no. 3, pp. 1159–1168, Feb. 1991.

[11] A. Kamal, B. Lin, and V. Giurgiutiu, "Energy and power modeling of multi mode lamb waves propagating in structure bonded with piezoelectric wafer active sensors," *Rev. of Prog. in Quantitative Nondestructive Evaluation, ed. by D.O. Thompson and D.E. Chimenti, New York*, vol. 32, pp. 183–190, Jul. 2012.

[12] P. Fromme, P. D. Wilcox, M. J. S. Lowe, and P. Cawley, "On the development and testing of a guided ultrasonic wave array for structural integrity monitoring," *IEEE Transactions on Ultrasonics, Ferroelectrics and Frequency Control*, vol. 53, no. 4, pp. 777–785, Apr. 2006.

[13] T. Clarke and P. Cawley, "Enhancing the defect localization capability of a guided wave SHM system applied to a complex structure," *Rev. of Prog. in Quantitative Nondestructive Evaluation, ed. by D.O. Thompson and D.E. Chimenti, New York*, vol. 29, pp. 1828–1835, Jul. 2009.

[14] B. Masserey and P. Fromme, "On the reflection of coupled Rayleigh-like waves at surface defects in plates," *The Journal of the Acoustical Society of America*, vol. 123, no. 1, pp. 88–98, Feb. 2008.

[15] P. S. Tua, S. T. Quek, and Q. Wang, "Detection of cracks in plates using piezo-actuated Lamb waves," *Smart Materials and Structures*, vol. 13, pp. 643–660, Feb. 2004.

[16] R. A. Roberts, "Plate Wave Transmission/Reflection at Integral Stiffeners," *Rev. of Prog. in Quantitative Nondestructive Evaluation, ed. by D.O. Thompson and D.E. Chimenti, New York*, vol. 26, pp. 95–102, Jul. 2006.

[17] P. Fromme, P. Wilcox, M. Lowe, and P. Cawley, "On the Scattering and Mode Conversion of the A_0 Lamb Wave Mode at Circular Defects in Plates," *Rev. of Prog. in Quantitative Nondestructive Evaluation, ed. by D.O. Thompson and D.E. Chimenti, New York*, vol. 23, pp. 142–149, Jul. 2003.

[18] P. Fromme and M. B. Sayir, "Measurement of the scattering of a Lamb wave by a through hole in a plate," *The Journal of the Acoustical Society of America*, vol. 111, no. 3, pp. 1165–1170, Feb. 2002.

[19] F. B. Cegla, A. Rohde, and M. Veidt, "Analytical prediction and experimental measurement for mode conversion and scattering of plate waves at non-symmetric circular blind holes in isotropic plates," *Wave Motion*, vol. 45, no. 3, pp. 162–177, Jan. 2008.

[20] C. Vemula and A. N. Norris, "Flexural wave propagation and scattering on thin plates using Mindlin theory," *Wave Motion*, vol. 26, pp. 1–12, Aug. 1997.

[21] F. Shi, J. E. Michaels, and S. J. Lee, "In situ estimation of applied biaxial loads with Lamb waves.," *The Journal of the Acoustical Society of America*, vol. 133, no. 2, pp. 677–687, Feb. 2013.

[22] Y. Lu, L. Ye, Z. Su, and C. Yang, "Quantitative assessment of through-thickness crack size based on Lamb wave scattering in aluminium plates," *NDT & E International*, vol. 41, pp. 59–68, Feb. 2008.

[23] P. Fromme, "Influence of guided ultrasonic wave scattering directionality on the detection sensitivity for SHM of fatigue cracks," *Proceedings of SPIE 7650 – Health Monitoring of Structural and Biological Systems 2010, ed. by T. Kundu,*, no. 76501M, Mar. 2010.

[24] P. Fromme and C. Rouge, "Directivity of guided ultrasonic wave scattering at notches and cracks," *Journal of Physics: Conference Series*, vol. 269, no. 012018, Jan. 2011.

[25] P. Fromme, "Guided wave imaging of part-thickness defects in large structures," *Rev. of Prog. in Quantitative Nondestructive Evaluation, ed. by D.O. Thompson and D.E. Chimenti, New York*, vol. 31, pp. 631–638, Jul. 2011.

[26] P. Rajagopal and M. J. S. Lowe, "Angular influence on the scattering of fundamental shear horizontal guided waves by a through-thickness crack in an isotropic plate.," *The Journal of the Acoustical Society of America*, vol. 124, no. 4, pp. 2021–30, Oct. 2008.

[27] M. J. S. Lowe, P. Cawley, J.-Y. Kao, and O. Diligent, "The low frequency reflection characteristics of the fundamental antisymmetric Lamb wave A_0 from a rectangular notch in a plate," *The Journal of the Acoustical Society of America*, vol. 112, no. 6, pp. 2612–2622, Feb. 2002.

[28] M. J. S. Lowe and O. Diligent, "Low-frequency reflection characteristics of the S_0 Lamb wave from a rectangular notch in a plate," *The Journal of the Acoustical Society of America*, vol. 111, no. 1, pp. 64–74, Feb. 2002.

[29] W. J. Staszewski, B. C. Lee, and R. Traynor, "Fatigue crack detection in metallic structures with Lamb waves and 3D laser vibrometry," *Measurement Science and Technology*, vol. 18, no. 3, pp. 727–739, Mar. 2007.

[30] P. Rajagopal and M. J. S. Lowe, "Short range scattering of the fundamental shear horizontal guided wave mode normally incident at a through-thickness crack in an isotropic plate," *The Journal of the Acoustical Society of America*, vol. 122, no. 3, pp. 1527–1538, Feb. 2007.

[31] A. Demma, P. Cawley, and M. Lowe, "Scattering of the fundamental shear horizontal mode from steps and notches in plates," *The Journal of the Acoustical Society of America*, vol. 113, no. 4, pp. 1880–1891, Feb. 2003.

[32] P. D. Wilcox and A. Velichko, “Efficient frequency-domain finite element modeling of two-dimensional elastodynamic scattering.,” *The Journal of the Acoustical Society of America*, vol. 127, no. 1, pp. 155–165, Jan. 2010.

[33] A. Velichko and P. D. Wilcox, “Efficient finite element modeling of elastodynamic scattering with non-reflecting boundary conditions,” *Rev. of Prog. in Quantitative Nondestructive Evaluation, ed. by D.O. Thompson and D.E. Chimenti, New York*, vol. 32, pp. 142–149, Jul. 2012.

[34] R. A. Roberts, “Guided wave propagation in integrally stiffened plates,” *Rev. of Prog. in Quantitative Nondestructive Evaluation, ed. by D.O. Thompson and D.E. Chimenti, New York*, vol. 27, pp. 170–177, Jul. 2007.

[35] P. D. Wilcox, A. Velichko, B. W. Drinkwater, A. J. Croxford, and M. D. Todd, “Scattering of plane guided waves obliquely incident on a straight feature with uniform cross-section,” *The Journal of the Acoustical Society of America*, vol. 128, no. 5, pp. 2715–2725, Feb. 2010.

[36] P. Fromme, “Experimental and finite element study of guided ultrasonic wave scattering at structural features in a plate,” *Rev. of Prog. in Quantitative Nondestructive Evaluation, ed. by D.O. Thompson and D.E. Chimenti, New York*, vol. 26, pp. 55–62, Jul. 2006.

[37] R. P. Dalton, P. Cawley, and M. Lowe, “The potential of guided waves for monitoring large areas of metallic aircraft fuselage structure,” *Journal of Nondestructive Evaluation*, vol. 20, no. 1, pp. 29–46, 2001.

[38] C. H. Wang, J. T. Rose, and F.-K. Chang, “A synthetic time-reversal imaging method for structural health monitoring,” *Smart Materials and Structures*, vol. 13, pp. 415–423, Feb. 2004.

[39] G. Santoni-Bottai and V. Giurgiutiu, “Exact Shear-Lag Solution for Guided Waves Tuning with Piezoelectric-Wafer Active Sensors,” *AIAA Journal*, vol. 50, no. 11, pp. 2285–2294, Nov. 2012.

[40] V. Giurgiutiu, “Tuned Lamb Wave Excitation and Detection with Piezoelectric Wafer Active Sensors for Structural Health Monitoring,” *Journal of Intelligent Material Systems and Structures*, vol. 16, pp. 291–305, Apr. 2005.

[41] R. Sicard, A. Chahbaz, and J. Goyette, “Guided Lamb waves and L-SAFT processing technique for enhanced detection and imaging of corrosion defects in plates with small depth-to wavelength ratio,” *IEEE Transactions on Ultrasonics, Ferroelectrics and Frequency Control*, vol. 51, no. 10, pp. 1287–1297, Oct. 2004.

[42] P. D. Wilcox, “Omni-directional guided wave transducer arrays for the rapid inspection of large areas of plate structures,” *IEEE Transactions on Ultrasonics, Ferroelectrics and Frequency Control*, vol. 50, no. 6, pp. 699–709, Jun. 2003.

[43] S. D. Holland, R. Roberts, D. E. Chimenti, and J. H. Song, “An ultrasonic array sensor for spacecraft leak direction finding.,” *Ultrasonics*, vol. 45, pp. 121–126, Dec. 2006.

[44] W. H. Leong, W. J. Staszewski, B. C. Lee, and F. Scarpa, “Structural health monitoring using scanning laser vibrometry: III. Lamb waves for fatigue crack detection,” *Smart Materials and Structures*, vol. 14, pp. 1387–1395, Feb. 2005.

[45] Y. Lu, L. Ye, and Z. Su, “Crack identification in aluminium plates using Lamb wave signals of a PZT sensor network,” *Smart Materials and Structures*, vol. 15, pp. 839–849, Jun. 2006.

[46] T. Clarke, F. Simonetti, and P. Cawley, “Guided wave health monitoring of complex structures by sparse array systems: Influence of temperature changes on performance,” *Journal of Sound and Vibration*, vol. 329, no. 12, pp. 2306–2322, Feb. 2010.

[47] J. Rajagopalan, K. Balasubramaniam, and C. V Krishnamurthy, “A single transmitter multi-receiver (STMR) PZT array for guided ultrasonic wave based structural health monitoring of large isotropic plate structures,” *Smart Materials and Structures*, vol. 15, pp. 1190–1196, Oct. 2006.

[48] P. Fromme, “Monitoring of plate structures using guided ultrasonic waves,” *Rev. of Prog. in Quantitative Nondestructive Evaluation, ed. by D.O. Thompson and D.E. Chimenti, New York*, vol. 27, pp. 78–85, Jul. 2007.

[49] J. E. Michaels and T. E. Michaels, “Guided wave signal processing and image fusion for in situ damage localization in plates,” *Wave Motion*, vol. 44, no. 6, pp. 482–492, Jun. 2007.

[50] R. M. Levine and J. E. Michaels, “Model-based imaging of damage with Lamb waves via sparse reconstruction.,” *The Journal of the Acoustical Society of America*, vol. 133, no. 3, pp. 1525–1534, Mar. 2013.

[51] P. D. Wilcox, “A rapid signal processing technique to remove the effect of dispersion from guided wave signals,” *IEEE Transactions on Ultrasonics, Ferroelectrics and Frequency Control*, vol. 50, no. 4, pp. 419–427, Apr. 2003.

[52] J. S. Hall and J. E. Michaels, “A model-based approach to dispersion and parameter estimation for ultrasonic guided waves.,” *The Journal of the Acoustical Society of America*, vol. 127, no. 2, pp. 920–930, Feb. 2010.

[53] F. Lanza di Scalea and S. Salamone, “Temperature effects in ultrasonic Lamb wave structural health monitoring systems,” *The Journal of the Acoustical Society of America*, vol. 124, no. 1, pp. 161–174, Jul. 2008.

[54] G. Konstantinidis, B. W. Drinkwater, and P. D. Wilcox, “The temperature stability of guided wave structural health monitoring systems,” *Smart Materials and Structures*, vol. 15, pp. 967–976, Feb. 2006.

[55] G. Konstantinidis, P. D. Wilcox, and B. W. Drinkwater, “An Investigation into the Temperature Stability of a Guided Wave Structural Health Monitoring System Using Permanently Attached Sensors,” *IEEE Sensors Journal*, vol. 7, no. 5, pp. 905–912, May 2007.

[56] M. D. Todd, E. B. Flynn, P. D. Wilcox, B. W. Drinkwater, A. J. Croxford, and S. Kessler, “Ultrasonic wave-based defect localization using probabilistic modeling,” *Rev. of Prog. in Quantitative Nondestructive Evaluation, ed. by D.O. Thompson and D.E. Chimenti, New York*, vol. 31, pp. 639–646, Jul. 2011.

[57] A. J. Croxford, P. D. Wilcox, B. W. Drinkwater, and G. Konstantinidis, “Strategies for guided-wave structural health monitoring,” *Proceedings of the Royal Society A: Mathematical, Physical and Engineering Sciences*, vol. 463, pp. 2961–2981, Nov. 2007.

[58] S. J. Lee, H. Sohn, J. E. Michaels, and T. E. Michaels, “In situ detection of surface-mounted PZT transducer defects using linear reciprocity,” *Rev. of Prog. in Quantitative Nondestructive Evaluation, ed. by D.O. Thompson and D.E. Chimenti, New York*, vol. 29, pp. 1844–1851, Jul. 2009.

[59] S. D. Holland, J. Song, D. E. Chimenti, and R. Roberts, “Leak Detection in Spacecraft Using a 64-Element Multiplexed Passive Array to Monitor Structure-Borne Noise,” *Rev. of Prog. in Quantitative Nondestructive Evaluation, ed. by D.O. Thompson and D.E. Chimenti, New York*, vol. 25, pp. 885–891, Jul. 2005.

[60] S. D. Holland, D. E. Chimenti, R. Roberts, and M. Strei, “Locating air leaks in manned spacecraft using structure-borne noise.,” *The Journal of the Acoustical Society of America*, vol. 121, no. 6, pp. 3484–3492, Jun. 2007.

[61] B. Masserey and P. Fromme, “Surface defect detection in stiffened plate structures using Rayleigh-like waves,” *NDT & E International*, vol. 42, pp. 564–572, Feb. 2009.

[62] P. Puthillath, J. M. Galan, B. Ren, C. J. Lissenden, and J. L. Rose, “Ultrasonic guided wave propagation across waveguide transitions: Energy transfer and mode conversion.,” *The Journal of the Acoustical Society of America*, vol. 133, no. 5, pp. 2624–2633, May 2013.

[63] P. F. Hansen and S. R. Winterstein, “Fatigue damage in the side shells of ships,” *Marine Structures*, vol. 8, no. 6, pp. 631–655, Jan. 1995.

[64] J. Dobrzański, “Internal damage processes in low alloy chromium–molybdenum steels during high-temperature creep service,” *Journal of Materials Processing Technology*, vol. 157–158, pp. 297–303, Dec. 2004.

[65] Z. Fan and M. J. S. Lowe, “Elastic waves guided by a welded joint in a plate,” *Proceedings of the Royal Society A: Mathematical, Physical and Engineering Sciences*, vol. 465, pp. 2053–2068, Apr. 2009.

[66] Z. Fan, M. Castaings, M. J. S. Lowe, C. Biateau, and P. Fromme, “Feature-guided waves for monitoring adhesive shear modulus in bonded stiffeners,” *NDT and E International*, vol. 54, pp. 96–102, Jan. 2013.

[67] R. S. Reusser, D. E. Chimenti, S. D. Holland, and R. A. Roberts, “Plate wave transmission/reflection at geometric obstruction: experiment,” *Rev. of Prog. in Quantitative Nondestructive Evaluation, ed. by D.O. Thompson and D.E. Chimenti, New York*, vol. 29, pp. 200–206, Jul. 2009.

[68] R. S. Reusser, D. E. Chimenti, S. D. Holland, and R. A. Roberts, “Spacecraft leak location using structure-borne noise,” *Rev. of Prog. in Quantitative Nondestructive Evaluation, ed. by D.O. Thompson and D.E. Chimenti, New York*, vol. 29, pp. 261–268, Jul. 2009.

[69] R. S. Reusser, D. E. Chimenti, R. A. Roberts, and S. D. Holland, “Guided plate wave scattering at vertical stiffeners and its effect on source location.,” *Ultrasonics*, vol. 52, no. 6, pp. 687–693, Aug. 2012.

[70] R. Watson, *Modelling of guided ultrasonic wave scattering at defects*, MSc Thesis. Mechanical Engineering Dept., University College London, 2007.

[71] B. W. Drinkwater and P. D. Wilcox, “Ultrasonic arrays for non-destructive evaluation: A review,” *NDT & E International*, vol. 39, no. 7, pp. 525–541, Oct. 2006.

[72] M. Staudenmann, *Structural waves in nondestructive testing*, PhD Thesis. Swiss Federal Institute of Technology, 1995.

[73] B. Auld, *Acoustic Fields and Waves in Solids*. New York: Wiley-Interscience, 1973.

[74] B. Hosten, L. Moreau, and M. Castaings, “Reflection and transmission coefficients for guided waves reflected by defects in viscoelastic material plates.,” *The Journal of the Acoustical Society of America*, vol. 121, no. 6, pp. 3409–3417, Jun. 2007.

[75] P. Rajagopal, M. Drozdz, E. A. Skelton, M. J. S. Lowe, and R. V. Craster, "On the use of absorbing layers to simulate the propagation of elastic waves in unbounded isotropic media using commercially available Finite Element packages," *NDT & E International*, vol. 51, pp. 30–40, Oct. 2012.

[76] M. Drozdz, L. Moreau, M. Castaings, M. Lowe, and P. Cawley, "Efficient numerical modelling of absorbing regions for boundaries of guided waves problems," *Rev. of Prog. in Quantitative Nondestructive Evaluation, ed. by D.O. Thompson and D.E. Chimenti, New York*, vol. 25, pp. 126–133, Jul. 2005.

[77] F. Yeo and P. Fromme, "Guided ultrasonic wave inspection of corrosion at ship hull structures," *Rev. of Prog. in Quantitative Nondestructive Evaluation, ed. by D.O. Thompson and D.E. Chimenti, New York*, vol. 25, pp. 202–209, Jul. 2006.

[78] B. Beardsley, M. Peterson and J. Achenbach, "A simple scheme for self-focusing of an array," *Journal of Nondestructive Evaluation*, vol. 4, pp. 169–179, Jun. 1995.

[79] H. Li, H. Yang and J. Hu, "Modal Strain Energy Decomposition Method for Damage Localization in 3D Frame Structures," *Journal of Engineering Mechanics*, vol. 132, pp. 941–951, Sep. 2006.